2018

Modeling Fluid Motion over Fibrous Surfaces

Delli Ganesh Venkateshan

Modeling Fluid Motion over Fibrous Surfaces

A dissertation submitted in partial fulfillment of the requirements for the degree of Doctor of Philosophy at Virginia Commonwealth University.

by

Delli Ganesh Venkateshan

M.Tech. Aerospace Enginering, Indian Institute of Technology, Guwahati, India, 2014

Director: Hooman V. Tafreshi

Professor, Department of Mechanical and Nuclear Engineeing

Virginia Commonwealth University

Richmond, Virginia

March, 2018

Dedication

I would like to dedicate this work to my brother (Shanmuga Sundaram Venkateshan) and my mother (Gomathi Venkateshan) whose continuous support made it possible for me to comeout of all the downfalls and finish my thesis successfully. My brother had faith in me more than anyone and he drove me all the way from my high school till my Doctoral studies. His indirect and invaluable contribution made me who I am today.

Acknowledgment

I wish to express my sincere thanks to my advisor and my mentor Prof. Hooman V. Tafreshi for his contiuous support of my scientific endeavors; valuable guidance, and encouragement. I have been lucky to have a supervisor who has lots of patience while going through my manusripts and correcting me whenever I am deviating from finishing the tasks.

I would also like to extend my feeling of gratitude to my committee members—Prof. Jayasimha Atulasimha, Prof. Christina Tang, Prof. Hong Zhao and Prof. Hu Yang for their insightful questions and comments which have helped strengthen my work.

I want to expresss my sincere gratitude to my friends (Kranthi Kumar Chougani, Suresh Kumar Marinaiker, Vinay Kumar Idikuda, Naren Motte, Naren G.K) and to my labmates (Mana Ameri, Ahmend Saleh, Ali, Sina, Hossain, Jamali, Noor) who made my days in Richmond and VCU unforgettable.

Finally, I would like to thank, Dr. Karla Mossi and Dr. Gary Tepper for providing me with valuable advice throughout my studies at VCU and for providing me with recommendation letters for the dissertation scholarship award.

I would also like to thank Nonwovens Institute at NC State University and VCU School of Engineering for financial support.

Table of Contents

List of Figures

Fig. 2.7	Effects of coarse fiber number fraction n_c on SVF (a) and thickness (b) of bimodal mats consisting of fibers with a fine fiber diameter of $d_f = 1$ μm but coarse-to-fine fiber diameter ratios of $R_{cf} = 2$ and 3. Figure (c) and (d) show the same results but for mats with $d_f = 2$ μm. Each simulation was repeated three times.
Fig. 2.8	A sample nanofiber mat with a basis weight of 5 $\mathrm{g/m^2}$ made of orthogonal soft fibers with a diameter of 1 μm is shown in (a) from two different views. Effects of varying fiber diameter of the fibers SVF and thickness are shown in (b) and (c), respectively, for mats made of orthogonal soft and rigid fibers. The results shown in (d)–(f) are similar to those of (a)–(c) except fibers in these figure have random in-plane orientations (i.e., a 45 degree standard deviation about a zero mean). Each simulation is repeated three times.
Fig. 2.9	Deposition of soft fibers with a diameter of $d = 5$ μm with an arbitrary initial velocity of $v_i = 0.05$ m/s on a monofilament woven substrate from an isometric view (a). The magnified image in (b) shows how the soft fibers conform to the geometry of the substrate.
Fig. 3.1	An example SEM image of the superhydrophobic wire screens considered in the study.
Fig. 3.2	Virtual unit-cell of a wire screen used in SE calculations (a). The area (b) and volume (c) elements used in deriving the energy equation for the system.
Fig. 3.3	Sample simulation results showing the AWI under different hydrostatic pressures in (a) and (b). Failure due to AWI sagging is shown in (c). Failure due to AWI breakup at the breakthrough pressure is shown in (d). Here

	$d_w = 254$ μm and $s_w = 458$ μm.
Fig. 3.4	An SEM image of the superhydrophobic spray-on coating used on a microscope slide. The inset shows droplet contact angle measured via a goniometer.
Fig. 3.5	Our experimental setup designed to measure the breakthrough pressure of SHP woven screens (a). Optical images of AWI trying to enter a SHP screen at low (b) and high (c) magnifications.
Fig. 3.6	The computational domain considered for solving the Navier–Stokes equations using an accurate estimate of the 3-D shape of the AWI over the screens (a). Schematic diagram describing the slip length concept (b).
Fig. 3.7	Dimensionless effective slip length values calculated for screens with different area fractions. An oversimplified representation of the screens geometry in considered here to compare the results of our numerical calculations with those of [8] for validation purposes.
Fig. 3.8	Effects of wire-to-wire spacing s_w on failure pressure (breakthrough and sagging pressures) and wetted area fraction of the screens having constant wire diameters of $d_w = 254$ μm (a) and $d_w = 508$ μm (b). Experimental breakthrough pressure values (red symbols) are added to the figures for comparison.
Fig. 3.9	Effects of hydrostatic pressure wetted area fraction (a and c) and slip length (b and d) for screens with different geometries. Slip length predictions of Eq. 5 ($\overline{b}_{up}$) and Eq. 6 ($\overline{b}_{app}$) are compared with one another.
Fig. 3.10	Average velocity at a distance δ above the solid surface in a plane slicing through the screen is shown for two different hydrostatic pressures of 0 and 500 Pa in (a) along

	with example velocity profiles. Effects of the gap distance between the upper and lower plate in Couette geometry H on slip length is shown in (b) for two different gap values as a function of pressure.
Fig. 4.1	(a) Illustration of a flat AWI over an array of parallel cylinders with a diameter d_w and separated by a distance s_w. The parameters f and r_f from Eq. 1 are also shown graphically; (b) lower and upper contact angles are shown for a droplet deposited on a tilted screen.
Fig. 4.2	Sliced view of a droplet on a wire screen showing the solid–liquid wetted area and the interface immersion angle. Parameters used in Eq. 8 are shown using a 2-D representation of the air–water interface in contact with a wire.
Fig. 4.3	(a) A microscope image of a glass slide coated with Ultra-Ever Dry, (b) a droplet image on the coated glass slide showing an YLCA of $\theta_{YL} = 120^{\circ}$; (c) an SEM image of one of the spray-coated wire screens used in this work.
Fig. 4.4	Side (a and b) and top (c and d) views of a droplet with a volume of $V = 30$ µL on a screen with $d_w = 254$ µm, $s_w = 660$ µm, and $\theta_{YL} = 120^{\circ}$ obtained from experiment (left) and simulation (right). (e) Local contact angle $\theta_A = \pi - \theta_l$ is shown using the normal to the droplet surface at contact line $\hat{n}_p$ and the normal to a horizontal plane placed at the top surface of the wires $\hat{n}_d$.(f) Apparent contact angle along the azimuthal angle β is shown for a droplet with a volume of $V = 5$ µL on screens with a wire diameter of $d_w = 166$ µm and an YLCA of $\theta_{YL} = 120^{\circ}$but different spacing values.
Fig. 4.5	(a) A stable position for a droplet on a wire screen. Examples of the regions where the droplet contact line cannot reside are shown with yellow arrows. **(b)** Global

	droplet energy and apparent contact angle obtained from simulations with different initial positions on screens with a diameter of $d_w = 166$ μm and spacing of $s_w = 113$ μm with droplet volumes of $V = 5$ μL. (c) The apparent contact angle using Eq. 10 from the simulations for the same parameter as in (b). (d) Effect of droplet volume on the apparent contact angle for the screen in (b) for both volume-increase (blue) simulations and volume-decrease (red) simulations.
Fig. 4.6	(a) Effects of wire spacing s_w on apparent contact angle θ_{app}, distance between droplet center and screen top surface h , and wetted area A_w for droplets with a volume of 5 μL are shown in (a) and (b). Simulation data, and predictions of Eq. 2 are shown in black and in red, respectively. Droplet contact area with screens having different wire diameters and spacing are shown in (c).) Effects of wire spacing s_w on apparent contact angle θ_{app} is shown in (d) for a droplet with a volume of $V = 30$ μL.
Fig. 4.7	Effects of tilt angle α on lower and upper contact angles for a droplet with a volume of $V = 5$ μL on a screen with $d_w = 254$ μm, $s_w = 381$ μm but two different YLCAs of 120 and 140 degrees are shown in (a) and (b), respectively. Comparison between droplet contact angles from experiment (left) and simulation (right) for three different tilt angles of 0, 40, and 80 degrees are given in (c). Droplet contact with wire a screen is given for three different tilt angles of 0, 10, and 20 degrees. Droplet volume and screen dimensions are the same as those in (a) with an YLCA of 120 degrees.
Fig. 4.8	(a) Effects of wire spacing on sliding angle for a droplet with $V = 5$ μL on screens with wire diameter and YLCAs. (b) The force calculated using Eq. 3 (black color)

	and Eq. 4 (blue color) for the same parameters in (a) at sliding angle α from SE simulations.
Fig. 4.9	Footprint of a droplet with a volume of 5 µL on two screen with identical properties but different wire spacing values of 136 µm and 559 µm are given in (a) and (b), respectively, at different tilt angles. The contact area between the droplet and the screens at tilt angles of 0 and 15 degrees are given in (c). Variations of the local contact angle along the perimeter of the same droplet on a screen with dimension $d_w = 254$ µm, $s_w = 381$ µm, and $\theta_{YL} = 140^{\circ}$ is shown in (d).
Fig. 4.10	Effects of droplet volume on the sliding angle for screens with different diameters, different wire spacing, and different YLCAs are given in (a) and (b). Experimental and computational data are shown with green and black symbols, respectively.
Fig. 5.1	(a): Side-view and cross-sectional view of a trilobal fiber. (b): Overlap of cross-sectional view of the fibers with different lobe height.
Fig. 5.2	(a) Local contact angle θ_l is shown using the tangent drawn to the droplet at the three phase contact line and xy plane for both lateral view(left) and longitudinal view(right) of the droplet. (b) Local contact angle is shown along the length of the contact line for different lobe heights for fiber radius $r_f = 200$ µm and droplet volume $V/{r_f}^3 = 200$ with $\theta_{YL} = 60°$.
Fig. 5.3	(a) The apparent contact angle θ_A measured using Eq. is shown for fibers with different lobe heights ranging from $a = 0$ to $a = 0.4$ and radius $r_f = 200$ µm having YLCA $\theta_{YL} = 60°$ for two different volume ratio $V/{r_f}^3 = 200$ and

	$V/{r_f}^3 = 400$. (b) The total length of three phase contact line and wetted area were shown for the same parameters as in (a).
Fig. 5.4	The effects of the azimuthal orientation (a) on the maximum force per unit mass (b) required to detach droplets from a fiber with $r_f = 200$ μm but different lobe heights ranging from $a = 0$ to $a = 0.4$ and YLCA of $\theta_{YL} = 60°$. (c) The shape of a clamshell shape droplet with $V/{r_f}^3 = 200$ on a trilobal fiber for different lobe heights.
Fig. 5.5	(a) Free body diagram showing the forces acting on the droplet. (b) Effect of lobe height on the capillary force, pressure force and maximum detachment force on fiber radius $r_f = 200$ μm.
Fig. 5.6	The maximum force per unit mass required to detach droplets with different volumes for fiber with $r_f = 200$ μm for different cross-section of fibers (circularand trilobal) for an YLCA $\theta_{YL} = 60°$;(b) Droplet with $V/{r_f}^3 = 300$ for fibers with circular and trilobal cross section.

Abstract

Modeling Fluid Motion over Fibrous Surfaces

By: Delli Ganesh Venkateshan, Ph.D.

A dissertation submitted in partial fulfillment of the requirements for the degree of Doctor of Philosophy at Virginia Commonwealth University.

Virginia Commonwealth University, 2018

Director: Hooman V. Tafreshi, Professor
Professor, Mechanical and Nuclear Engineeing Department

The ultimate goal of this project has been to develop a computational model for quantifying the interactions between of a body of fluid and a fibrous surface. To achieve this goal, one has to develop a model to create virtual structures that resemble the morphology of a fibrous surface (Objective-1) as well as a model that can simulate the flow of a fluid over these virtual surfaces (Objective-2). To achieve the first objective, we treated fibers as an array of beads interconnected through viscoelastic elements (springs and dampers). The uniqueness of our algorithm lies in its ability to simulate the curvature of the fibers in terms of their rigidity, fiber diameter, and fiber orientation. Moving on to Objective-2, we considered woven screens for their geometric periodicity, as a starting point. We studied how fiber diameter, fiber spacing, and contact angle can affect the skin-friction drag of a submerged hydrophobic woven screen, and how such surfaces resist against water intrusion under elevated hydro-static pressures (a requirement for providing drag reduction benefits). We also studied the impact of surface geometry and wetting properties on droplet mobility over these surfaces. Laboratory experiment was conducted at various stages throughout this investigation, and good agreement was observed between the experimental data and the results from our numerical simulation.

Chapter 1. Introduction

1.1 Background Information

Superhydrophobic (SHP) surfaces, often produced by incorporating single or multiscale roughness into a hydrophobic material, are known for their ability to reduce the area of contact between water and the solid surface (referred to here as the wetted area). The reduced wetted area, in turn, brings about peculiar attributes that are essential for applications such as self-cleaning [1] and drag-reduction [2] to name a few. Given the prohibitive cost associated with large-scale production of microfabricated SHP surfaces, woven screens enhanced with functional surface treatments/coatings have recently been considered as a cost-effective alternative in many applications requiring a SHP surface. SHP coatings can be used for drag reduction [3], oil–water separation [4], self-cleaning and anti-icing [5], underwater protection of electronic devices [6], water harvesting [7], and heat transfer [8] among many other applications. There have also been interesting studies on the load-carrying properties of SHP wire screens for device manufacturing. In the following subsections the background information about capillarity force, fluid interactions with fibrous surfaces, droplet interactions with fibers were presented.

1.1.1 Capillarity Force

Capillarity is the physical mechanism caused due to the interfacial forces which establishes the shape of the interface between two immiscible fluids or upon interaction with the solid. The surface tension can be defined as a property of the fluid which causes the fluid surface to acquire the minimum surface area possible. Young and Laplace in 1800s was the first to introduce the surface

tension and formulated the wettability of a substrate in terms of contact angle between the liquid-gas and solid-liquid interface as [9, 10].

$$\sigma \quad co \quad = \sigma_{SG} - \sigma_{SL} \tag{1.1}$$

where σ , σ_{SG} and σ_{SL} represents the interfacial tensions of liquid-gas, solid-gas, and solid-liquid, respectively. When the pressure diference across the interface araises, the surface tension forces balance the pressure forces and the resulting equation known as Young-Laplace equation can be written as

$$\Delta P_{cap} = \sigma(\frac{1}{R_1^*} + \frac{1}{R_2^*}) \tag{1.2}$$

where σ is the interfacial tension and R_1^* and R_2^* are function of principal radii of the surface. As there are many practical applications where the interactions of liquid alongside solid can be seen, many researchers studied the interface shape and stability over different surfaces [11-13, 5, 14-16].

1.1.2 Fluid Interactions with fibrous surfaces

Fluid interaction (either droplet or AWI) with fibrous surfaces can be seen in many applications in recent days. The wettability of the fibrous surface depends on the chemical composition, which in turn defines the contact angle and the geometric attributes of the surface, which in turn defines the penetraton of the fluid into the surface [17]. The capillary forces between the liquid and the solid causes the liquid to spread across the surface and the surface tension forces within the liquid cause the liquid to attain the minimum surface area possible. A force balance between the capillary forces and the surface tension forces determines the degree of wettability of the surface [18-19]. The

Young's Laplace Contact Angle (YLCA) is defined as the angle at which the liquid-vapor interface meets the solid-liquid interface. The YLCA provides the measure of the wettability. Depending on the contact angle made on the surface, surfaces were categorized into hydrophilic (contact angle < 90°), hydrophobic (90°< contact angle < 150°) and superhydrophobic (contact angle > 150°) surfaces (SHP).

Superhydrophobic surfaces is well known for their less wettability showing less to almost no-contact between the liquid drop and the surface. Many natural surfaces exhibit SHP properties, lotus leaf and water striders were few among them [14]. As mentioned earlier, hydrophobic characterstics mainly depend on the surface topology. Superhydrophobic (SHP) surfaces, often produced by incorporating single or multiscale roughness into a hydrophobic material, are known for their ability to reduce the area of contact between water and the solid surface (referred to here as the wetted area). An alternative approach to mimic the nature and produce SHP surfaces is to coat the substrate with a hydrophobic material, e.g., deposition of polystyrene nanofiber electrospun mats. The coated fibrous surfaces creates the micro or nano scale roughness and induces the hydrophobicity of the surface or substrate [20-21].

Performance of a SHP surface depends on the mechanical stability of the air–water interface (AWI) that forms over the non-wetting pores of the surface upon contact with water. Depending on surface geometry and hydrostatic/hydrodynamic pressure, the AWI can ingress into the space between the fibers/screen's wire. Superhydrophobicity on a fibrous surface is due to Cassie state i.e, the liquid doesn't penetrate into the fibrous surface and remain fully dry forming a composite interface. The fibrous surface looses it's hydrophobicity when the liquid comes into contact with the entire solid surface, Wenzel State. Depending on surface geometry and hydrostatic/hydrodynamic pressure, the AWI can ingress into the space between the wires to allow the Wenzel state, the Cassie state,

or a series of transition states in between the two extreme states to prevail over the surface [22-23]. The hydrostatic pressure at which a SHP surface starts departing from the Cassie state is referred to as the critical hydrostatic pressure (CHP) or transition pressure [5]. This definition is often used in the context of pores with sharp-edged entrance where the AWI can anchor (pin) itself to the edges of the pore. The definition is less clear when the pore entrance is round (the case with wire screens). This is because in this case, the AWI cannot anchor itself to any sharp corner, and has to conform to a shape that maintains the Young–Laplace contact angle (YLCA) at any point along the curved walls of the pore. Therefore, even at a zero hydrostatic pressure, it is hard to define a fully dry (Cassie) state. Obviously, the AWI moves further down into the pore in response to any increase in the hydrostatic pressure [5,24-25]. The AWI may slip between the pores and may reach the bottom of the pore or surface, if the hydrostatatic pressure is high enough. Furthermore, the entrapped air in Cassie state dissolves into water and the rate of dissolution increases with increase in hydrostatic pressure. For the lack of a better alternative, we define CHP for a pore with round entrance, to be the hydrostatic pressure at which the AWI moves down into the pore such that the pore's capillary pressure reaches its maximum value (referred to here as the breakthrough pressure). Transition to the Wenzel state can also occur if the AWI touches the bottom of the pore under pressure. This has been identified in the literature as failure due to AWI sagging or the lack of "robustness height" [25]. Therefore, there is a need to shed some light on the affect of surface topology and chemical composition of the surface on the wettability and the fluid penetration along the surface.

The 3D shape of the WI on a surface can be obtained eithr through force balance or though the energy minimization technique. Solving the force balance equation along the three-phase contact line for a random 3D fibrous surface is very much complicated. For all the numerical simulations we used public domain software called the Surface Evolver (SE). The Surface Evolver (SE), finite element code, is used to determine the shape and position of the AWI under elevated hydrostatic pressures. The general form of the energy equation E being integrated in the code can be expressed as [4]:

$$E = p\iiint dV - \sum \sigma \cos\theta_i \iint dA_i \tag{1.3}$$

where p is the applied pressure difference across the interface which is being integrated over volume element dV. The summation refers to the surface energy contributed by the wetted area of each particle/fiber associated with the interface dA_i. To ensure proper calculation of the screens\fibers' energy contribution, the integrand dA_i must be derived for each AWI face and applied explicitly in the code. This approach will give us the shape of the interface and consequently the ability to calculate the wetted area A_w which is the solid-liquid area per unit area of a flat surface.

The AWI formed over the pores of a SHP fibrous surface can provide drag reduction benefits for a submerged surface. A body of water flowing over a SHP fibrous surface experiences frictional (no-slip) contact with the solid surface and slippery (no shear) contact along the AWI. Overall, one can expect a reduction in the skin-friction drag of a solid surface due to a reduction in the surface wetted area upon using a SHP fibrous surface. The decrease in the skin friction drag is often portrayed by the effective slip length, which is the average distance underneath the water–solid interface at which the velocity extrapolates to zero. The slip length on a SHP surface is related

to solid-liquid wetted area A_w, and is therefore pressure dependent. While there are several studies proposing an explicit relationship between slip length and A_w for internal flows over SHP surface comprised of streamwise or transverse sharp-edged grooves, the literature is scarce when it comes to slip length correlations for SHP surfaces made of fibrous coatings . The most practical way of defining an effective slip length is what one may observe in a rheometer experiment with the SHP surface as the bottom plate. [26],

$$\bar{b}_{up} = \left(\frac{\tau_{flat}}{\tau_{slip}} - 1\right) H \tag{1.4}$$

where τ_{flat} is the conventional Couette flow shear stress at the upper plate (in the absence of a SHP bottom plate), and τ_{slip} is the shear stress at the upper plate with the SHP wire screen as the lower plate. An approximate analytical effective slip length expression is also provided in [3] for flow over SHP surfaces, as

$$\bar{b}_{app} \approx \frac{l_w}{3\pi} \ln\left(\frac{2\left(1+\sqrt{1-A_w}\right)}{\pi A_w}\right) \tag{1.5}$$

According to this equation, effective slip length is positive for $A_w < 0.868$, and negative when $0.868 < A_w \leq 1$. The effective slip length expression of [26] treats the fibrous surface as a 2-D planar surface (i.e., no curvatures is considered for the AWI or the wires). There is no accurate approach for obtaining an estimate of a fbrous surface wetted area in 3-D and to calculate its drag reduction benefit (slip length). Therefore, there is a need to develop a model to simulate the flow over SHP fibrous surface and estimate the drag reduction benefits.

1.1.3 Droplet Interactions with Fibrous surfaces

Understanding the underlying physics of droplet movement inside fibrous media is a challenging problem of crucial importance to many engineering applications such as liquid− liquid separation, liquid−gas filtration, textiles, microfluidics, water transport in fuel cells, and even water harvesting, to name a few [27-33]. Early studies have discussed equilibrium position of droplet and droplet mobility on flat surfaces [34]. The wetting behavior and droplet mobility on fibrous surfaces differs from the wetting on the flat surfaces. A number of previous studies have dealt with the apparent contact angles, droplet geometry, sliding mechanisms of droplet on non-flat surfaces [35-36]. The complexity in predicting the degree of droplet mobility over a fibrous surface or curved surface arises mainly from the fact that it depends on many factors like the wetted area (WA) of the solid surface, the length of the three-phase air–water–solid contact line (CL), the 3-D shape and orientation of WA and many others. Obviously, these factors depend strongly on both the surface morphology and on the physical properties of the droplet. These factors make it almost impossible to accurately predict the degree of droplet mobility over a hydrophobic surface via a first-principles theoretical approach. In the absence of a better option, droplet mobility over a hydrophobic surface has often been characterized empirically in terms of the droplet's advancing and receding contact angles (CAs) which are the CAs in the direction of droplet motion (most probably the largest and smallest CAs along the perimeter of the droplet) on that specific surface.In the absence of a better option, droplet mobility over a fibrous surface has often been characterized empirically in terms of the droplet's advancing and receding contact angles (CAs) which are the CAs in the direction of droplet motion (most probably the largest and smallest CAs along the perimeter of the droplet) on that specific surface. One should keep in mind that there is nothing fundamentally important about the advancing and receding CAs other than they are easy to

measure via imaging. In fact, the advancing and receding CAs are only two "dependent variables" that owe their values to a series of morphological (surface) and thermodynamic (droplet) "independent variables", and therefore their applicability is limited to the specific surface and droplet size used in measuring them. Because of these inherent limitations, the force required to detach a droplet from a surface is often presented in terms of the difference between the advancing and receding CAs (i.e., CA hysteresis) but multiplied by an empirical factor to compensate for the lack of sufficient information about the impact of the actual "independent variables" in this problem [37–38]. An additional factor further complicating this problem is the tendency of the droplet to pin itself to certain local sites on the surface (caused perhaps by chemical or morphological non-homogeneities). In the absence of pinning effects, a numerical approach has been proposed to predict the force of detachment explaining the mechanism of contact angle hysteresis.

Although circular fiber is the most common shape manufactured by synthetic fiber producers, other shapes such as elliptical, lobed, and wedge-shaped cross-sections, are beginning to emerge for a variety of reasons—performance, bulkiness, tactility, processing, etc. [39]. Fibrous surfaces made from these various fibers may be configured as pads, pleated papers, bonded webs, nettings, or composites. [40]. The wetting behavior and droplet detachment on non-circular fibers differs from the wetting on the circular fibers. The only research on droplet-fiber interaction on non-circular fibers considers wedge-shaped cross-sections [41-42] but does not explain the effect of the shape of the fiber –e.g., number and size of the wedges- or volume of the droplets on fibers' wettability explicitly. Henceworth, there is a need to investigate the importance of a fiber's cross-sectional shape on ACA and droplet detachment force from the fibers.

1.2 Overall Objectives of This Thesis

This main motivation for this study is to develop a theoretical model to study the fluid motion over fibrous coatings. The main contribution of this work is to understand the percentage of drag reduction that can be obtained through manmade fibrous coatings and to underlying physics of droplet movement over non-flat surfaces and filter media for fluid-fluid separations. Other applications include self-cleaning, and anti-icing as well as droplet filtration, fog harvesting, and incontinence products. Our study is divided into two distinct objectives: 1) modelling the morphology of the 3-D structure of nanofiber mats, 2) modelling the flow of a fluid over these virtual surfaces.

For the case of fibrous coatings, there is no accurate model in the literature which simulates the full morphology of the electrospun nanofibers. The current study is devised to develop a modeling approach toward solving this problem by simulating the 3-D structure of nanofiber mats. Furthermore, we model the air-water interface over the superhydrophobic woven screens for different geometric and wetting propoerties. Altering the operating hydrostatic pressure across the air-water interface can cause a change in performance (drag reduction) of such coatings by affecting the stability of the air-water interface and also changing the solid-water area. For the case of droplet interactions over non-circular fibers (trilobal, rectangular) and non-flat surfaces (woven screen), we develop a model to predict the apparent contact angle as a function of geometric parameters. This information is crucially important for understanding the dynamics, coalescence, and migration of liquid droplets in fibrous structures for an applied force. The ultimate goal of the proposed research is to develop a fundamental theory for design and optimization of coalescing filter media used in fluid-air or fluid-fluid separation, fog-harvesting.

Despite the widespread applications of electrospun fibers, there is still no accurate method to measure the thickness or porosity of compliant electrospun mats. Chapter 2 discusses a modeling approach to help better understand this problem. This work presents a methodology for simulating the morphology of nanofiber mats by treating each fiber as an array of beads (see Chapter 2). The uniqueness of our algorithm lies in its ability to emulate how fibers conform to the geometry of the surface on which they deposit, e.g., previously deposited fibers. This feature is important for predicting how the thickness of a nanofiber mat grows as fibers continue to deposit on the collector. Our algorithm is implemented in a C++ program and is used to study the effects of fiber rigidity, fiber diameters, and fiber orientation on the thickness and porosity of electrospun mats. Contrary to the common belief, it was shown that reducing fiber diameter, for a fixed basis weight, does not necessarily lead to an increase in the thickness or porosity of the mat. The thickness and porosity were shown to depend on fibers tendency to bend at the fiber-fiber crossovers, which varies depending on properties of the fibers and electrospinning conditions.

Chapter 3 presents a detailed study on the failure pressure of spray-coated superhydrophobic wire screens in terms of their geometric and wetting properties. Such information is needed in designing fluid–fluid or fluid–air separation/barrier media as well as drag reducing and self-cleaning surfaces, amongst many others. Good agreement has been observed between the results of our numerical simulations and the experimental data for failure pressure. In addition, the wetted area of the screens was calculated and used to predict their drag reduction benefits when used in a Couette flow configuration under different operating pressures. Interestingly, it was found that operating pressure in the Couette configuration does not significantly affect the drag reducing effects of the screens.

Chapter 4 presents a detailed investigation of the droplet lower and upper contact angles on hydrophobic wire screens with different properties such as wire diameter, wire spacing, or Young–Laplace contact angle. Numerical simulation and experiment were considered to better our understanding of the factors impacting droplet sliding on a hydrophobic screen, and to quantify their importance. To conduct the numerical simulations, the screens' geometry was programed in the Surface Evolver code, and the droplet shape was obtained by minimizing the total energy of the droplet–screen system iteratively using the code's finite element solver. Good general agreement was observed between the results of our numerical simulations and experimental data. Most interestingly, it was observed that droplet sliding angle increases with increasing the wire spacing in screens with a given wire diameter. To explain this counterintuitive observation, detailed quantitative information is presented in terms of the three-phase contact line on the droplet's receding side as well as the penetration of the air–water interface into the void space between the wires. The results of our study are discussed in the context of the contemporary literature.

The equilibrium shape of droplet on fibers with trilobal cross-section is studied in chapter 5 via numerical simulation. Special attention has been paid to droplet shape on trilobal fibers having different lobe height. In addition, the effects of droplet volume and azimuthal orientation of fibers with respect to direction of gravity are investigated. Our results indicate that trilobal fibers promote the wettability of the fibers e.g, decrease apparent contact angle and increase the force required to detach the droplet. We also observed that when the droplets are small the azimuthal orientation of

the fiber plays a more important role in detachment force. Finally, we will close with our overall conclusions in Chapter 6.

Chapter 2. Modeling Effects of Fiber Rigidity on Thickness and Porosity of Virtual Electrospun Mats

2.1 Introduction

Electrospinning has been the focus of countless studies for the past decades for applications such as aerosol filtration, tissue engineering, and catalysis among many others. Electrospinning is a one-step process for producing submicron fibers—fibers one or two orders of magnitude smaller than traditional textile fibers. To date, there is no accurate method for measuring the thickness, and consequently the porosity of a nanofiber mat. This is because the available measurement techniques are mostly suitable either for nano-scale dimensions (e.g., AFM microscopes) or for measurements on scales greater than say 10 μm (e.g., profilometers or indenters), leaving a thickness range of about 1 to 10 μm hard to measure accurately, especially when working with soft and compliant materials like fibrous mats. Accurate determination of the thickness of a nanofiber mat is very important for most applications that take advantage of such materials. Obviously, one cannot know the performance of a nanofiber mat (for particle/fluid separation, for instance) without knowing its most intrinsic properties such as thickness and porosity.

In a typical electrospinning process, a liquid jet (a single filament) is ejected from the surface of a charged polymer solution (or melt) and then driven by the electrostatic forces towards a collector. The charged filament experiences a so-called whipping process in which it follows an erratic trajectory before depositing on a collector [43-46]. The instabilities in the filament are due mainly to the effects of electrostatic repulsions of the charges in the filament and the coulombic forces caused by the electric field [43-47]. It is possible that the electric charges in the filament may

become dissipated in the ambient air due to humidity or other factors during the electrospinning process. However, depending on the polymer structure and the process conditions, it is also possible that some charges remain in the fibers after the fibers are deposited on the collector [48-49]. Unfortunately, the effects of these residual charges on the morphology of a nanofiber mat have not yet been established. One can expect that the residual charges generate some attraction forces between the fibers and the collector. It is not yet known if such attraction forces can play a role in further compressing the fibers together, and thereby decreasing the thickness of an electrospun mat. Given the number of unknowns affecting the formation of an electrospun nanofiber mat, the current study is devised to perhaps shed some light on the possible relationships between the thickness (and porosity) of a nanofiber mat and the properties of its constituting fibers. As such, this work is only a first step in developing a mathematical means for predicting the thickness and porosity of an electrospun mat. As will be discussed later in this paper, our focus in the current study is on the influence of fiber bending characteristics on the morphology of a fibrous mat.

In the remainder of this chapter, we first describe how a mass-spring model is used in our work to represent a fiber in Section 2.2. We then present our algorithm for depositing such fiber on top of one another to form a mat in Section 2.3. We present a comparison between the predictions of our model and the Fourier solution of the Vibrating String problem for validation in Section 2.4. Our results and discussion are given in Section 2.5 followed by the conclusions in Section 2.6.

2.2 Problem Formulations

Our group has been active in developing modeling methods for simulating the 3-D structure of fibrous mats for the past decade [17-18,50-57]. Our previous structure simulations were specifically designed to provide a computational domain for simulating the transport of fluid, particles, and heat through a fibrous material. Such virtual structures need only to be developed on scales comparable to the dimensions of the fibers—about 25 times greater than the diameter of the fibers. On such small scales, one can assume the fibers to remain rigidly straight (modeled as rigid cylinders) across the entire length of the simulation domain. On the other hand, to simulate how the thickness of a fibrous mat grows as fibers continue to deposit on the surface, one needs to consider simulation domains with in-plane dimensions much greater than the fiber diameter. However, in such large domains (accommodating long fibers) a rigid-cylinder may no longer provide an accurate representation of a real fiber and how it interacts with other fibers in the mat. A new modeling approach is therefore needed to capture both the in-plane (if needed) and the through-plane curvature of the fibers. In the current study therefore, we have assumed the fibers to be made up of a continuous array of beads connected to one another by structural and flexion springs and dampers (see Fig. 2.1a).

Our approach to simulate a nanofiber mat here is to treat the fibers as linear viscoelastic materials. The most common linear viscoelastic models are the Maxwell model, in which springs and dampers are connected in series, and the Kelvin–Voigt model, where springs and dampers are connected in parallel [58]. In these methods, the springs and dampers resemble the material's elasticity and viscosity, respectively. The Maxwell model is more suited for a fiber in the liquid/melt state whereas the Kelvin–Voigt is more appropriate for a solid fiber (the case here). This model allows an efficient representation of a fiber's motion through solving the balance of

mechanical forces acting on each bead p_i. These forces are due to the structural and bending springs and dampers (neglecting gravitational forces), as shown in the free body diagram in Fig. 2.1b. For instance, the spring and damping forces between beads p_i and p_{i+1} can be written as

$$\vec{f}^{s}_{i,i+1} = -k_s(\|\vec{p}_i - \vec{p}_{i+1}\| - l_r)\frac{(\vec{p}_i - \vec{p}_{i+1})}{\|\vec{p}_i - \vec{p}_{i+1}\|} \tag{2.1}$$

$$\vec{f}^{d}_{i,i+1} = -k_d(\vec{u}_i - \vec{u}_{i+1}) \tag{2.2}$$

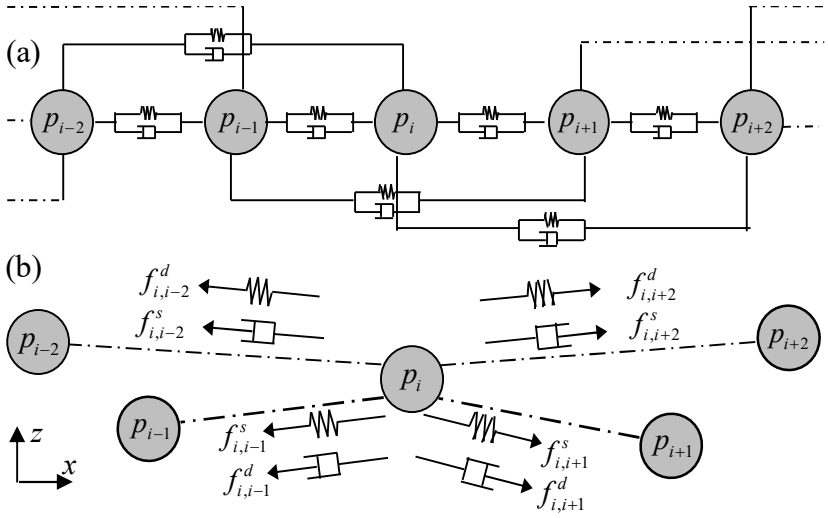

Fig 2.1: (a) The mass-spring-damper model representation of a fiber, (b) free body diagram of a bead.

In the absence of detailed quantitative information with regards to any residual charges in a deposited fiber, the electrostatic forces are not included in our simulations. As will be seen later in this paper however, the possible effects of such forces on the morphology of an electrospun mat are indirectly discussed in this paper. The instantaneous position and velocity of each bead can be obtained by solving Newton's second law for that bead. For a fiber comprised of a finite number of beads, this leads to a coupled system of second-order ordinary differential equations (ODEs).

For the ease of numerical calculations, these second order ODEs are converted into two first order ODEs with respect to position and velocity as,

$$\frac{d}{dt}\begin{bmatrix} v_i \\ x_i \end{bmatrix} = \begin{bmatrix} \vec{f}_i^{\Sigma}/m_i \\ v_i \end{bmatrix} \tag{2.3}$$

where

$$\vec{f}_i^{\Sigma} = \vec{f}_{i,i-2}^{s} + \vec{f}_{i,i-1}^{s} + \vec{f}_{i,i+1}^{s} + \vec{f}_{i,i+2}^{s} + \vec{f}_{i,i-2}^{d} + \vec{f}_{i,i-1}^{d} + \vec{f}_{i,i+1}^{d} + \vec{f}_{i,i+2}^{d} \tag{2.4}$$

The mass of each bead m_i in the fiber can be determined using fiber diameter d and fiber density ($\rho_f = 1000\ \mathrm{kg/m^3}$ here). Assuming $l \gg d$, we obtain,

$$m_i = \frac{\pi l d^3 \rho_f}{4(l+d)} \cong \frac{\pi}{4} d^3 \rho_f \tag{2.5}$$

Note that m_i depends only on the diameter and density of the fibers.

2.3. Algorithm

In this section, our algorithm for simulating the 3-D structure of a fibrous mat is described in detail. As will be discussed later in the section, we produce fiber mats comprised of straight fibers, but allow them to bend at fiber-fiber crossovers (generally in the through-plane direction). The beads are represented with imaginary spheres having a diameter equal to the fiber diameter. These spheres are distributed along the straight length of the fibers with a center-to-center distance equal to the fiber diameter. Accurate simulation of the bending of the fibers at fiber-fiber crossovers is an important yet challenging task that can directly affect the thickness and porosity of a fibrous mat. The extent of bending that occurs at the fiber crossovers depends strongly on the viscoelastic

properties of the fibers as well as the electrostatic and aerodynamic fields during fiber deposition and solidification processes. In the absence of detailed quantitative information with regards to these factors, it is practically impossible to predict the morphology of an electrospun fiber mat. As such, the simulation algorithm developed in the current work is aimed to only shed some light on this complicated problem by studying how fiber bending can affect the porosity and thickness of a fibrous mat. In our simulations, fibers enter the simulation domain horizontally and with an arbitrary initial vertical velocity toward the collection plate. We have assumed the fibers to fall sequentially onto a flat substrate. The μ-randomness algorithm is used to produce fibers with unbiased random positions [59].

The system of ODEs in Equation 3 is solved using the Runge–Kutta 4^{th} order method with a time step of $0.05\ \mu s$. This results in the position and velocity of each bead at each time step during the integration time. At each time step, the algorithm checks whether or not a collision has occurred between the beads of an incoming fiber and those of the already deposited fibers (as well as among the beads of the same fiber). Fiber interpenetration is avoided by monitoring the distance between the beads at each time step to ensure that no beads can come closer to one another by a distance less than a fiber diameter. If two beads are interpenetrating, the distance between these beads at that time step is corrected (moved apart in the direction of the vector connecting them) to become equal to the fiber diameter.

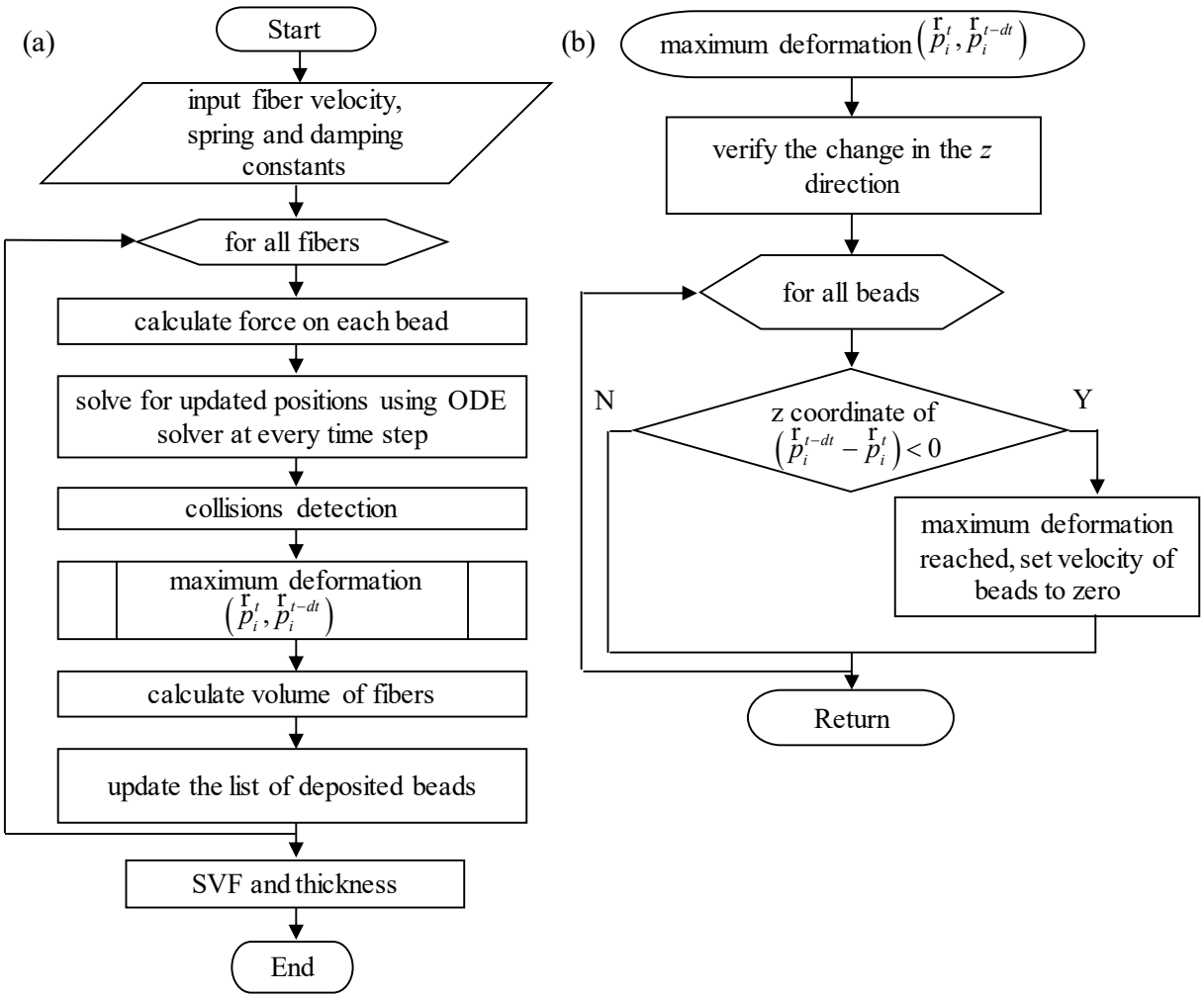

Fig 2.2: (a) The overall flowchart of our algorithm; (b) the flowchart for calculating the maximum deformation of a fiber between two rigid supports.

Once the deposition and bending processes are completed, the fibers are assumed to be rigid. Therefore, the beads in the mat do not move every time a new fiber is deposited. This allows our collision detection algorithm to search for a collision between the beads of a new fiber and those of the deposited fibers (but not among the deposited beads). Obviously, the simulations slow down as additional fibers enter the simulation domain. To overcome this problem, we first produce a sub-list of the deposited beads that may interact with the projected image of an incoming fiber onto the fiber mat. The collision detection search process is then limited to the beads in this sub-

list. Fig. 2.2 summarizes the above algorithm in a flowchart. The thickness of the virtual mats can be predicted using the z-coordinates of the deposited beads (the fibers are in the *x*-*y* plane and the thickness grows in the *z*-direction). To further accelerate the algorithm, a new fiber is introduced to the domain at a height equal to the maximum *z*-coordinate of the deposited beads plus a fiber radius. The length of a fiber in the mat can be obtained by calculating the distance between adjacent beads along the length of the fiber.

2.4. Modeling Single Fiber Deflection

Our algorithm is used in this section to simulate the bending of a single fiber as it deposits on two rigid supports and to compare the resulting deflection with that obtained from the exact solution of the wave equation as it applies to the Vibrating String problem (see Fig. 2.3a). For this comparison, we consider no initial deflection, but assigned an arbitrary initial velocity of $u = -0.05\ \mathrm{m/s}$ in the z-direction to all beads. The solution for the one dimensional wave equation can be obtained using the Fourier series solution given as [60],

$$z(x,t) = \sum_{j=1}^{10} \frac{2u}{cj\pi}\left(\int_0^l sin\frac{j\pi x}{l}dx\right) sin\left(\frac{cj\pi}{l}t\right) sin\left(\frac{j\pi}{l}x\right) \quad (2.6)$$

where l is the fiber length between the rigid supports and c is the speed of the wave, taken to be as 1 m/s here for simplicity. Fig. 2.3b shows the deflection of the fiber obtained from the current model and Equation 2.6 at different times using $k_s/m_i = 8 \times 10^{15}\mathrm{N/(m.kg)}$. Note that a small damping constant $k_d/m_i = 10^3\ \mathrm{N/(m.s^{-1}.kg)}$ is considered for this comparison as Equation 2.6 is derived in the absence of a damping term in the wave equation.

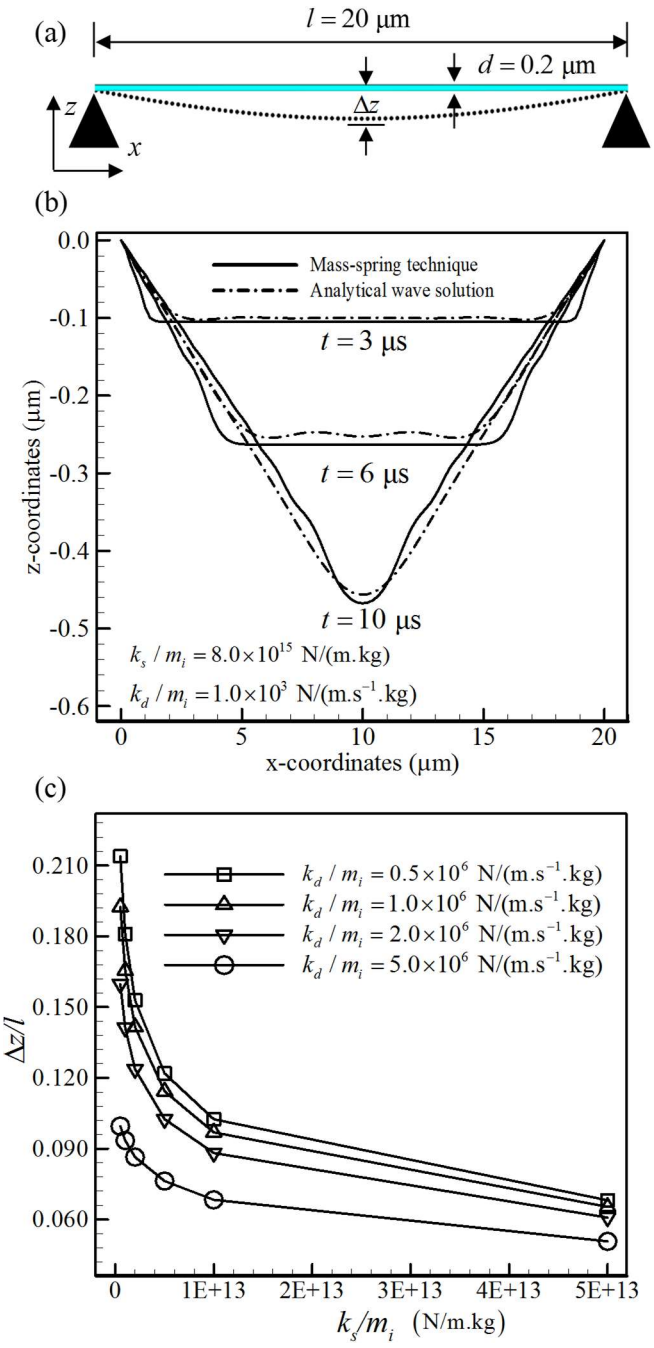

Fig 2.3: (a) Schematic representation of a straight fiber with a diameter of 0.2 μm falling in the z-direction with an arbitrary velocity of $v_i = 0.05$ m/s on two rigid supports separated at a distance of 20 μm; (b) comparison between the predictions of the mass-spring model and the Fourier solution of the wave equation at different time steps; (c) maximum fiber deflection, $\Delta z/l$ for different modeling parameters k_s/m_i and k_d/m_i.

To also study how the spring and damping constants (k_s/m_i and k_d/m_i) affect the bending of a fiber, we varied these parameters for the case shown in Fig. 2.3a, and reported the non-

dimensionalized maximum deflections in Fig. 2.3c. It can be seen that fiber deflection decreases with increasing k_s/m_i or k_d/m_i. Although not reported in this figure, deflection is more when the fiber's initial velocity is higher, as expected.

2.5. Results and Discussion

In our mat formation simulations, we allow the fibers to bend until they reach their maximum deflection in the z-direction, and we then stop them from moving back up. With the lack of quantitative information about the residual charges in a fiber as well as the velocity and solidification state of the fiber at the moment of deposition, this assumption is considered merely to further simplify the otherwise very complicated problem. The simulations in which the fibers are allowed to bend in this manner are referred to as "soft" fiber simulations to distinguish them from the simulations where the fibers were treated as rigid cylinders. The latter is referred to as "rigid" fiber model, and has been the default approach in the almost all the simulations reported previously in the literature [17-18, 50-57,61-68].

In this section, we first study the effects of fibers' in-plane orientation on the solid volume fraction (SVF) and thickness of their mats, and then move on to the more complicated case of mats comprised of fibers with two different diameters. We also simulate the potential effects of an uneven substrate (e.g., a woven screen) on the mat's morphology.

An example of the 3-D virtual electrospun mats generated by our algorithm is shown in Fig. 2.4a. This figure shows a fibrous mat with a basis weight of 2 $\mathrm{g/m^2}$ and $x-y$ dimensions of 0.5 mm by 0.5 mm comprised of fibers having a diameter of $d = 1$ μm. The standard deviation of the in-

plane orientation of fibers about a zero-mean is set to be 30 degrees. The incoming velocity of the fibers was arbitrarily taken to be 0.05 m/s. The modeling parameters used in the simulations were $k_s/m_i = 3.5 \times 10^{14}$ N/(m.kg) and $k_d/m_i = 3 \times 10^6$ N/(μm.s^{-1}.kg). The average thickness and average SVF of the fiber mats produced in these simulations were found to be 19.03 μm and 3.8% respectively. The magnified image in Fig. 2.4b shows the fibers bending at crossovers.

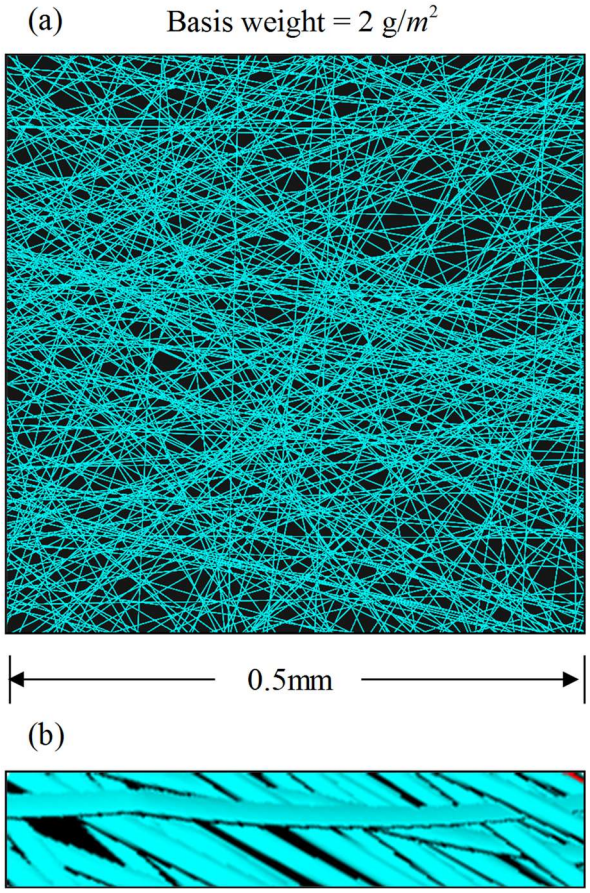

Fig 2.4: A sample virtual mat with a basis weight of 2 g/m^2 made of fibers with a diameter of 1 μm is shown in (a) along with a magnified image showing the fibers bending at crossovers in (b).

Fig. 2.5 shows the effects of fibers' in-plane orientation on a mat's thickness and SVF for both the "soft" and "rigid" fiber models. It can be seen that mats comprised of highly oriented fibers have a lower thickness but a higher SVF. This is because fibers tend to pack closer to one another when

they are highly oriented in a given direction. As can be seen in Fig. 2.5, fiber mats produced by depositing fibers with random in-plane orientations tend to become thicker, and therefore more porous, than mats with aligned fibers having the same basis weight. Fig. 2.5 also shows that for a given in-plane fiber orientation distribution, mats comprised of rigid fibers are more than ten times thicker and more porous than their counterparts made of soft fibers.

The simulation algorithm developed here also allows one to study how thickness and porosity of mats comprised of fibers with different diameters, i.e., mats with multi-modal fiber diameter distributions. In particular, we consider mats made up of fibers with two different diameters, hereon referred to bimodal mats. Such mats can be produced, for instance, by using two simultaneous electrospinning needles each having its own polymer or process conditions. Our virtual bimodal mats consist of coarse and fine fibers with diameters d_c and d_f, respectively. The number fraction of coarse and fine fibers in these mats are denoted by n_c and n_f, respectively.

In a bimodal fibrous material, the coarse fibers often provide mechanical stability, and the fine fibers bring about enhanced surface area. In modeling bimodal electrospun mats, again one has to have quantitative information on how fibers with different diameters retain different amounts of residual charges as they deposit. In the wake of all the unknowns with regards to electrospinning process, we assume that fine fibers retain more residual charges per unit mass and also assume that they bend more at the fiber-fiber cross-sections in comparison to coarse fibers [48].

Fig. 2.6a shows a fibrous mat with a basis weight of $5\ \mathrm{g/m^2}$ comprised of fibers having a fine fiber diameter of $d_f = 1$ μm, coarse fiber number fraction of $n_c = 10$ %, and a coarse-to-fine fiber diameter ratio of $R_{cf} = d_c/d_f = 2$. The fibers are assumed to deposit with an arbitrary initial velocity of 0.05 m/s. Assuming that the coarse and fine fibers have the same material density, according to Equation 2.5, the

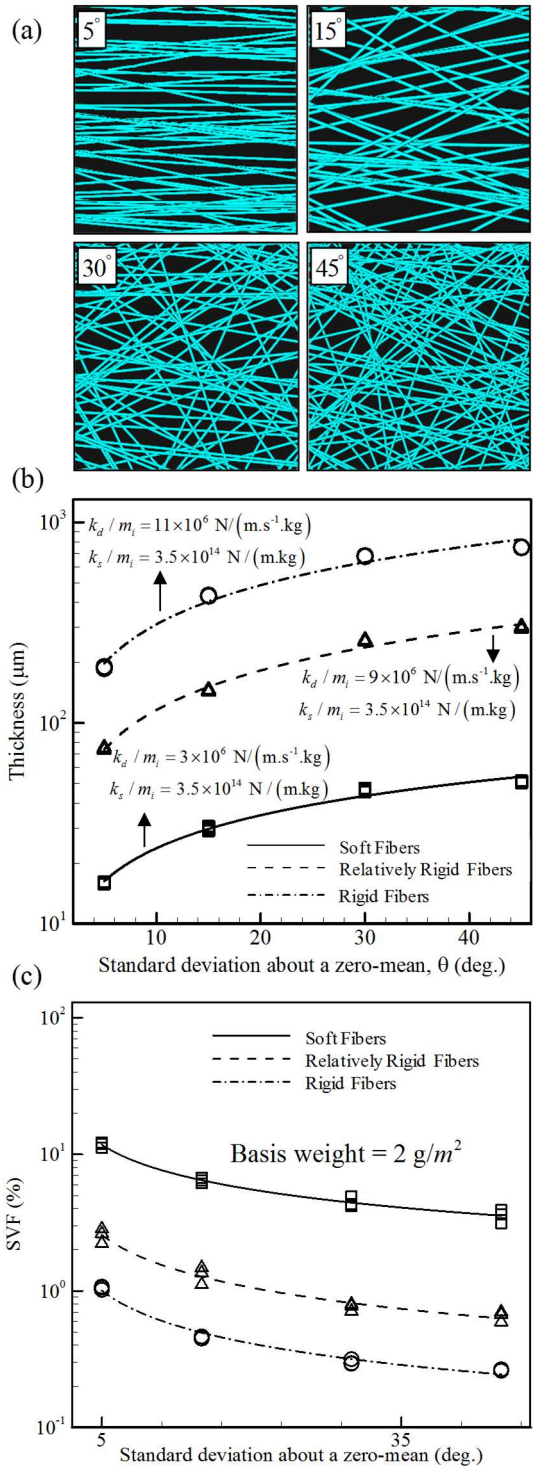

Fig 2.5: Virtual nanofiber mats with different in-plane fiber orientation distributions having a mean zero but standard deviations ranging from 5 to 45 degrees are shown in (a); effects of in-plane fiber orientation thickness (b) and SVF (c) for mats comprised of soft and rigid fibers. Each simulation was repeated three times to ensure that the statistical uncertainties are insignificant.

beads forming a coarse fiber should be heavier than those constituting a fine fiber by a factor of ${R_{cf}}^3$ (i.e., $m_i^c = {R_{cf}}^3 m_i^f$). With the assumption that the coarse fibers are more rigid than the fine fibers, here we considered a spring constant for the former greater than that of the latter by a factor of ${R_{cf}}^3$. This assumption allows us to retain a spring-constant-to-mass ratio of $k_s^c/m_i^c = k_s^f/m_i^f = 3 \times 10^{14}$ N/(m. kg) and a damping-constant-to-mass ratio of $k_d^c/m_i^c = k_d^f/m_i^f = 3 \times 10^6$ N/(m. s^{-1}. kg) for both the fine and coarse fibers. The average thickness and average porosity for the mat shown in Fig. 2.6 were found to be 81.72 μm and 3.76%, respectively. The magnified image in Fig. 2.6b shows the fibers bending at crossovers.

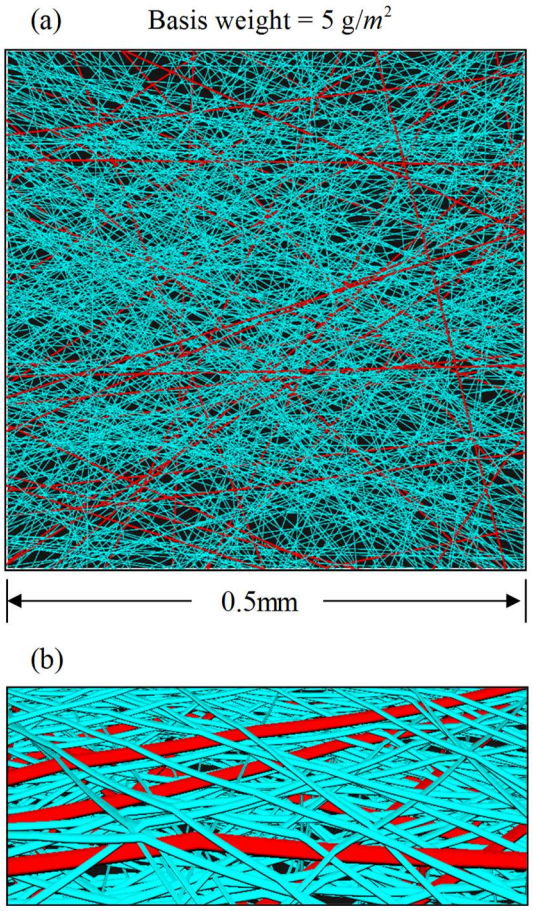

Fig 2.6: A sample bimodal virtual mat with a basis weight of 5 g/m^2 made up of fibers with fine and coarse fiber diameters of 1 μm and 2 μm, respectively is shown in (a) along with a magnified image showing the fibers bending at crossovers in (b).

Figures 2.7a and 2.7b report the simulated SVF and mat thickness for bimodal mats with a constant basis weight of 5 g/m^2 having a fine fiber diameter of $d_f = 1$ μm but varying coarse fiber diameters of $d_c = 2$ μm and 3 μm versus coarse fiber number fraction n_c. The standard deviation of the in-plane orientation of the fibers about a zero-mean was set to 45 degrees for the mats shown in this figure. Figures 2.7c and 2.7d present similar results for similar mats with a fine fiber diameter of $d_f = 2$ μm. The results shown in Fig. 2.7 are obtained for both the soft and rigid fiber models. Interestingly, increasing the percentage of coarse fibers in a bimodal mat made up of soft fibers exhibits a behavior completely different from that of a mat comprised of rigid fibers. For the case of rigid fibers, SVF increases with increasing the percentage of coarse fibers in a bimodal (at a constant basis weight). This is because the thickness of a mat with a fixed mass decreases when the fibers are coarser, i.e., there are less number of fibers in the mat when the fibers are coarse. However, this is not the case with soft fibers. In the case of soft fibers, thickness of the mat increases with increasing the number fraction of coarse fibers. This is because coarse fibers do not bend as much as the fine fibers as discussed earlier. Consequently, SVF of a bimodal mat comprised of soft fibers decreases with the increase of the percentage of coarse fibers. Obviously, if the fibers are softer than the "soft" fibers considered in our simulations, the above effects will be more pronounced. Similarly, SVF decreases with increasing the fiber diameters ratio R_{cf} for constant percentage of coarse fibers for soft fibers (see Fig. 2.7). This is because fibers with a larger diameter tend to bend less, resulting in thicker mats with lower SVFs. This effect is reversed for rigid fibers, as discussed earlier. For the same reason, SVF is higher for mats composed of fine fibers, or fibers with smaller diameters.

With the recent progress in electrospinning process, it is now possible to produce nanofiber mats with orthogonal fibers [69-72]. Orienting the fibers in orthogonal positions allows one to better

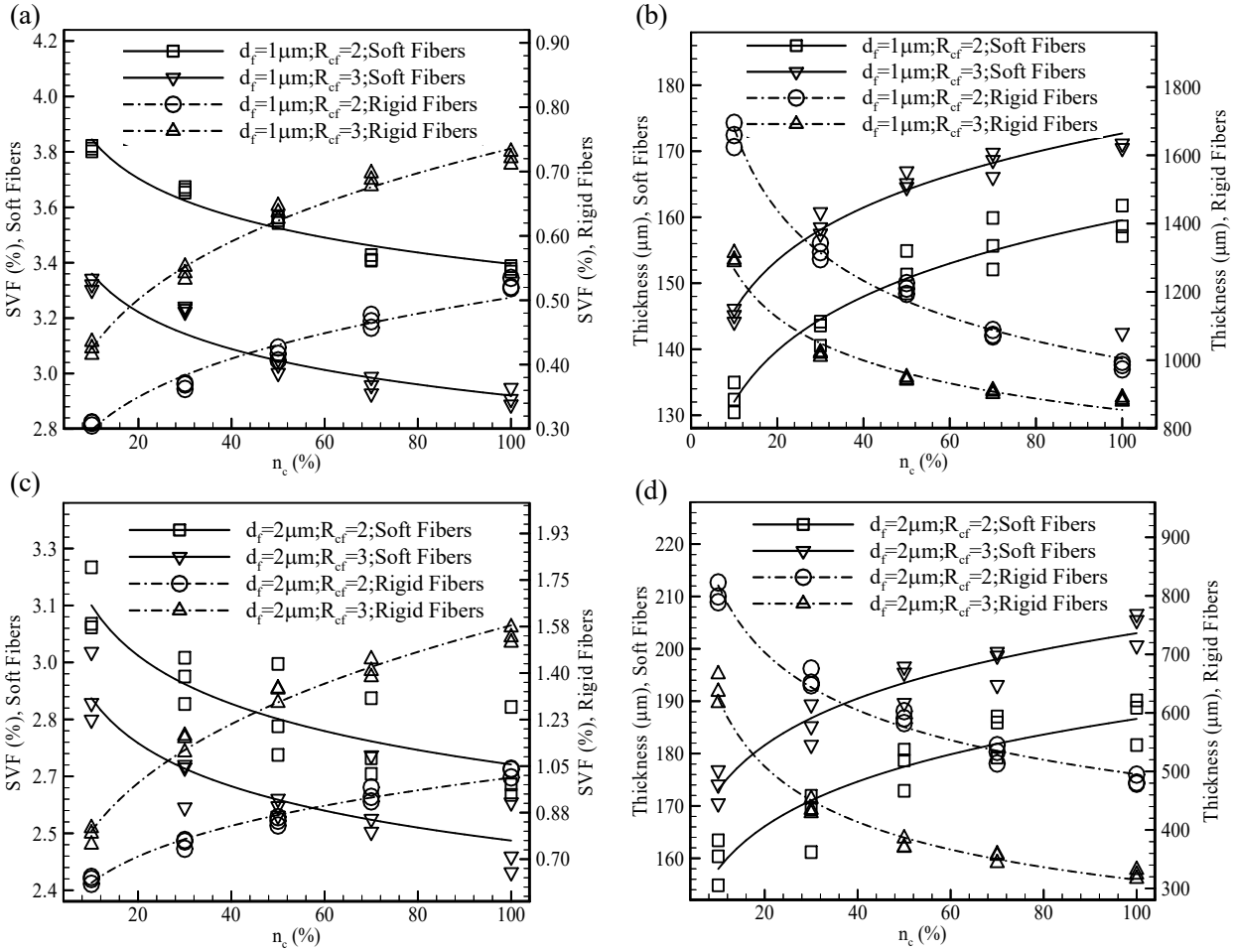

Fig 2.7: Effects of coarse fiber number fraction n_c on SVF (a) and thickness (b) of bimodal mats consisting of fibers with a fine fiber diameter of $d_f = 1$ μm but coarse-to-fine fiber diameter ratios of $R_{cf} = 2$ and 3. Figure (c) and (d) show the same results but for mats with $d_f = 2$ μm. Each simulation was repeated three times.

control the performance of the material in many different applications. For instance, due to the randomness in the orientation of the fibers produced by a classical electrospinning setup, there must always be a greater number of fibers in an electrospun fiber mat than is actually needed to filter particles of a given diameter. Obviously, the presence of additional fibers translates to additional friction with the flow, and therefore results in increased pressure drop. Filter media comprised of orthogonally oriented fibers allows one to reduce the number of fibers needed for

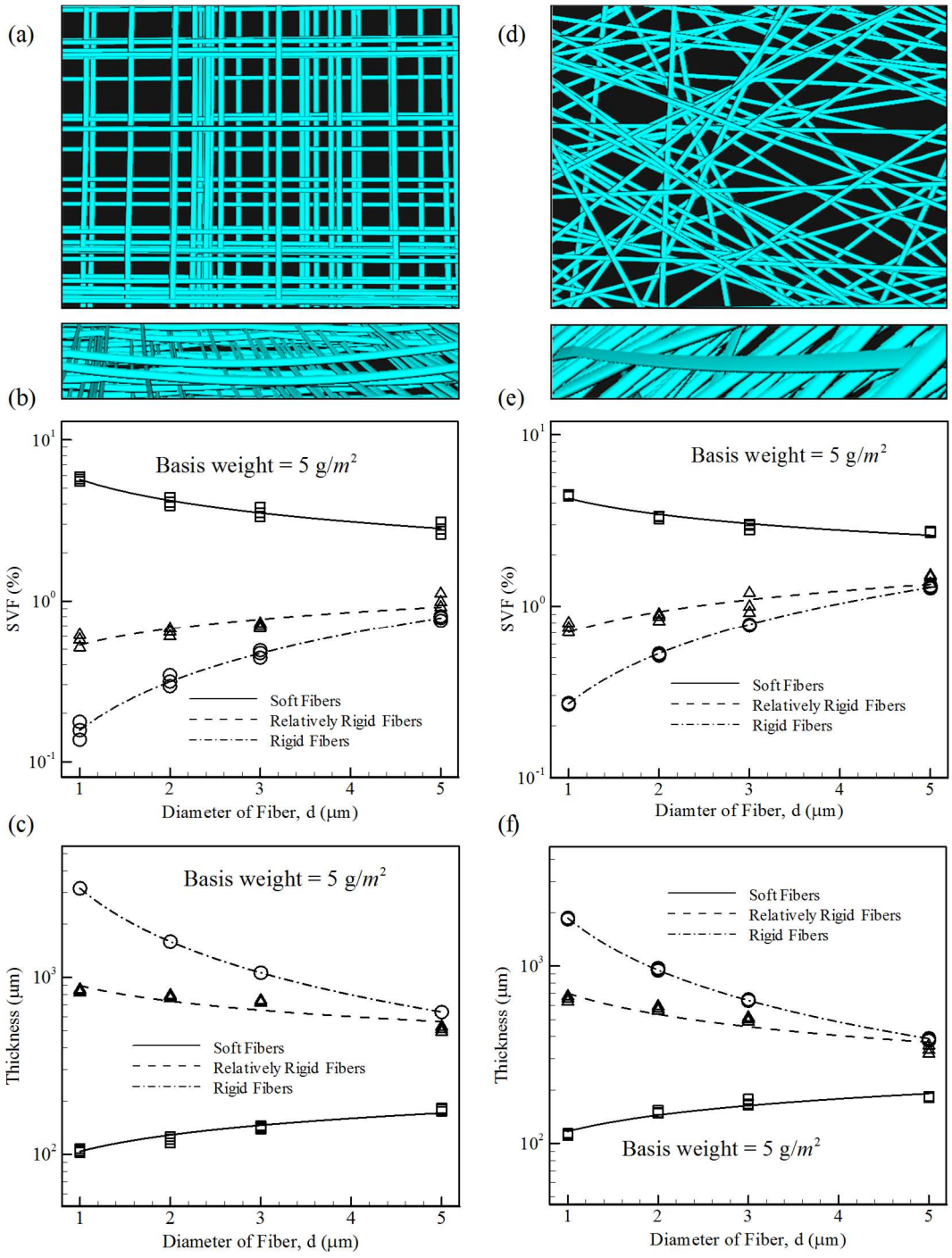

Fig 2.8: A sample nanofiber mat with a basis weight of 5 g/m^2 made of orthogonal soft fibers with a diameter of 1 μm is shown in (a) from two different views. Effects of varying fiber diameter of the fibers SVF and thickness are shown in (b) and (c), respectively, for mats made of orthogonal soft and rigid fibers. The results shown in (d)–(f) are similar to those of (a)–(c) except fibers in these figure have random in-plane orientations (i.e., a 45 degree standard deviation about a zero mean). Each simulation is repeated three times.

filtration, and thereby provides a means for producing filter media with lower pressure drops (e.g., [73-74]).

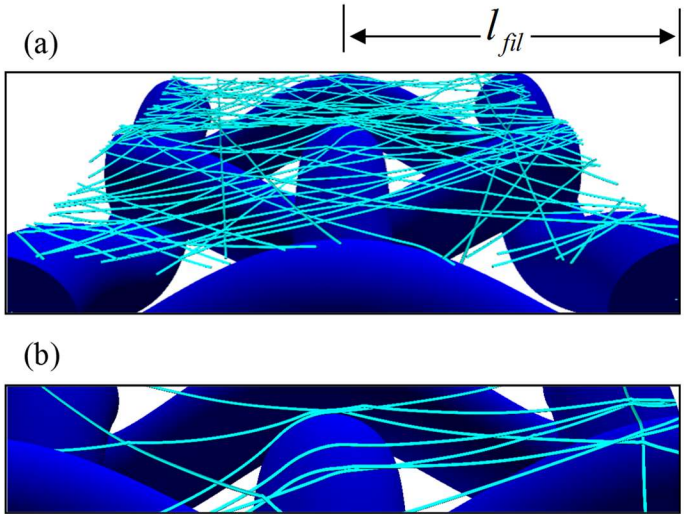

Fig 2.9: Deposition of soft fibers with a diameter of $d = 5$ μm with an arbitrary initial velocity of $v_i = 0.05$ m/s on a monofilament woven substrate from an isometric view (a). The magnified image in (b) shows how the soft fibers conform to the geometry of the substrate.

Figures 2.8a–2.8c show SVF and thickness of fiber mats with orthogonal fibers having a basis weight of 5 g/m^2 but varying fiber diameters. For the sake of simplicity, the deposition sequence of the fibers has been designed in such a way that the orientation of every other fiber will be same. This guarantees that no two fibers will lie in the same horizontal plane. The modeling parameters used here are the same as those mentioned for Fig. 2.5. With this setup, the thickness of a mat comprised of rigid fibers will simply become equal to the number of the fibers in the mat times the diameter of each fiber. With a constant basis weight SVF increases linearly with fiber diameter for rigid fibers while thickness decrease with an inverse proportionality to fiber diameter. On the other hand, for soft-fiber mats having identical basis weights, increasing fiber diameter increases the thickness but decreases the SVF. This is again due to the fine fibers bending more at fiber-fiber

crossovers. Note that in simulating unimodal mats made of fibers with different diameters in Fig. 2.8, we maintained fixed spring-constant-to-mass and damping-constant-to-mass ratios of $k_s/m_i = 3 \times 10^{14}$ N/(m. kg) and $k_d/m_i = 3 \times 10^{6}$ N/(μm. s^{-1}. kg), respectively.

Figures 2.8d–2.8f repeat the study reported in Fig. 2.8a–2.8c but for mats with randomly oriented fibers (45 degrees standard deviation about a zero mean). The simulated SVF and mat thickness show trends similar to those shown in Fig. 2.8b and 2.8c for mats with orthogonal fibers. Note that thickness and porosity of a mat with orthogonal fibers may be higher or lower than those of its random counterpart depending on the number of fibers placed in each layer. For the case reported in Fig. 2.8a–2.8c where only one fiber is allowed in each layer, the thickness and porosity values are higher in mats with orthogonal fibers in comparison to mats discussed in Fig. 2.8d–2.8f.

To further demonstrate the capabilities of the simulation method developed in this work, here we also present the results of simulating fiber deposition on a woven mesh—a typical substrate used to characterize filtration performance of electrospun fibrous mats. The woven screen used for this simulation consists of filaments with a diameter of $d_{fil} = 400$ μm and a filament spacing of $l_{fil} = 500$ μm (as shown in Fig. 2.9). The fibers considered here have a diameter of $d = 5$ μm, an initial velocity of 0.05 m/s, a spring constant of $k_s/m_i = 10^9$ N/(m. kg), and a damping constant of $k_d/m_i = 10^4$ N/(m. s^{-1}. kg). The magnified image in Fig. 2.9b clearly shows how the fibers conform to the curvature of the woven substrate. The modeling method introduced in this work is the only approach to date to simulate the morphology of a fiber mat deposited on an uneven substrate.

2.6. Conclusions

The study presented here is the first to develop an in-house mass-spring-damper model to simulate the thickness and porosity of an electrospun fiber mat in terms of the rigidity of the mats' constituting fibers (and their diameter dissimilarity). In this method, each fiber in the media is treated as an array of beads with a diameter equal to that of the fibers, and connected to one another by a series of spring and dampers. Writing the balance of forces acting on each bead, one obtains a system of second order ODEs that can be solved for the position of the beads, and thereby the profile of the fiber as it deposits on the collector plate or previously deposited fibers.

In the absence of detailed quantitative information with regards to residual charges in electrospun fibers as well as their mechanical properties, we treated the fibers as "soft" or "rigid" to illustrate how fiber bending at fiber-fiber crossovers can affect the thickness and porosity of a nanofiber mat. This allowed us to observe an effect that has never been reported previously: for fibrous mats with identical weights, the thicker and more porous mat is not necessarily the one comprised of smaller fibers. Depending on how diameter of a fiber influences its tendency to bend at fiber-fiber crossovers, a fibrous mat made of fine fibers may or may not be more porous than its counterpart composed of coarser fibers.

The effects of fiber diameters dissimilarity in bimodal fibrous mats are simulated in this paper. It was found that porosity and thickness of bimodal mats with constant weight increases with increasing the fraction of the coarse fibers in the mats or the coarse-to-fine fiber diameter ratio, if fine fibers tend to bend more than the coarse fibers at the fiber-fiber crossovers (the soft-fiber

model). This trend reverses if the fibers are rigid. Our simulations also indicated that porosity is lower in mats where fibers are highly oriented in a certain direction.

Chapter 3. Failure Pressures and Drag Reduction Benefits of Superhydrophobic Wire Screens

3.1 Introduction

Superhydrophobic (SHP) surfaces, often produced by incorporating single or multiscale roughness into a hydrophobic material, are known for their ability to reduce the area of contact between water and the solid surface (referred to here as the wetted area). The reduced wetted area, in turn, brings about peculiar attributes that are essential for applications such as self-cleaning [1,75,2] and drag-reduction [81-85] to name a few. Given the prohibitive cost associated with large-scale production of microfabricated SHP surfaces, woven screens enhanced with functional surface treatments/coatings have recently be considered as a cost-effective alternative for producing a SHP porous surface in many applications. SHP woven screens can be used for drag reduction [3,23,79-80], oil–water separation [4,26,81-83], self-cleaning and anti-icing [5-6,84], underwater protection of electronic devices [85-86], water harvesting [7], and heat transfer [8] among many other applications. There have also been interesting studies on the lead-carrying properties of SHP wire screens for device manufacturing [87-91].

Performance of a SHP surface depends on the mechanical stability of the air–water interface (AWI) that forms over the non-wetting pores of the surface upon contact with water. Depending on surface geometry and hydrostatic/hydrodynamic pressure, the AWI can ingress into the space between the wires to allow the Wenzel state (fully wetted), the Cassie state (fully dry), or a series of transition states in between the two extreme states to prevail over the surface. The main forces acting on an AWI are the hydrostatic/hydrodynamic pressure and the capillary pressure (see [22,92] for more detailed information). The hydrostatic pressure at which a SHP surface starts departing from the

Cassie state is referred to as the critical hydrostatic pressure (CHP) [22]. This definition is often used in the context of pores with sharp-edged entrance where the AWI can anchor (pin) itself to the edges of the pore. The definition is less clear when the pore entrance is round (the case with wire screens). This is because in this case, the AWI cannot anchor itself to any sharp corner, and has to conform to a shape that maintains the YLCA at any point along the curved walls of the pore. Therefore, even at a zero hydrostatic pressure, it is hard to define a fully dry (Cassie) state. Obviously, the AWI moves further down into the pore in response to any increase in the hydrostatic pressure [22]. For the lack of a better alternative, we define CHP for a pore with round entrance, to be the hydrostatic pressure at which the AWI moves down into the pore such that the pore's capillary pressure reaches its maximum value (referred to here as the breakthrough pressure) denoted with P_{brk} (see [5,20] for more detailed information). Transition to the Wenzel state can also occur if the AWI touches the bottom of the pore under pressure. This has been identified in the literature as failure due to AWI sagging or the lack of "robustness height" [12]. For applications in which a wire screen is used as a coating placed on a surface (e.g.,[4,23,79-80] and [6,84]), we consider sagging to be the failure mechanism and the pressure associated with this pressure is shown with P_{sag}. On the other hand, for applications in which a wire screen operates as a barrier between two different fluids or two different compartments (e.g., [5,7,26, 81-83, 85-91]), we consider failure to be the condition where the pressure over the screen exceeds the breakthrough pressure.

In the remainder of this chapter, we first present our numerical approach for predicting the wetted area and failure pressures of SHP wire screens in Section 3.2. We then discuss our custom-designed setup for testing a screen's breakthrough pressure in Section 3.3. In Section 3.4, we

present available expressions for calculating the slip length over a SHP wire screen. Finally, our results and discussion are given in Section 3.5 followed by our conclusions in Section 3.6.

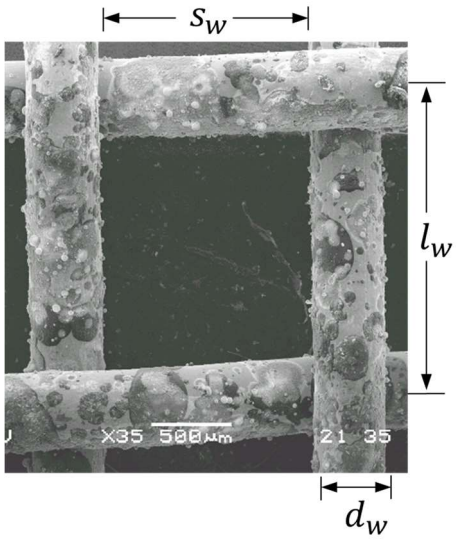

Fig 3.1: An example SEM image of the superhydrophobic wire screens considered in the study.

3.2 Predicting Wetted Area and Failure Pressures

In our simulations, sagging pressure, breakthrough pressure and slip length are calculated for simple square-weave wire screens (same number of wires per unit length in both directions). These screens are generally described by the geometric parameters: spacing between the wires s_w, diameter of the wires d_w, and the center to center distance between the wires l_w, as can be seen in Fig. 3.1. The Surface Evolver (SE), finite element code, is used in our study to determine the shape and position of the AWI under elevated hydrostatic pressures [93]. The screen is simulated by modeling a unit cell of the repeating geometry using symmetry boundary conditions on the planes slicing through the center line of the consecutive wires in the *x* and *y* directions (see Fig. 3.2a). The general form of energy equation for an AWI can be expressed as [9],

$$E = p\iiint dV - \sum \sigma \cos\theta_i \iint dA_i \tag{3.1}$$

where p is the pressure difference across the interface, σ is the surface tension, θ represents the Young–Laplace contact angle (YLCA). The surface energy associated with the wires depends on the water–solid surface area and it is described by the second term on the right hand side of Eq. 3.1. The area integral term in Eq. 3.1 should explicitly be defined for the SE. Fig. 3.2b shows the wetted area of a wire in a screen in the $x-y$ plane with the top of the wires placed at the $z=0$ plane. The AWI penetrates into the space between the wires in response to an increase in the water hydrostatic pressure. At the equilibrium position at an angle α from the top, the AWI is symmetrically draped over the top of the wire (see Fig. 3.2c). Note that the AWI touches the wire at point D making an angle α with the vertical axis (angle ABD). A wire oriented in the *x*-direction can mathematically be described as sine wave $\left[z-\frac{d_w}{2}\left(\sin\left(\frac{\pi}{l}x+\varphi\right)-1\right)\right]^2+y^2=\left(\frac{d_w}{2}\right)^2$ with φ being the phase shift (in radian) from the origin (point A). For such a wire, the area element dA_i can be written as

$$dA_i = d_w \alpha F_l dx \tag{3.2}$$

where $F_l=\sqrt{1+\left[f'(x)\right]^2}$ with $f(x)=\frac{d_w}{2}\left[\sin\left(\frac{\pi}{l}x+\varphi\right)-1\right]$ is the z-coordinate of the wire centerline. Also, the angle α is a function of $f(x)$ according to [77]

$$\alpha = \cos^{-1}\left(1-2f(x)/d_w\right) \tag{3.3}$$

The above-mentioned equations (Eqs. 3.2–3.3) can be modified for the case where the wire is aligned in the $y-$ direction by replacing x with y. Attention should be paid to how the volume

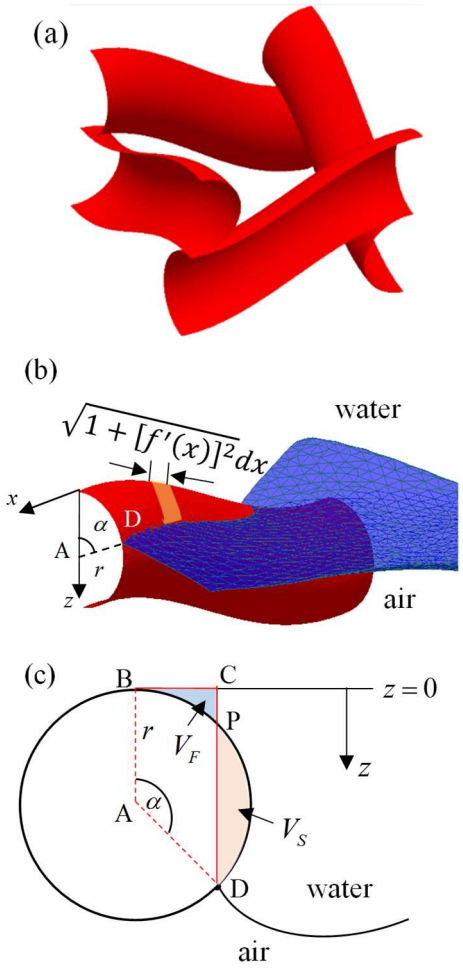

Fig 3.2: Virtual unit-cell of a wire screen used in SE calculations (a). The area (b) and volume (c) elements used in deriving the energy equation for the system

integral term on the right hand side of Eq. 3.1 is defined for SE. To obtain the volume of the fluid above AWI correctly, one should subtract the volume of the portion of the wire V_S (orange color) overlapping with the volume obtain by projecting the AWI onto the $x-y$ plane ($z=0$) from AWI contact point (point *D*) as shown in Fig. 3.2c. Then, the volume of the fluid restricted by lines *CD* and *AB* above the wire V_F (blue color) has to be added in the volume integral term. Finally, the volume integrand in Eq. 3.1 is modified by adding $V_F - V_S$ to become,

$$dV = \left[-\frac{1}{8} {d_w}^2 \alpha + \frac{2z + d_w}{8} d_w \sin\alpha \right] \sqrt{1 + \left[f'(x) \right]^2}\, dx \tag{3.4}$$

Figures 3.3a–3.3d show the simulated AWI over a wire screen under different hydrostatic pressures. The wires have an YLCA of $\theta = 123^{\circ}$, a spacing of $s_w = 458$ μm, and a diameter of $d_w = 254$ μm. At low pressures, the meniscus merely touches the surface of the wires, but it penetrates deeper into the spacing between the wires as the pressure increases. In this work, we mainly focus on estimating the sagging pressure P_{sag} and breakthrough pressure P_{brk} for SHP screens with different dimensions. The sagging pressure P_{sag} is defined here as the pressure at which the AWI touches the flat substrate underneath the wire screen (Fig. 3.3c). The breakthrough pressure P_{brk} on the other hand, is defined here as the highest pressure that the AWI can tolerate before the AWI break up allowing water to flow through the screens (the maximum capillary pressure) as shown in Fig. 3.3d. As will be seen later in this paper, these pressures will be predicted for wire screens with different geometries and YLCAs. We also report the screens' wetted area at different hydrostatic pressures. We define the wetted area fraction A_w of a screen as the ratio of the screen's wetted area from Eq. 3.1 to the unit cell area of the screen l_w^2.

To ensure that the AWI predictions reported in this paper are not affected by the choice of mesh density, the wetted area fraction for a screen having a wire diameter of $d_w = 140$ μm, a wire spacing of $s_w = 458$ μm, and an YLCA of $\theta = 123^{\circ}$ was calculated at different hydrostatic pressures using a uniformly distributed triangular mesh elements. The mesh density was then increased incrementally and its effects on the wetted area as well as sagging and breakthrough pressures were recorded. It was found that simulations performed with a mesh density of $L / d_w > 500$ (where

L is the grid-points interval size) produce numerical results with less than about 5% mesh dependence (not shown for the sake of brevity).

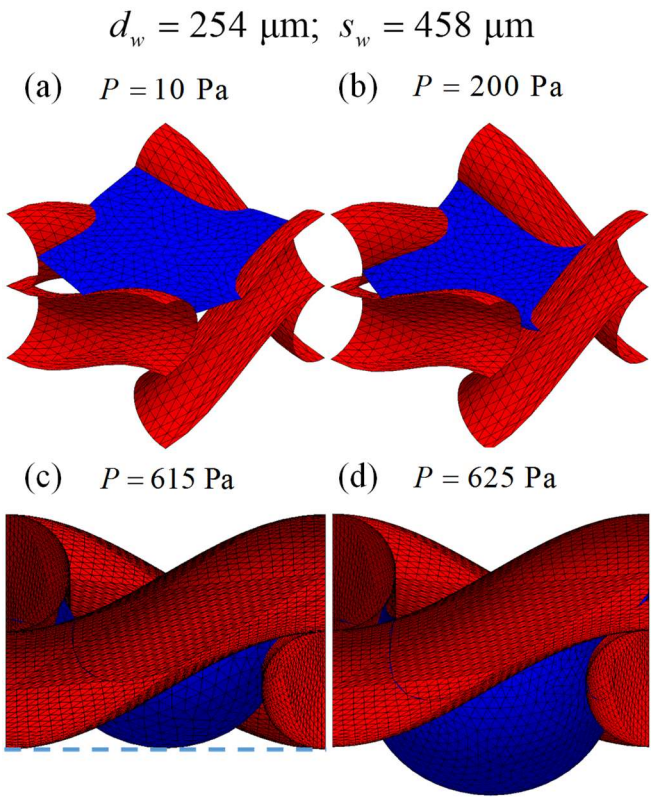

Fig 3.3: Sample simulation results showing the AWI under different hydrostatic pressures in (a) and (b). Failure due to AWI sagging is shown in (c). Failure due to AWI breakup at the breakthrough pressure is shown in (d). Here $d_w = 254$ μm and $s_w = 458$ μm.

3.3 Breakthrough Pressure Measurement

An experimental setup was built to determine the breakthrough pressure of the SHP wire screens for model validation. Four different wire screens were purchased from McMaster-Carr and cut into 2 inch by 2 inch samples. The screens were then sprayed with a commercially available hydrophobic coating (Ultra-Ever Dry by Ultratech Company). Prior to spraying the screens, the coating was applied on a glass slide and an average YLCA of 123 degrees was obtained (see Fig.

3.4). To coat the screens, an adhesive coating was first applied to each side of the screens using a sprayer bottle held 3 inches away and the screens were left to dry for 30 minutes. After the bottom coat had sufficiently dried, a top coat was sprayed on using another sprayer. The coating was sprayed in a fine mist and in a consistent way to maximize the uniformity of the coating to the extent possible. Attention was also paid to not apply excessive amount of coating onto the screens so that their geometry remain unaffected. Nevertheless, differences in the amount of coating applied to the various screens could account for some minor aberrations in the results. The screens were left to dry for 24 hours before being used in the experiment. Several screens of each size to be tested were coated to obtain statistically meaningful measurements. Occasionally, a film of hydrophobic coating would form a film across one or numerous pores in the screen. These screens were excluded from the experiment to create consistency and accuracy in the experimental data.

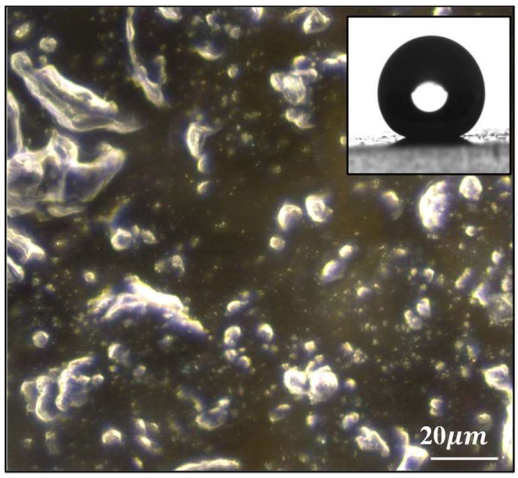

Fig 3.4: An SEM image of the superhydrophobic spray-on coating used on a microscope slide. The inset shows droplet contact angle measured via a goniometer.

To measure a screen's breakthrough pressure, a test setup was designed and built (see Fig. 3.5a). The setup consists of a vessel made of an acrylic cylinder that is fed with water at a defined

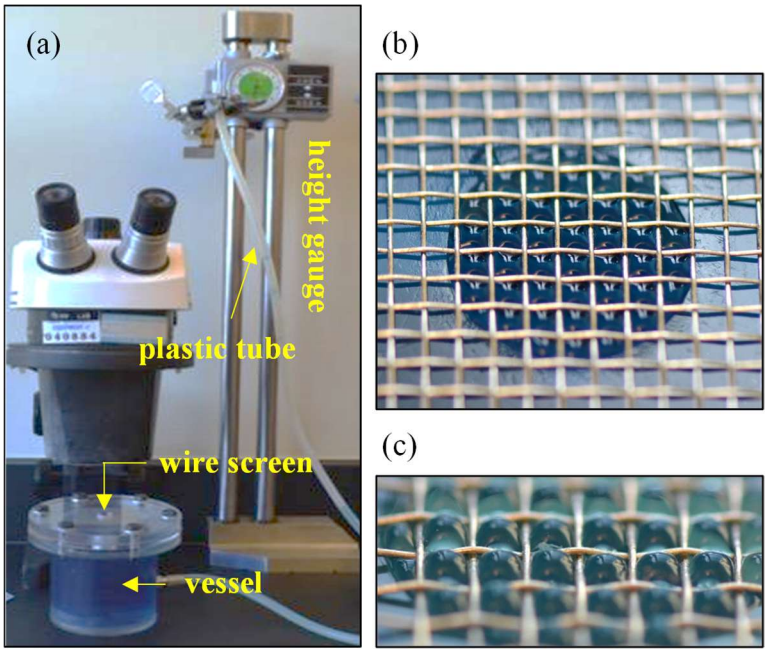

Fig 3.5: Our experimental setup designed to measure the breakthrough pressure of SHP woven screens (a). Optical images of AWI trying to enter a SHP screen at low (b) and high (c) magnifications.

pressure. The pressure of water is adjusted by changing the height of the water in a tube. The top of the chamber is comprised of the holder where the screen can be mounted. The screen was placed on top of the vessel and then a hydrophobic o-ring centered on the hole in the middle of the plate. A clear circular plate was then placed on top of the o-ring and the screen before fastening the top plate to the rest of the vessel. The height gauge was adjusted until the water level reached the surface of the screen and the manometer level became stable. The height gauge was then zeroed and the microscope was positioned over the pressure vessel. A possible variation in the results could have resulted from inconsistencies in this zeroing because it was a judgment based on visual observation and could vary slightly from trial to trial. The level of the height gauge was slowly elevated until it was observed through the microscope that the water had penetrated the hydrophobic coating of the screen. The elevated hydrostatic pressure could then be calculated as

$P_{brk} = \rho g h$ where ρ is the density of water, g is the gravitational acceleration, and h is the height of the water column in the tube. The maximum water (dyed with food coloring to allow a more definable interface) level that a SHP screen can withstand without water breaking through was measured optically [86]. The AWI breaking through the screen can be seen in Figs. 3.5b and 3.5c. In order to eliminate the potential edge effects, results were only considered from trials in which the water penetrated the screen from a pore that was not directly touching the pressure vessel. The screen was removed and the vessel was dried so that the next trial can be conducted. The screen, o-ring and both flanges had to be completely dried in order for an accurate trial to be conducted.

3.4 Slip Length Prediction

3.4.1 Flow Field Calculation

As mentioned earlier, the AWI formed over the pores of a SHP surface can provide drag reduction benefits for a submerged surface. A body of water flowing over a SHP wire screen experiences frictional (no-slip) contact with the solid wires and slippery (no shear) contact along the AWI (see Fig 3.6a). Overall, one can expect a reduction in the skin-friction drag of a solid surface due to a reduction in the surface wetted area upon using a SHP screen. The decrease in the skin friction drag is often portrayed by the effective slip length, which is the average distance underneath the water–solid interface at which the velocity extrapolates to zero (refer Fig. 3.6b). As discussed before in Sec. 3.2, the shape and position of the AWI over a SHP wire screen can be obtained from SE simulations at different pressures. This information can be used to predict the slip length over such surfaces by solving the Navier–Stokes equation in a Couette geometry such as the one shown in Fig. 3.6 (note the periodic and symmetric boundary conditions in the streamwise and lateral directions, respectively). A laminar flow is induced by moving the upper plate with a velocity of

0.1 m/s in the x-direction. Unless otherwise stated, the distance between the SHP surface and the upper plate is considered to be $H = 5d_w$ in all the simulations reported here. The flow field is obtained using the

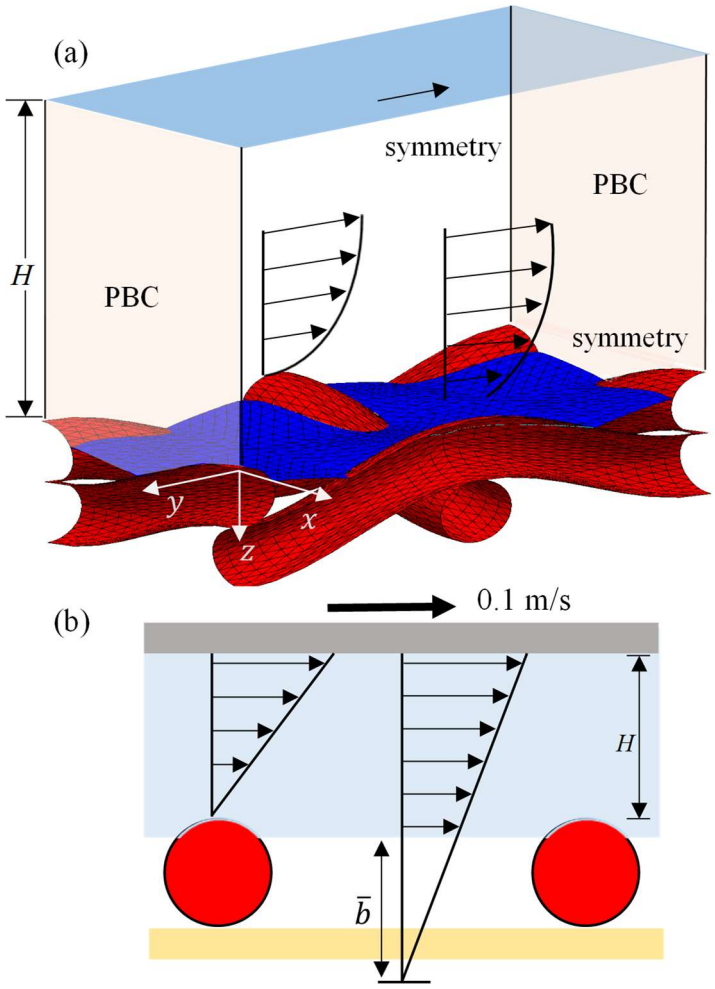

Fig 3.6: The computational domain considered for solving the Navier–Stokes equations using an accurate estimate of the 3-D shape of the AWI over the screens (a). Schematic diagram describing the slip length concept (b).

finite volume FLUENT software. The computational domain was meshed using tetrahedral mesh refined near the AWI to reduce the total number of volume mesh (i.e., CPU time) required to obtain a reliable flow field between the plates. In addition, regional mesh adaption was considered near

the AWI or the upper plate whenever it showed to further improve the slip length predictions. A mesh-independence study was also conducted (with $d_w = 140\ \mu m$, $s_w = 458\ \mu m$, and YLCA $\theta = 123°$ at a hydrostatic pressure of 100 Pa) to examine how our predicted effective slip length values vary with the total number of volume mesh N used in our flow field simulations (not shown for the sake of brevity). It was found that simulations conducted with more than 1.5 million tetrahedral mesh (with the near-AWI refinement) had negligible dependence on the total number of volume mesh. Additional regional mesh adaptation was considered whenever needed to further improve the accuracy of our slip length calculations.

3.4.2 Slip Length Calculation and Validation

The most practical way of defining an effective slip length is what one may observe in a rheometer experiment with the SHP wire as the bottom plate. In this configuration, the drag benefits of a SHP wire can be examined by the reduced torque (shear stress) needed to spin the upper plate [23],

$$\bar{b}_{up} = \left(\frac{\tau_{flat}}{\tau_{slip}} - 1\right) H \tag{3.5}$$

where τ_{flat} is the conventional Couette flow shear stress at the upper plate (in the absence of a SHP bottom plate), and τ_{slip} is the shear stress at the upper plate with the SHP wire screen as the lower plate. An approximate analytical effective slip length expression is also provided in [3] for flow over SHP screens, as

$$\bar{b}_{app} \approx \frac{l_w}{3\pi} \ln\left(\frac{2\left(1+\sqrt{1-A_w}\right)}{\pi A_w}\right) \tag{3.6}$$

According to this equation, effective slip length is positive for $A_w < 0.868$, and negative when $0.868 < A_w \leq 1$. To the knowledge of the authors, the only analytical work that can be used to validate our numerical slip length calculations over SHP wire screens is the work of [3] who proposed an effective slip length expression as,

$$\bar{b}_{flat} = l_w(a_1 \ln \varepsilon + a_2) \tag{3.7}$$

where $\varepsilon = d_w / l_w$, $a_1 = -0.107$, and $a_2 = -0.069$, with the solid area fraction defined as $A_w = \varepsilon(2-\varepsilon)$

.

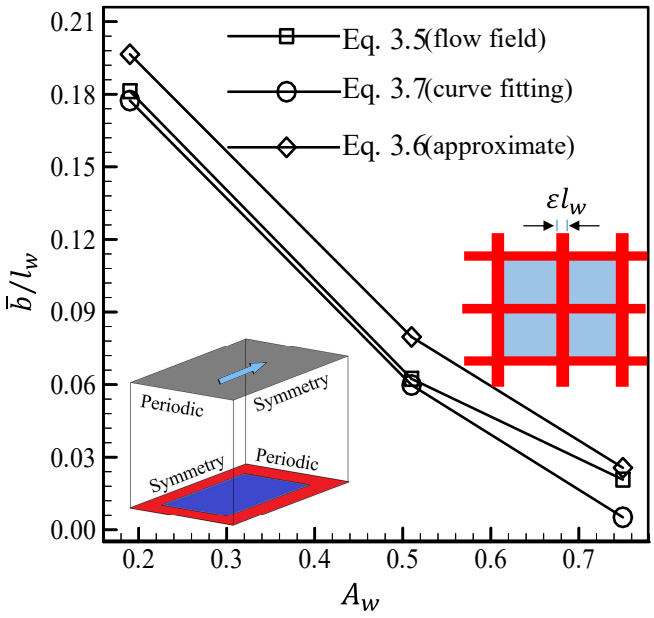

Fig 3.7: Dimensionless effective slip length values calculated for screens with different area fractions. An oversimplified representation of the screens geometry in considered here to compare the results of our numerical calculations with those of [8] for validation purposes.

The effective slip length expression of [3] treats the wire screen as a 2-D planar surface (i.e., no curvatures is considered for the AWI or the wires). Therefore, our simulation domain was simplified to numerically duplicate the geometry of screen as considered in [3]. The simulation domain and the resulting slip

length values from Eq. 3.5 are given in Fig. 3.7 along with those of Eqs. 3.6 and 3.7. For these calculations wire screens with a unit cell length of $l_w = 636\ \mu\text{m}$ but varying solid area fractions of $0.19 < A_w < 0.75$ were considered. Good agreement can be seen between the three approaches taken to predict an effective slip length for flow over a SHP wire screen treated as a 2-D geometry comprised of flat wires accommodating a flat AWI (i.e., a flat plate perforated with square holes having sharp edges).

3.4 Results and Discussion

In this section, we discuss how diameter and spacing of the wires in a screen can impact a screen's sagging and breakthrough pressures as well as its wetted area and slip length. We will compare the results of numerical simulations with those obtained from our experiment whenever possible.

Figure 3.8 shows the effects of wire spacing on sagging and breakthrough pressures for screens with different wire diameters of d_w = 254 and 508 μm. It can be seen that both pressures decrease when increasing the spacing between the wires. The decreasing trend can be better understood by considering the fact that the AWI contact line (providing capillary forces) scales almost linearly with the wire spacing whereas AWI area (exposed to hydrostatic pressure) scales with the wire spacing squared. Therefore, increasing wire spacing weakens the resistance of a screen to an intruding AWI. More interesting in this figure is the difference between the breakthrough and sagging pressures. While in most cases sagging pressure is smaller than the breakthrough pressure, it is quite possible for this trend to reverse especially at small wire spacing values (i.e., AWI gives in before it comes into contact with the underlying substrate) as shown with blue shade in Fig. 3.8a and Fig. 3.8b for $s_w < 254\ \mu\text{m}$ and $s_w < 762\ \mu\text{m}$, respectively. In such cases, the breakthrough

pressure is taken as the failure pressure. Figure 8 also shows the effects of wire spacing on the screens' wetted area fraction at sagging and breakthrough pressures. It can be seen that wetted area

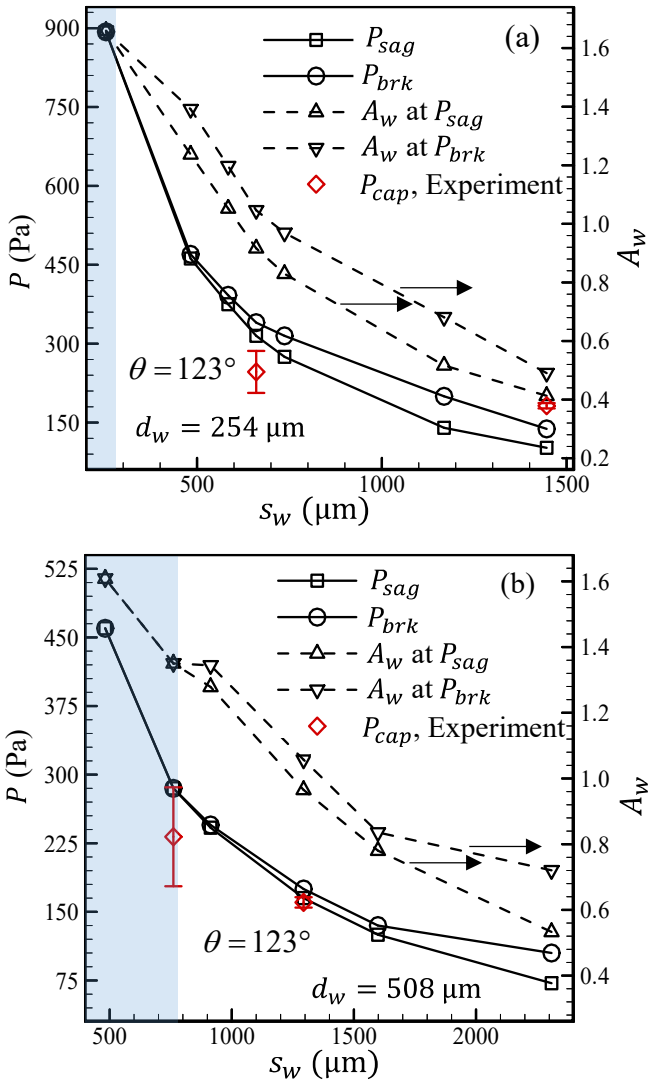

Fig 3.8: Effects of wire-to-wire spacing s_w on failure pressure (breakthrough and sagging pressures) and wetted area fraction of the screens having constant wire diameters of $d_w = 254$ µm (a) and $d_w = 508$ µm (b). Experimental breakthrough pressure values (red symbols) are added to the figures for comparison.

fractions decrease with increasing wire spacing. This is because the unit cell area of a screen increases faster with increasing wire spacing than does the wires' wetted area. The breakthrough pressures obtained from our experiments are shown in Fig. 3.8a ($s_w = 660$ µm and $s_w = 1448$ µm)

and Fig. 3.8b (and $s_w = 762$ μm and $s_w = 1296$ μm) with red symbols. The experimental data seem to follow the numerical predictions slightly better for screens with larger wire spacing. This appears to be caused by the inaccuracies involved in tracking the AWI experimentally (i.e., optically) when the wire spacing is smaller.

Comparing screens with identical wire spacing but different wire diameters in Fig. 3.8, it can be seen that both the sagging and breakthrough pressures are generally higher for screens with bigger wire diameters especially when the spacing is large. For instance, for a wire spacing of $s_w = 1446$ μm, the sagging and breakthrough pressures are found respectively to be $P_{sag} = 102$ Pa and $P_{brk} = 138$ Pa, for the screen having a wire diameter of $d_w = 254$ μm (Fig. 3.8a), and $P_{sag} = 135$ Pa and $P_{brk} = 160$ Pa for the screen with the wire diameter of $d_w = 508$ μm (Fig. 3.8b). For a smaller spacing of $s_w = 746$ μm however, these pressures are predicted to be $P_{sag} = 275$ Pa and $P_{brk} = 300$ Pa for the screen with the wire diameter of $d_w = 254$ μm, and $P_{sag} = P_{brk} = 300$ Pa were for screen with the wire diameter of $d_w = 508$ μm.

Figure 3.9 shows the effects of pressure on wetted area fraction and effective slip length of wire screens with different geometries. Two sets of data are generated for this study; one in which the spacing is varied, while the wire diameter is held constant at $d_w = 254$ μm (Figs. 3.9a and 3.9b), and the other where spacing is fixed at $s_w = 178$ μm but the wire diameter is varied (Figs. 3.9c and 3.9d). As expected, wetted area fraction increases with pressure for both cases (see Fig. 3.9a and 3.9c). More interestingly, at a constant pressure (say, $P = 150$ Pa), wetted area fraction is found to be larger for screens with larger wire diameters or smaller wire spacing. This information is used in Eq. 3.6 to predict the effective slip length of the surface. Effective slip length can also be

predicted (more accurately) using Eq. 3.5 after solving the Navier–Stokes equations in a Couttee

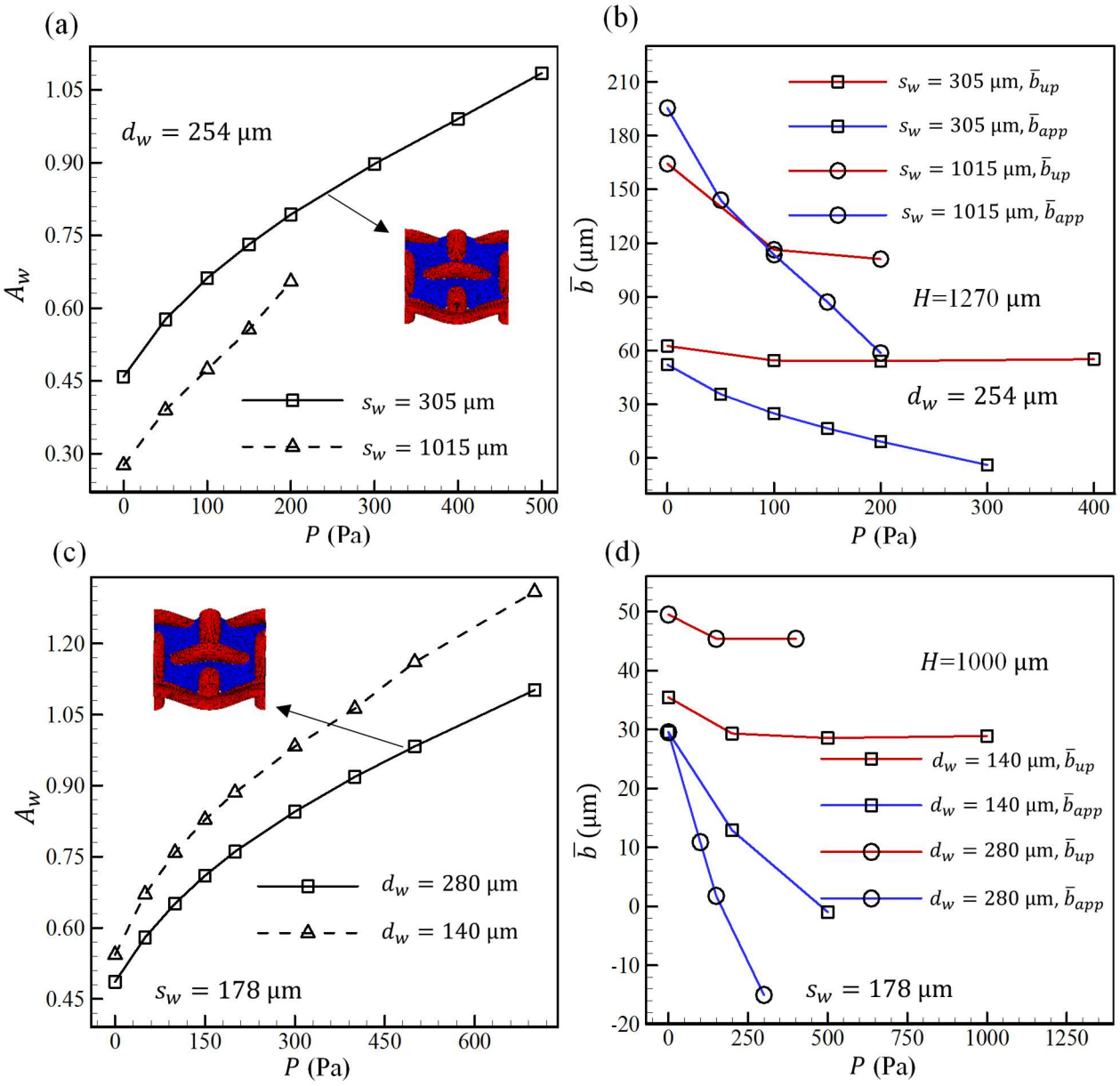

Fig 3.9: Effects of hydrostatic pressure wetted area fraction (a and c) and slip length (b and d) for screens with different geometries. Slip length predictions of Eq. 3.5 ($\bar{b}_{up}$) and Eq. 3.6 ($\bar{b}_{app}$) are compared with one another.

geometry. Figures 3.9b and 3.9d compare the slip length predictions of these two equations with one another. It can be seen that Eq. 3.5 predicts a decreasing slip length which reaches a plateau beyond some pressure (around 100 Pa in Fig. 3.9b and 250 Pa in Fig. 3.9d). To better explain this,

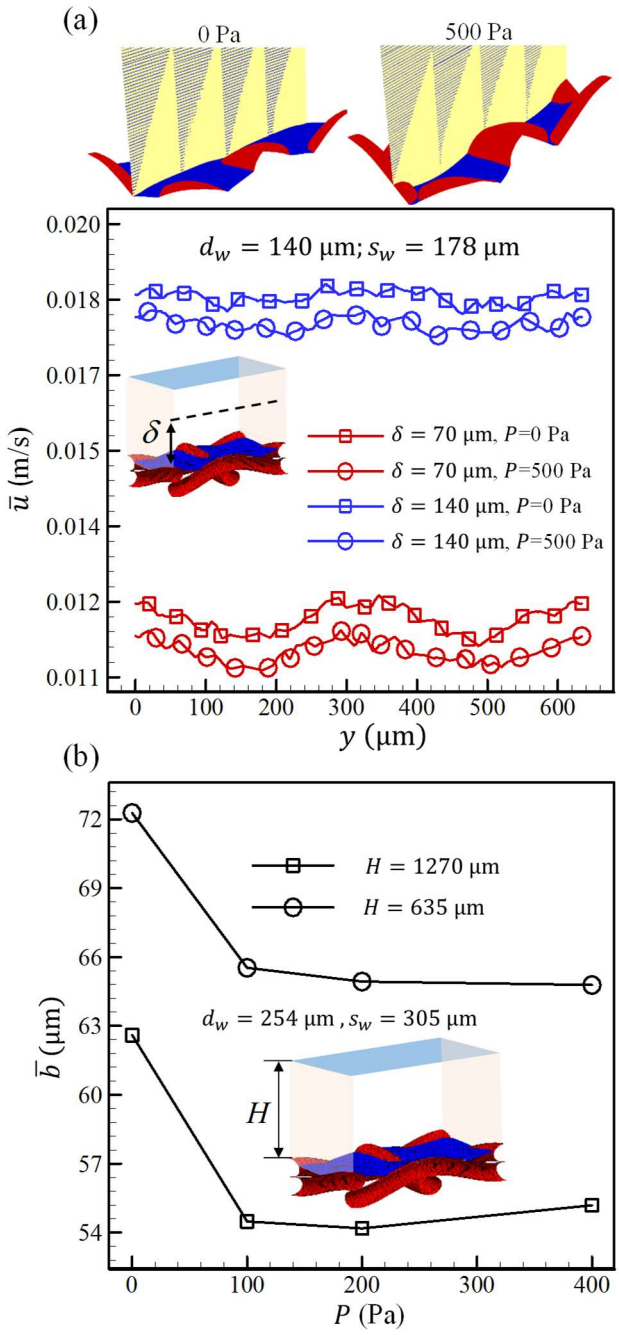

Fig 3.10: Average velocity at a distance δ above the solid surface in a plane slicing through the screen is shown for two different hydrostatic pressures of 0 and 500 Pa in (a) along with example velocity profiles. Effects of the gap distance between the upper and lower plate in Couette geometry H on slip length is shown in (b) for two different gap values as a function of pressure.

velocity vectors in a plane slicing through the wire screen (the case with a wire diameter of $d_w = 140$ μm and a wire spacing of $s_w = 178$ μm) are shown in Fig. 3.10a and their average values at a distance δ above the surface are calculated for operating pressures of 0 and 500 Pa (see the dashed line in the inset figure). It can be seen that, average velocity above the surface is almost independent of operating pressure, even when the AWI penetrates deeper into the screen when the pressure is higher. This means despite the increase in the wetted area of the screens under pressure, no measurable additional friction is generated against the flow. This observation is also consistent with the results reported in [94].

The results given in Figs. 3.9b and 3.9d indicate that slip length decreases continuously with pressure when predicted using the approximate formula given in Eq. 3.6 (even reaching negative slip length values). However, this equation seems to provide reasonable predictions at relatively low pressures, and more importantly, it does not require solving the Navier–Stokes equation. Figure 3.9b shows that, at a given operating pressure, effective slip length is higher for wire screens with larger wire spacing. This is mostly due to the fact that wetted area fraction is smaller for such screens (see Fig. 3.9a). On the contrary, Fig. 3.9d shows that, at a given pressure, effective slip length over wire screens with identical wire spacing is higher for screens with larger wire diameters. This is in contradiction with the wetted area fraction results shown in Fig. 3.9b. However, it should be noted that the results shown in Fig. 3.9d were obtained for a fixed gap of $H = 1000$ μm between the upper and lower plates. Therefore, the effective gap (distance between the top surface of the wires and the moving upper wall) decreases with increasing the wire diameter, and this makes the screen with a larger wire diameter produce more slip length despite having a larger wetted area fraction.

To further investigate this, effective slip length over a screen with a wire diameter of $d_w = 254$ μm and a wire spacing of $s_w = 305$ μm is calculated for two different gap distances of $H = 1270$ μm and

$H = 635$ μm in Fig. 3.10b. It can be seen that slip length increases by about 20% when the gap is decreased by a factor of 2. This is in qualitative agreement with the observation reported in [95].

3.4 Conclusions

Woven screens enhanced with functional surface treatments/coatings have recently be considered as a cost-effective alternative for producing a SHP porous surface in many applications including but not limited to drag reduction [3,23,79-80], oil–water separation [4,26,81-83], self-cleaning and anti-icing [5-6,84], and device manufacturing [87-91] among many others. In this work, we reported on the failure pressure of such screens and discuss how the interplay between the wire diameter and wire-to-wire spacing can affect the performance of a SHP screen. An approach for obtaining an accurate estimate of a screen's wetted area in 3-D is presented and is used to calculate its drag reduction benefit (slip length) when the screen is used in a Couette flow configuration. Our simulations indicate that operating pressure in the Couette configuration does not significantly affect the drag reducing effects of the screens. Different formulations proposed in the literature for predicting the slip length of a SHP surface are compared with one another and their pros and cons are discussed in detail.

Chapter 4. Modelling Droplet Sliding Angle on Hydrophobic Wire Screens

4.1 Introduction

Wire screens treated with a hydrophobic coating have become a cost-effective way of creating a porous water repellent (or oil repellent if treated with an oleophobic coating) surface. Such porous structures have been considered for a variety of potential applications such as drag reduction on submerged surfaces [3,23,88,89,96], oil–water separation [4,91-92,97-99], heat transfer or anti-icing [6-8,97], self-cleaning [27,105-106], and fog harvesting [7,100-101] to name a few. The main attribute of a hydrophobic surface is the ability to reduce the area of contact between the solid surface and a body of water (often referred to as surface wetted area). While a reduced wetted area (WA) is the primary cause for achieving drag reduction in the case of a submerged hydrophobic surface [2,80,83,85], the problem becomes unfortunately more complicated when it comes to droplet mobility on the surface (e.g., in separating dispersed water droplets from diesel or oil droplets from engine exhaust). The complexity in predicting the degree of droplet mobility over a hydrophobic surface arises mainly from the fact that it depends on the WA of the solid surface, the length of the three-phase air–water–solid contact line (CL), the 3-D shape and orientation of WA and CL with respect to the direction of the droplet's motion, and the slope of the air–water interface (AWI) along the CL. Obviously, these factors depend strongly on both the surface morphology and on the physical properties of the droplet. An additional factor further complicating this problem is the tendency of the droplet to pin itself to certain local sites on the surface (caused perhaps by chemical or morphological non-homogeneities). These factors make it almost impossible to accurately predict the degree of droplet mobility over a hydrophobic surface via a first-principles theoretical approach. In the absence of a better option, droplet mobility over

a hydrophobic surface has often been characterized empirically in terms of the droplet's advancing and receding contact angles (CAs) which are the CAs in the direction of droplet motion (most probably the largest and smallest CAs along the perimeter of the droplet) on that specific surface. One should keep in mind that there is nothing fundamentally important about the advancing and receding CAs other than they are easy to measure via imaging. In fact, the advancing and receding CAs are only two "dependent variables" that owe their values to a series of morphological (surface) and thermodynamic (droplet) "independent variables", and therefore their applicability is limited to the specific surface and droplet size used in measuring them. Because of these inherent limitations, the force required to detach a droplet from a surface is often presented in terms of the difference between the advancing and receding CAs (i.e., CA hysteresis) but multiplied by an empirical factor to compensate for the lack of sufficient information about the impact of the actual "independent variables" in this problem [5,102-110].

In the absence of pinning effects (e.g., the case of a surface with round asperities like those of a wire screen), a theoretical approach can be considered to predict the force of detachment (and of course the advancing and receding CAs) as was discussed in our previous work for droplet detachment from a single fiber [111-112]. In the current paper, we study the effects a screen's geometrical parameters on the mobility of droplets of different sizes on its surface via numerical simulation, for the first time. Complimentary experiments have also been conducted for model validation whenever possible. Furthermore, the direct application of the current work is to establish the dependency of wettability and hydrophobicity on the screen parameters, to increase the efficiency of the woven screens for direct applications like fog harvesting, mesh membranes to separate immiscible oil/water mixtures.

Remainder of this chapter is organized as follows. We first present a condensed review of the common knowledge regarding droplet CAs on flat and tilted surfaces in Sec. 4.2. We then discuss our numerical approach for modelling droplet over hydrophobic wire screens in Sec. 4.3 and our experimental approach in Sect. 4.4. Our results and discussion are given Sec. 4.5, followed by our conclusions in Sec. 4.6.

4.2 Advancing and Receding Contact Angles On Hydrophobic Wire Screens

On a rough surface the droplet exhibits multiple equilibrium states and apparent contact angles. The apparent CA θ_{app} (average local CA), for a droplet associated with the global free energy minimum on an isotropic hydrophobic surface is given by [113-115].

$$cos\theta_{app} = r_f f cos\theta_{YL} + f - 1 \tag{4.1}$$

In this equation r_f is the ratio of the WA to its projected area on a horizontal plane, and f is the ratio of the same projected WA to the total projected contact area of the droplet with the surface. θ_{YL} is the Young–Laplace contact angle (YLCA) of a chemically identical smooth surface (see Fig. 4.1b). Treating the wire texture of a monofilament textile as an array of parallel cylinders, Eq. 4.1 was modified in [27] to predict the apparent CA of droplets on woven fabrics, i.e.,

$$cos\theta_{app} = \frac{1}{D^*}(\pi - \theta_{YL})cos\theta_{YL} + \frac{1}{D^*}sin\theta_{YL} - 1 \tag{4.2}$$

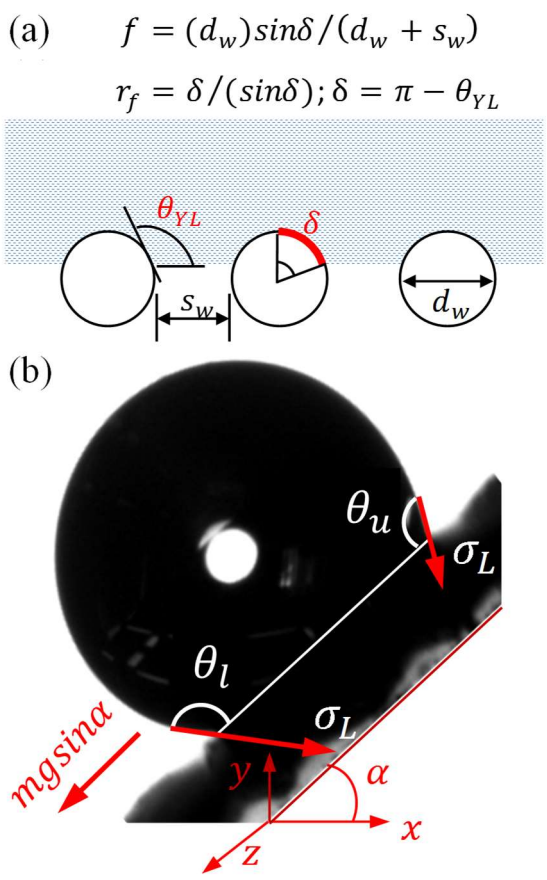

Fig 4.1: (a) illustration of a flat AWI over an array of parallel cylinders with a diameter d_w and separated by a distance s_w. The parameters f and r_f from Eq. 4.1 are also shown graphically; (b) lower and upper contact angles are shown for a droplet deposited on a tilted screen.

where $D^* = (d_w + s_w)/d_w$, and d_w and s_w are the filament (wire) diameter and the filament-to-filament spacing, respectively. There are contradictory reports with regards to the accuracy of Eqs. 4.1 and 4.2 for apparent CA prediction on wire screens (while studies such as those in [106,116-117] showed good agreement between experimental data and predictions of Eqs. 4.1 and 4.2, the work of [100,118] report to the contrary). It is important to note that these equations were derived assuming that *i*) droplet size is larger than the scale of surface roughness, *ii*) the surface is isotropic surface, and *iii*) the AWI is flat. More specifically, Eq. 4.1 is not derived for when the AWI penetrates into the pores of the surface as discussed in [119]. For instance, apparent CA is expected

to increase monotonically by increasing the spacing between the filaments according to Eq. 4.1. This however, is not generally true for a wire screen with a wire spacing comparable to the size of the droplet, as will be seen later in this paper.

Sliding angle is a simple way of characterizing droplet mobility on a surface. Droplet mobility requires low adhesion force between the liquid and the solid, such that the droplet can easily slide off the surface at small inclination angles. When a hydrophobic surface is tilted, the droplet starts to deform due to gravitational forces leading to the formation of lower and upper CAs, denoted in Fig. 4.1c by θ_l and θ_u, respectively. More specifically, a droplet on an inclined surface experiences a body-force given by

$$F_G = mgsin\alpha \tag{4.3}$$

where m is the mass of the droplet, g is the gravitational acceleration, and α is the inclination angle. This force is generally balanced by the adhesion force between the droplet and the rough solid surface. Increasing the inclination angle generally results in an increase in the lower CA and a simultaneous decrease in the receding CA. In a pioneering study [120], it was suggested that droplet adhesion force is proportional to the surface tension of the liquid γ_{LV}, the width of contact area w_d (perpendicular to droplet's direction of motion), and the difference between the cosines of lower and upper CAs at the sliding angle i.e.,

$$F_A = k\gamma_{WA}w_d(cos\theta_{min} - cos\theta_{max}) \tag{4.4}$$

where is k is an empirical correction factor that accounts for all the factors neglected in developing this equation (reported for instance, to vary in the range of 1 to 3.14 in [105]) and $\theta_{min} = \theta_l$,

$\theta_{max} = \theta_u$ are the contact angles at at the sliding angle α. The lower θ_l and upper θ_u CAs can be different from the droplet's advancing and receding angles. [121]

Equation 4.4 is generally valid for a droplet on a smooth flat surface, and as was mentioned earlier, additional factors (e.g., shape and location of the CL, WA, Laplace pressure, AWI penetration into surface pores…) should be taken into consideration for surfaces with added or inherent roughness [5]. For instance, increasing the inclination angle decreases the gravitational force pushing the droplet onto the surface. This in turn, changes the shape and location of the CL (among other parameters) when the surface is rough (e.g., a wire screen).

4.3 Modelling Droplet Shape on Hydrophobic Wire Screens

In this paper, the effects of the geometrical parameters of a wire screen (e.g., wire diameter d_w and wire spacing s_w) on droplet CAs and mobility are studied computationally and compared with experiments (Sec. 4.4). The energy minimization method implemented in the Surface Evolver (SE) finite element code is used here to simulate the 3-D shape of water droplets with different volumes on wire screens with different geometries. For a droplet sitting on a surface, the free energy of the system can be expressed as [122-123],

$$E_T = \gamma_{WA} A_{WA} + \gamma_{WA} cos\theta_E \iint_{A_{SW}} dA + \iiint \rho g z dV \qquad (4.5)$$

where γ_{WA} is the water–air surface tension, and A_{WA} and A_{SW} are the water–air and solid–water interfacial area. Assuming screens' wires to be circular with a sinusoidal centerline profile oriented in the *x* and y directions (referred to here as warp and weft respectively). The warp and weft in a wire screen with an inclination angle of α about the y-axis can mathematically be presented respectively as (see Fig. 4.2),

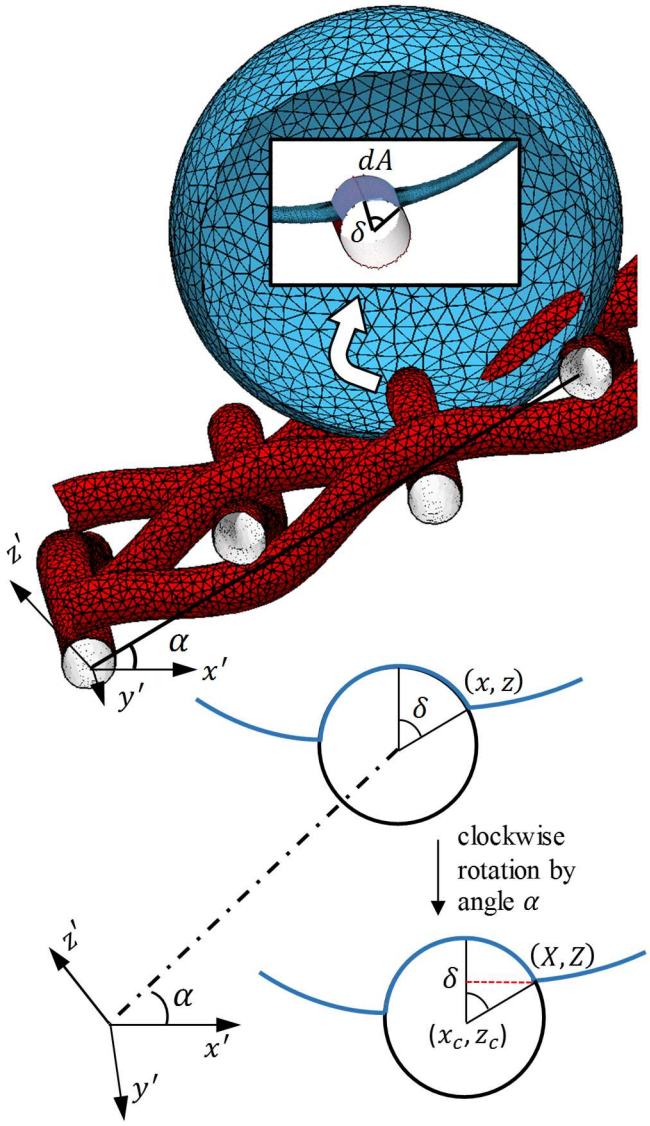

$$X = xcos\alpha + zsin\alpha; \quad Z = -xsin\alpha + zcos\alpha;$$

$$z_c = \frac{d_w}{2}\left(sin\left(\frac{\pi}{l}y + \varphi\right) + 1\right); \ \delta = \tan^{-1}\left(\frac{X - x_c}{Z - z_c}\right);$$

Fig 4.2: Sliced view of a droplet on a wire screen showing the solid–liquid wetted area and the interface immersion angle. Parameters used in Eq. 4.8 are shown using a 2-D representation of the air–water interface in contact with a wire.

$$\left((-xsin\alpha + zcos\alpha) - \frac{d_w}{2}\left(si \quad \frac{\pi}{l}x + \varphi\right) - 1)\right)^2 + (y - y_c)^2 = \left(\frac{d_w}{2}\right)^2 \tag{4.6}$$

$$\left((-xsin\alpha + zcos\alpha) - \frac{d_w}{2}\left(sin\left(\frac{\pi}{l}y + \varphi\right) - 1\right)\right)^2 + (xcos\alpha + ysin\alpha - \ _c)^2 = \left(\frac{d_w}{2}\right)^2 \tag{4.7}$$

where φ is the phase shift (in radian), and y_c and x_c are the x and y coordinates of the wires, respectively. SE considers the interfacial energy of the droplet in the total energy of the system, but the wetting energy of the wires needs to be defined for SE and added to the second term on the right side of Eq. 4.5. This is accomplished here by defining the area element dA in Eq. 4.5 as

$$dA = d_w \delta \sqrt{1 + [z_c']^2}\, dy \tag{4.8}$$

where $z_c = \frac{d_w}{2}\left[sin\left(\frac{\pi}{2}y + \varphi\right) - 1\right]$ is the z-coordinate of the wire centerline. In this equation, δ is the wetting angle (see Fig. 4.2) and it is a function of z_c,

$$\delta = \tan^{-1}\left(\frac{xcos\alpha + ysin\alpha \quad _c}{(-xsin\alpha + zcos\alpha) - \frac{d_w}{2}\left(sin\left(\frac{\pi}{l}y + \varphi\right) - 1\right)}\right) \tag{4.9}$$

Upon defining the initial surface in a data file, SE evolves the droplet shape by meshing the surfaces involved in the calculations and iteratively moving the vertices of the meshed AWI to reach a minimum (local or global) energy value for the whole system under a constant droplet-volume constraint. In this paper, we define the sling angle α as, the largest inclination angle at which the droplet can have a stable shape without moving on the surface. Numeircaly, this happens when SE cannot converge to a stable equilibrium shape upon increasing the inclination angle. For the boundary conditions, the AWI at the CL is assumed to conform to a slope that matches the droplet's YLCA.

4.4 Experiment

To confirm the results of our numerical simulations, the droplet sliding angle was measured on wire screens (from McMaster-Carr) spray-coated with a water repellent solution, Ultra-Ever Dry

(from Ultratech Company). The screens were cut into 1 inch by 1 inch squares and inspected to be perfectly flat during the

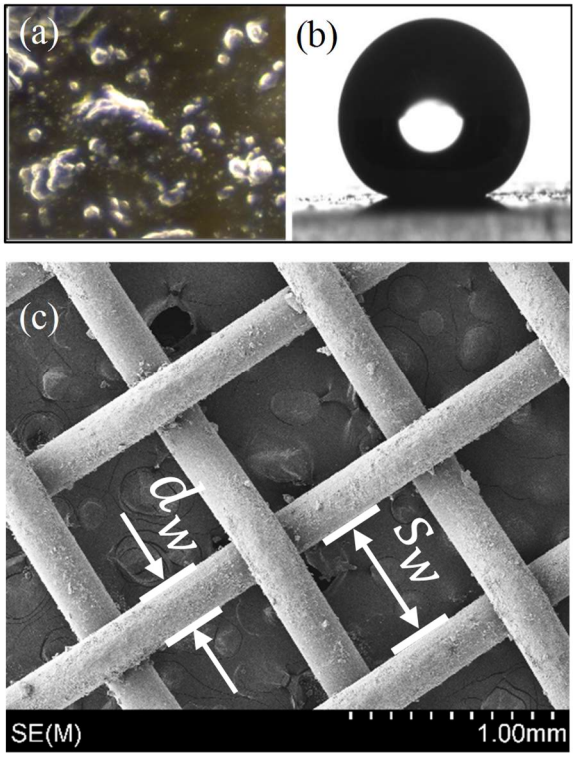

Fig 4.3: (a) A microscope image of a glass slide coated with Ultra-Ever Dry, (b) a droplet image on the coated glass slide showing an YLCA of $\theta_{YL} = 120^{\circ}$; (c) an SEM image of one of the spray-coated wire screens used in this work.

experiment. The screens were prepared by first spraying an adhesive coating (bottom coating) on them. The screens were allowed to dry in ambient atmosphere for about 45 minutes before the hydrophobic coating (top coating) was applied. The coating was sprayed in a fine mist and as consistent as possible to maximize its uniformity on each screen. Multiple screens were used for each size to obtain statistically meaningful measurements. Occasionally, a film of hydrophobic coating would form across one or numerous pores of the screen, however, these screens were discarded to avoid inconsistencies. The YLCA of the coating was obtained by employing 5 µL droplets on a microscope slide (coated in a similar manner) at three different locations and the

average was found to be 120 degrees (see Fig. 4.3). The coated screens were placed on a goniometer consisting of a CCD camera, a syringe pump, and a tilting platform. Water droplets of known volume were placed on the screens (in horizontal position) using a sharp-needle micrometer syringe and tilted incrementally (3-degree increments). The droplets were observed to continuously deform as the platform was tilted, until they eventually slide off the screen at a maximum inclination angle referred to here as the sliding angle. The droplets were imaged during the experiment and the images were used to extract droplet's lower and upper CAs. Each experiment was repeated at least three times to produce average values and a standard deviation for each case. Each experiment was completed in less than 5 min to minimize the errors associated with droplet evaporation.

4.5 Results and Discussion

In this section, we first discuss the effects of wire diameter and spacing on apparent CAs for droplets with different volumes. We then discuss the droplets' lower and upper CAs followed by a discussion about the effect of screen dimensions on the droplet sliding angle. We will compare the results of numerical simulations with those obtained from our experiments whenever possible.

4.5.1 Apparent Contact Angle

Figure 4.4 shows a droplet with a volume of 30 μL on a coated wire screen with $d_w = 254$ μm and $s_w = 660$ μm from side (Fig. 4.4a) and top (Fig. 4.4c) views along with its numerical counterparts (Figs. 4.4b and 4.4d) simulated using the procedure described in Sec. 4.3. The local CA is found to be 135° for the imaged droplet and 138° for the simulated one. The local CA θ_A, is

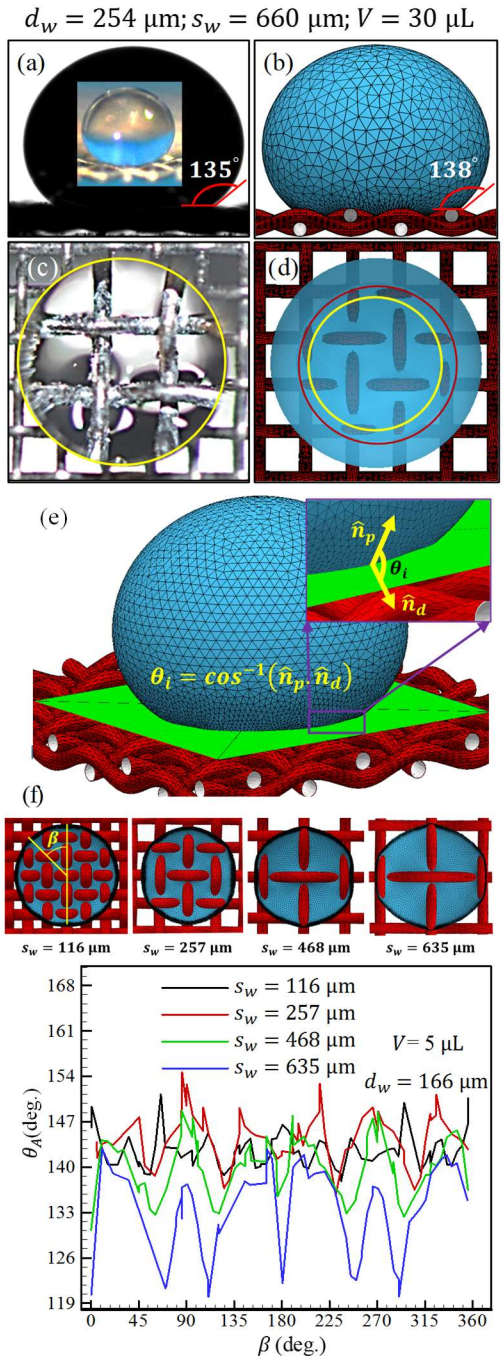

Fig 4.4: Side (a and b) and top (c and d) views of a droplet with a volume of $V = 30$ µL on a screen with $d_w = 254$ µm, $s_w = 660$ µm, and $\theta_{YL} = 120^{\circ}$ obtained from experiment (left) and simulation (right). (e) Local contact angle $\theta_A = \pi - \theta_l$ is shown using the normal to the droplet surface at contact line $\hat{n}_p$ and the normal to a horizontal plane placed at the top surface of the wires $\hat{n}_d$.(f) Apparent contact angle along the azimuthal angle β is shown for a droplet with a volume of $V = 5$ µL on screens with a wire diameter of $d_w = 166$ µm and an YLCA of $\theta_{YL} = 120^{\circ}$but different spacing values.

determined using the dot-product of the unit normal $\hat{n}_d$ to a plane tangent to the droplet (to the facets of the meshed droplet) and the unit normal $\hat{n}_p$ to a reference horizontal plane in contact with the top surface of the wires (see Fig. 4.4e $\theta_A = \pi - cos^{-1}(\hat{n}_p.\hat{n}_d)$). It is important to note that, a droplet deposited on a wire screen can have different local CAs from different viewpoints due to macroscopic roughness of the surface. For this reason in this work, local CAs viewed from different directions are computed and averaged for each case to obtain apparent CA which can be written as

$$\theta_{app} = \frac{\oint_C \theta_A dl}{\oint_C dl} \tag{4.10}$$

where C indicates the closed integration path along the three phase contact line. The simulated droplet is shown in blue color and its contact with the wires is highlighted with a red circle for better illustration in (Fig. 4.4d). The wetted surface area of the wires under the droplet can be seen as red-color islands in the blue-color background of the droplet interface with air. A similar pattern can be seen in the imaged droplet, but as the droplet magnifies the objects under it, Fig. 4.4c shows only the central part of the area under the droplet (highlighted by a yellow circle in Figs. 4.4c and 4.4d for better illustration).

Figure 4.4f shows the local apparent CA as a function of the azimuthal angle β for a water droplet with a volume of 5 µL on a wire screen with a wire diameter of $d_w = 166$ µm but four different wire spacing values. The area of contact between the droplet and screens is also shown in this figure. It can be seen that screen's WA increases by decreasing the spacing between the wires (everything else being constant). It can also be seen that a droplet imprint on the screens becomes less circular as the spacing is increased leading to a larger variation in the apparent CA around the perimeter of the droplet.

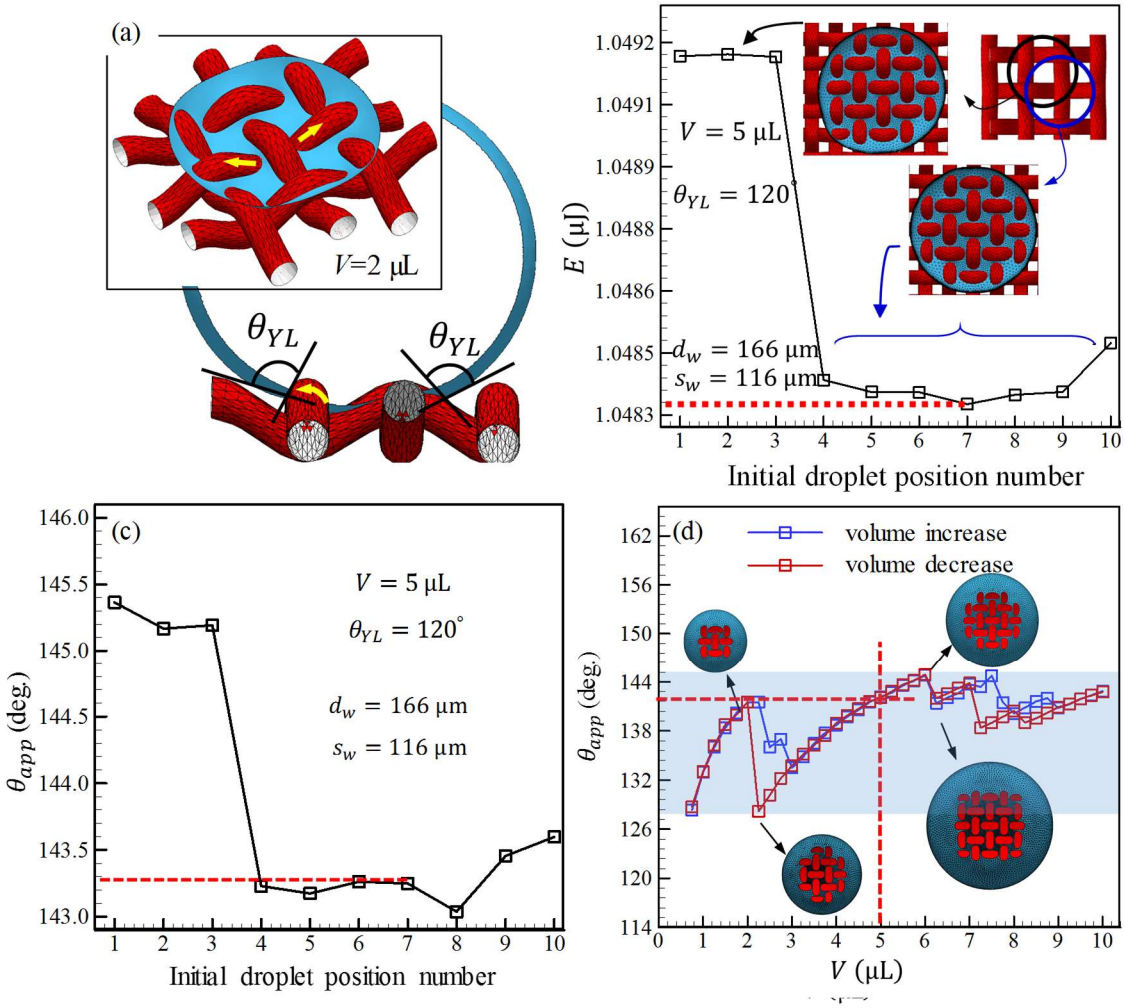

Fig 4.5: (a) A stable position for a droplet on a wire screen. Examples of the regions where the droplet contact line cannot reside are shown with yellow arrows. **(b)** Global droplet energy and apparent contact angle obtained from simulations with different initial positions on screens with a diameter of $d_w = 166$ μm and spacing of $s_w = 113$ μm with droplet volumes of $V = 5$ μL. (c) The apparent contact angle using Eq. 4.10 from the simulations for the same parameter as in (b). (d) Effect of droplet volume on the apparent contact angle for the screen in (b) for both volume-increase (blue) simulations and volume-decrease (red) simulations.

It is interesting to note that satisfying the YLCA at the CL prevents the droplet from reaching an equilibrium position on certain parts of the surface (where the slope of the warp or weft cannot accommodate an AWI slope corresponding to the YLCA). Figure 4.5a shows the equilibrium profile of a droplet with a volume of 5 μL on a wire screen with $d_w = 254$ μm, $s_w = 313$ μm,

and $\theta_{YL} = 120$ deg. Note the slope of the AWI on the warp and weft matching the YLCA. The yellow arrows in Fig. 4.5a show examples of the areas where a CL cannot reside at equilibrium.

When a droplet is placed on the real rough surface, it may exhibit multiple equilibrium energy states and a range of apparent contact angles. To further investigate the equilibrium states of the system in Fig. 4.5b, the droplet shape and the total energy of the system is presented for different initial droplet positions with a volume of 5 μL on a wire screen with $d_w = 166$ μm, $s_w = 116$ μm, and $\theta_{YL} = 120$ deg. This is performed for nine different initial droplet positions in the neighborhood of the position shown with a black circle (when the droplet center of mass is lined up with the center of the screen's unit cell) [124]. The blue circle in Fig. 4.5b shows an example of these nine initial positions (numbered 2 to 10 with no special order on the horizontal axis in Fig. 4.5b). Our simulations revealed that the droplet which was initially placed in the vicinity of the middle of the screen's unit cell, reached a final equilibrium shape with maximum total energy, while the droplets placed in the six other positions reached an identical final equilibrium shape with lower total energy (shown in red color horizontal line). Figure 4.5c shows the apparent contact angle, averaged using Eq. 4.10, for the droplets simulated in Fig. 4.5b. The most stable apparent contact angle is the one associated with the minimum total energy of the system $\theta_{app} = 143.25^{\circ}$ (shown with red horizontal line in Figs. 4.5b and 4.5c). Close attention was paid to ensure that droplet apparent CAs reported in this work are those corresponding to a minimum global system energy.

The multiplicity of the minimum total energy of the droplet-screen system depends on the drop volume and the screen dimensions. The range of observable apparent CAs is known as contact angle hysteresis (CAH). To better illustrate this, a droplet was placed on the same screen, and the

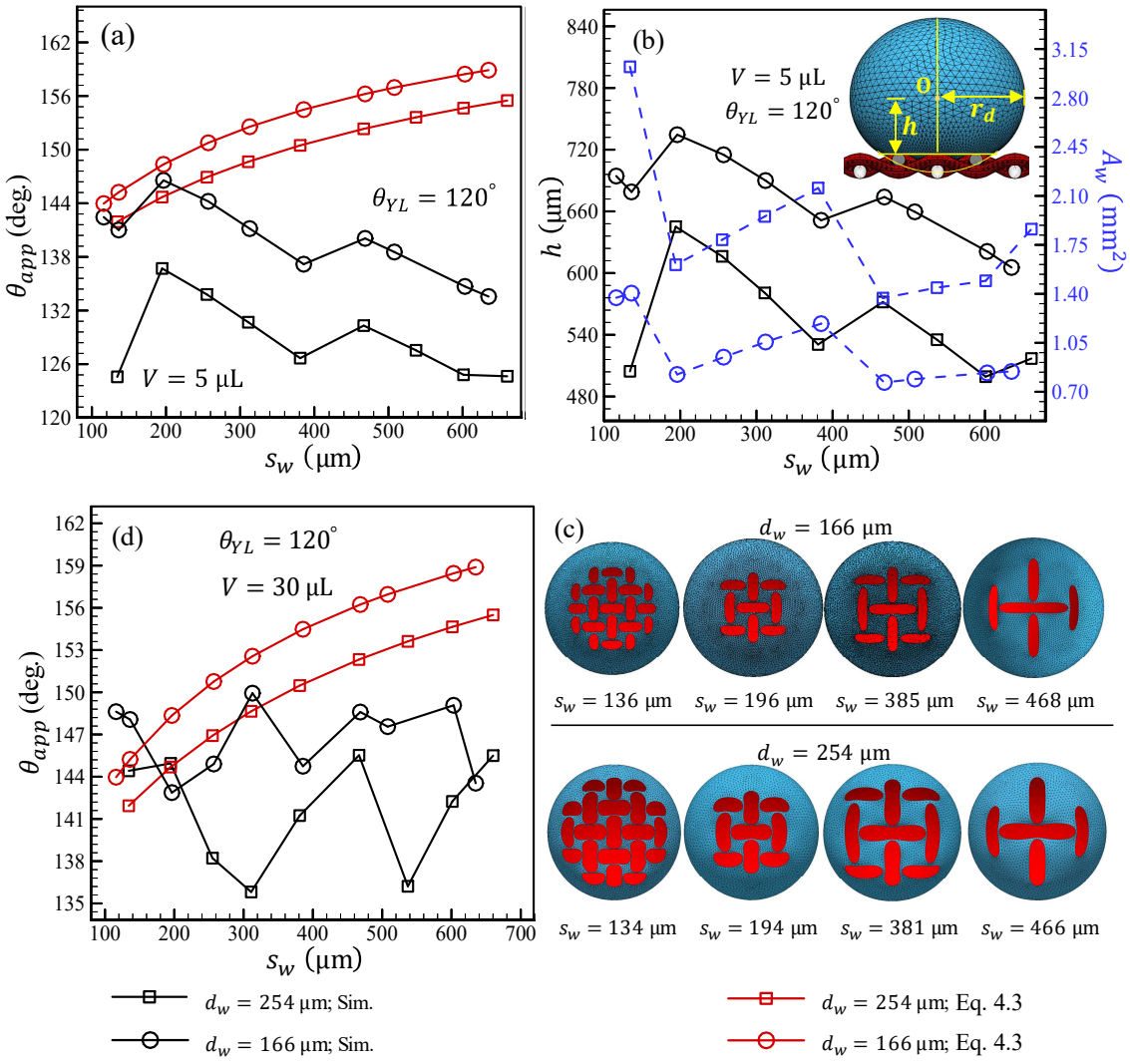

Fig 4.6: (a) Effects of wire spacing s_w on apparent contact angle θ_{app}, distance between droplet center and screen top surface h , and wetted area A_w for droplets with a volume of 5 µL are shown in (a) and (b). Simulation data, and predictions of Eq. 4.2 are shown in black and in red, respectively. Droplet contact area with screens having different wire diameters and spacing are shown in (c). Effects of wire spacing s_w on apparent contact angle θ_{app} is shown in (d) for a droplet with a volume of $V = 30$ µL.

droplet volume was continuously varied from 0.75 µL to 10 µL and vice versa. It can be seen that as the droplet volume increases, the apparent CA increases reaching an advancing CA of $\theta_{adv} = 144^{\circ}$. The droplet apparent CA suddenly decreases, due to change in the radius of droplet's footprint (the so-called stick-slip phenomena [124]. Similarly, with decreasing droplet volume, the

apparent CA decreases until it reaches a receding CA of $\theta_{rec} = 128^{\circ}$. The CAH, the difference between the advancing and receding CAs is highlighted with a blue shadow in Figure 4.5d. Note also that the amplitude of CA fluctuations decreases with increase droplet volume. The most stable apparent CA can be estimated by taking the average of the advancing and receding CAs over the entire range of droplet volumes (136.5 deg.), or it can be approximated by considering the CA associated with lowest global minimum energy of the system (143 deg.) [125]. The latter has been considered in our study, but the former approach is also shown for comparison in Figure 4.5d.

In order to study the effect of screen's parameters (spacing and diameter of wire), it is difficult to simulate a range of volumes and measure the CAH for different screens. Therefore, we report the apparent CA's of the droplets from here onwards considering minimum energy approach as discussed in Figure 4.5b and 4.5c. Figure 6a shows the effects of wire spacing on the apparent CA defined by Eq. (4.10) for a droplet with a volume of 5 µL on screens having two different wire diameters of $d_w = 166$ µm and $d_w = 254$ µm. This figure compares the results of metastable apparent contact angle numerical simulation associated with the minimum energy (black lines and symbols) with the predictions of Eq. 4.3 (which is also for most stable CA) . It can be seen that numerical data show a fluctuating but somewhat downward trend in clear contrast to the predictions of Eq. 4.2. We believe this discrepancy is due to the fact that Eq. 4.2 doesn't account for the penetration of the AWI into the pore space between the wires (see [96] for more information about AWI over hydrophobic wire screens). In other words, Eq. 4.2 is only accurate when the AWI remains close to the top surface of the wires, i.e., when the droplet radius is much larger than the spacing and diameter of the wires [126]. Similar disagreement between the predictions of Eq. 4.2 and the numerical/experimental data has also been reported by [127-129]. To better characterize this, we report the distance between the center of an imaginary sphere matching the body of the

actual droplet (referred to as O in Fig. 4.6b) and the top surface of the wires (referred to as h). As can be seen in Fig. 4.6b, h decreases with increasing the spacing between the wires (this information will also be used later in this paper when discussing droplet sliding angle). Figure 4.6b also shows the effects of increasing wire spacing on screens' WA denoted by A_w. It can be seen that the WA decreases with spacing, but not monotonically, as illustrated in Fig. 4.6c (top row) for the wire screens with $d_w = 166$ μm. Comparing the variations of A_w in Fig. 4.6b with that of apparent CA in Fig. 4.6a, one can see an inverse relationship between the apparent CA and WA, but the relationship tends to fade at higher spacing (note that the matching trends of apparent CA and h is trivial as they are geometrically related). It is also interesting to note that for screens with identical wire spacing, apparent CA is always higher for the screen with a smaller wire diameter (see Fig. 4.6a) which can be due to the increase of the WA with increasing wire diameter as can be seen in Fig. 4.6c (bottom row). To also study the effects of droplet size we repeated our simulations for a droplet with a volume of $V = 30$ μL and reported the apparent CA values in Fig. 4.6d. It can be seen that the apparent CA is slightly higher for this larger droplet. This can be due to lower Laplace pressure of the bigger droplet, resulting in less penetration of the AWI into the screen (the droplet can better retain its special shape and exhibit a higher apparent CA). This analysis is obviously invalid for larger droplets where the gravitational effects are not negligible.

4.5.2 Sliding Angle

Figures 4.7a and 4.7b report lower and upper CAs obtained for a droplet with a volume of $V = 5$ μL on a screen with $d_w = 254$ μm, $s_w = 381$ μm, and $\theta_{YL} = 120^{\circ}$ from simulation and experiment. Numerical simulations started with a droplet placed on a screen held at the desired inclination angle. The experimental data, on the other hand, were obtained by first placing the

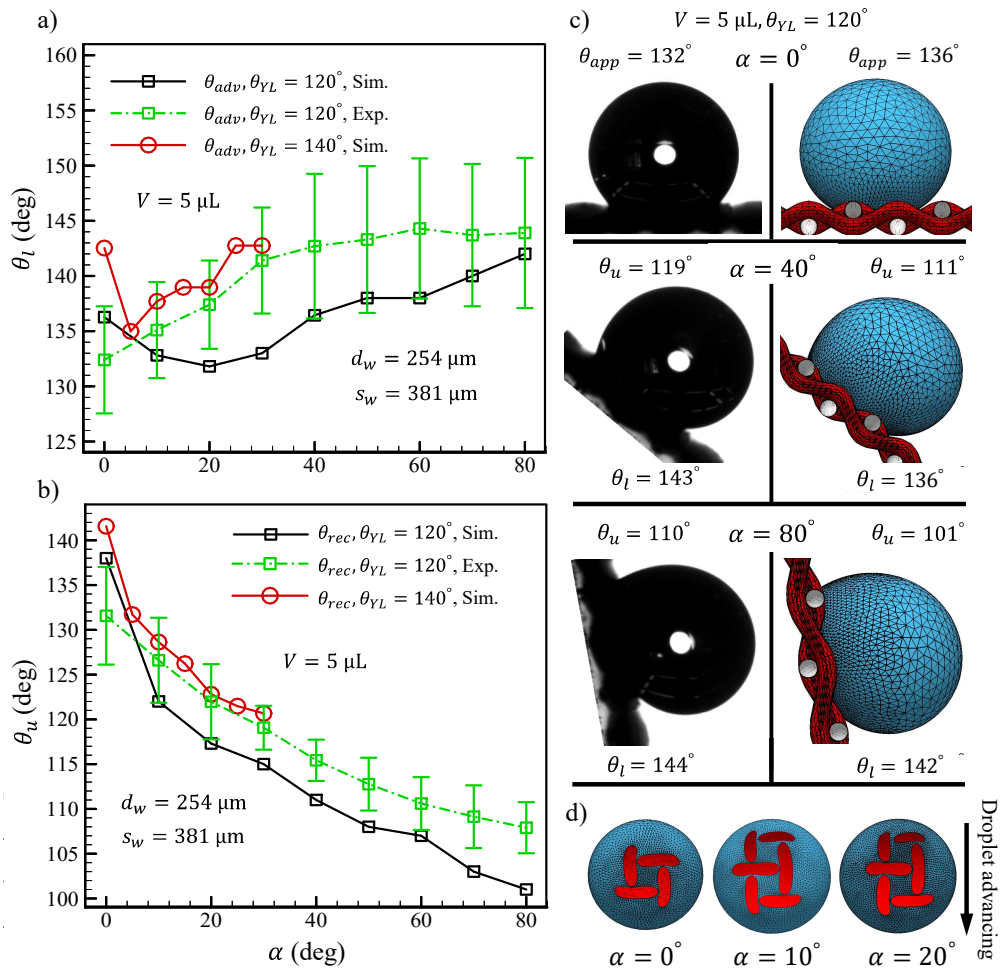

Fig 4.7: Effects of tilt angle α on lower and upper contact angles for a droplet with a volume of $V = 5$ µL on a screen with $d_w = 254$ µm, $s_w = 381$ µm but two different YLCAs of 120 and 140 degrees are shown in (a) and (b), respectively. Comparison between droplet contact angles from experiment (left) and simulation (right) for three different tilt angles of 0, 40, and 80 degrees are given in (c). Droplet contact with wire a screen is given for three different tilt angles of 0, 10, and 20 degrees. Droplet volume and screen dimensions are the same as those in (a) with an YLCA of 120 degrees.

droplet on the screen in a horizontal position, and then tilting the screen. This was considered to reduce the impact of droplet's inertia (at the moment of deposition) on the results. As can be seen in Figs. 4.7a and 4.7b, experimental and numerical data are in good general agreement (about 8% and 5% mismatch in lower CAs and upper CAs, respectively). As expected, lower CA increases and upper CA decreases with increasing the inclination angle until the droplet slides off the surface.

To also study the effects of YLCA on lower and upper CAs, we repeated our simulations with an YLCA of 140 degrees and added the results to Figs. 4.7a and 4.7b. It can be seen that both the lower and upper CAs increase with increasing the YLCA. While the simulation results with $\theta_{YL} = 140^{\circ}$ appear to be closer to the experimental data, we believe this is coincidental as the simulated droplet with $\theta_{YL} = 140^{\circ}$ slides off the screen surface at an inclination angle of about $\alpha = 30^{\circ}$ while the actual droplet sticks to the surface, same as the simulated droplet with $\theta_{YL} = 120^{\circ}$. Figure 4.7c compares the droplet shape obtained from numerical simulations with that from the experiment for a droplet volume of $V = 5$ µL on a screen with $d_w = 254$ µm and $s_w = 384$ µm at three different inclination angles of $\alpha = 0^{\circ}, 40^{\circ}$ and 80° (lower and upper CAs are given in the figure for each case). Good general agreement can again be seen between the experimental and computational results both in terms of droplet shape and droplet lower or upper CAs.

It is important to mention that the computational lower CAs reported in Fig. 4.7a show an initial decrease with increasing the inclination angle from 0 to 20 degrees, which appears to be inconsistent with the trend of data obtained from experiment. To better explore this, we reported the WA of the screen for three different inclination angles of 0, 10, and 20 degrees in Fig. 4.7d. It can be seen that the droplet initially wets a relatively small area of the screen at an inclination angle of zero (resulting in a larger CA) but it reshapes and wets a larger area upon a slight increase in the inclination angle. This happens instantly in the experiment during the process of depositing the droplet, as it is almost impossible to place a droplet on the screen with zero inertia. In other words, the droplet wets more than one unit cell even at an inclination angle of zero due to experimental error. This can also be seen in the CA values where the experimental CA at zero-

degree inclination is smaller than its computational counterpart but it matches the CA at inclination angles of 10–30 degrees.

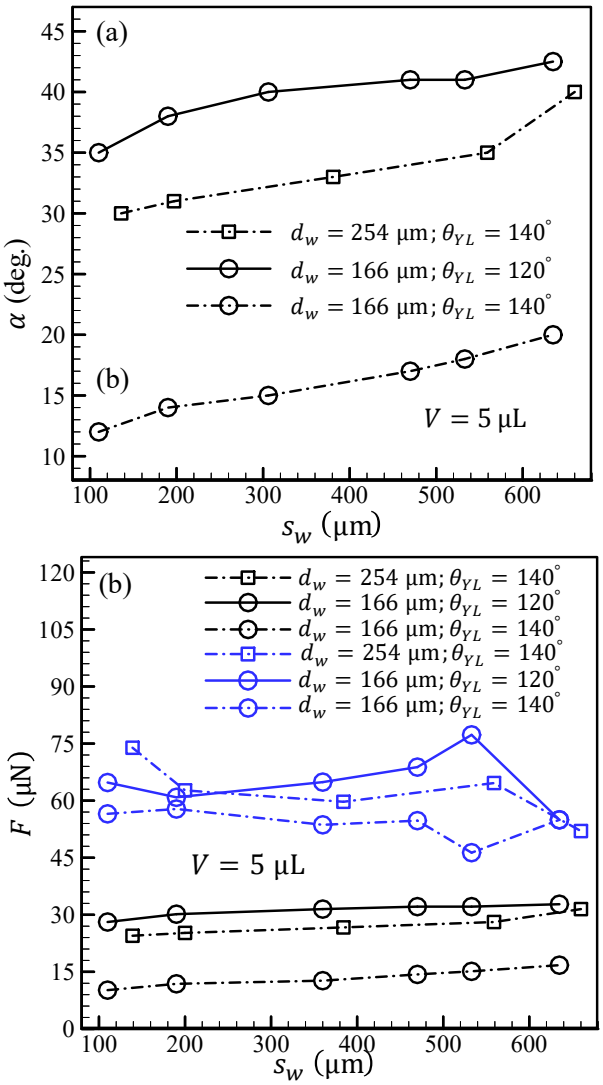

Fig 4.8: (a) Effects of wire spacing on sliding angle for a droplet with $V = 5$ μL on screens with wire diameter and YLCAs. (b) The force calculated using Eq. 4.3 (black color) and Eq. 4.4 (blue color) for the same parameters in (a) at sliding angle α from SE simulations.

The effects of wire spacing on a droplet's sliding angle is shown in Fig. 4.8a for a droplet with a volume of 5 μL on screens with wire diameters of $d_w = 166$ μm and $d_w = 254$ μm and YLCAs of $\theta_{YL} = 120^\circ$ and $\theta_{YL} = 140^\circ$. It can be seen that sliding angle mildly increases with increasing

wire spacing (no sliding was observed even at an indication angle of 90 degrees for the screens with $d_w = 254$ μm and $\theta_{YL} = 120^{\circ}$ for $110 < s_w < 640$; not shown in the figure). The fact that sliding increases with wire spacing may appear counterintuitive as previous studies have reported decreasing sliding angles for increasing spacing between surface asperities (see e.g., [130]). Figure 4.8b shows the force calculated from Eq. 4.3 using the sliding angle from SE simulations and Eq. 4.4 using the θ_{min} ,θ_{max} and w_d (assuming $k = 1$ [131]) from the final equilibrium shapes at the sliding angle from SE simulations. It can be seen that there is discrepancies from the force calculated from Eq. 4.3 and Eq. 4.4. The main reason is as explained before, Eq. 4.3 is the body force (gravitational force) acting on the droplet and Eq. 4.4 is the capillary force acting on the droplet considering the perimeter of the contact line to be circular as the droplet on inclined smooth planar surface. Moreover, when the droplet is on rough surface, the retention force is due to the capillary bridges arising on the receding end of the droplet. This in turn depends on capillary force components acting on the three phase contact line in the direction of the droplet sliding [5].

To better understand the behavior that sliding angle increases with increase in spacing, we track the droplet's footprint on the screens at every inclination angle. This is shown, for a droplet with a volume of 5 μL on a screen with $d_w = 254$ μm in Fig. 4.9a and Fig. 4.9b for wire spacing values of $s_w = 136$ μm and $s_w = 559$ μm, respectively. Comparing these two figures with one another, it can be seen that the droplet on the screen with the smaller wire spacing continuously adjusts its shape and position on the screen in response to increasing the inclination angle up to the point where it can no longer stay on the screen ($\alpha > 30°$). The droplet on the screen with the larger wire spacing on the other hand, shows a less continuous movement on the screen (note the gap between droplet footprints at $\alpha = 10°$ and $\alpha = 15°$ in Fig. 4.9b) and move at a larger inclination angle of

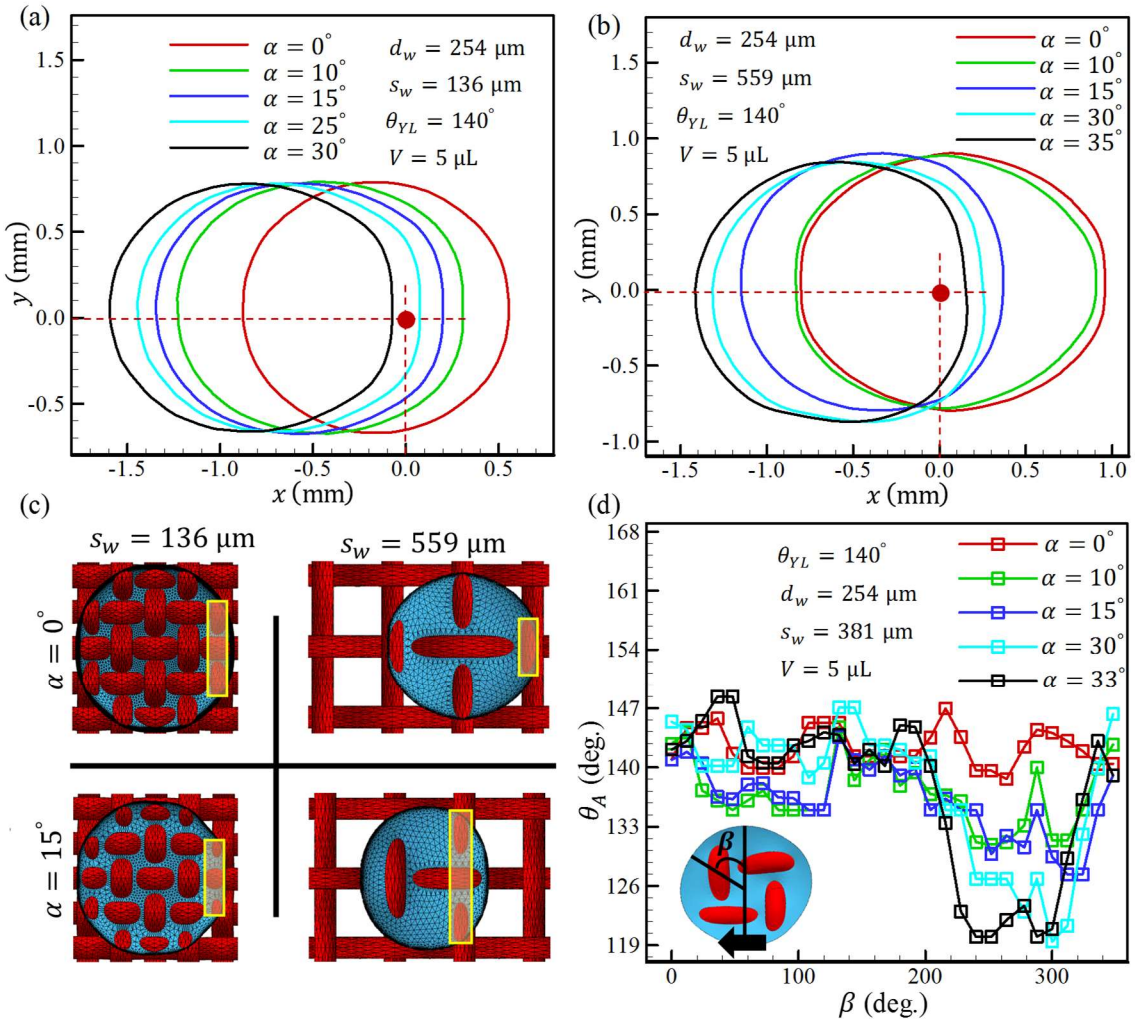

Fig 4.9: Footprint of a droplet with a volume of 5 µL on two screen with identical properties but different wire spacing values of 136 µm and 559 µm are given in (a) and (b), respectively, at different tilt angles. The contact area between the droplet and the screens at tilt angles of 0 and 15 degrees are given in (c). Variations of the local contact angle along the perimeter of the same droplet on a screen with dimension $d_w = 254$ µm, $s_w = 381$ µm, and $\theta_{YL} = 140^{\circ}$is shown in (d).

screen ($\alpha > 35°$). More importantly, droplet footprints in Figs. 4.9a and 9b show that the CL on receding end of the droplet is larger on the screen with the larger wire spacing (see also the yellow-highlighted areas in Fig. 4.9c where AWI is shown at two different inclination angles of zero and 15 degrees on these screens). This means that while the total CL (or WA) is shorter on a screen with a larger wire spacing, the droplet CL on the receding end of the droplet can be longer, and

this contributes significantly to the increase of the sliding angle with increasing wire spacing. This is in agreement with some recent studies where droplet mobility on a hydrophobic surface was observed to depend mostly on the mobility of the receding CL [132]. We believe that the combined effect of longer CL and deeper AWI penetration into the space between the wires (see e.g., [5]) is the main reason for sliding angles increasing with wire spacing in Fig. 4.8. To further quantify this, we report the droplet's CA along its perimeter at different inclination angles on a screen with $d_w = 254$ μm and $s_w = 381$ μm in Fig. 4.9d. It can be seen that with increasing the inclination angle, the CA on the advancing side ($\beta < 180°$) first decreases slightly (droplet moves slightly to wet more wires) but then increases almost continuously. On the receding side ($\beta > 180°$) on the other hand, the CA continuously decreases with increasing the inclination angle. Note that the overall variation in the upper CA is greater than that of the lower CA by a factor of about 2. Furthermore, it can be seen that the local contact angle in the advancing side is not maximum at $\beta = 90^{\circ}$ and at the receding side is not minimum at $\beta = 270^{\circ}$. Due to the macroscopic roughness, the advancing and receding CA doesn't have to be necessarily at the lower side and upper side.

Effects of droplet volume on sliding angle is studied in Fig. 4.10a for screens with a wire diameter of $d_w = 254$ μm having a YLCA of $\theta_{YL} = 120^{\circ}$and two different wire spacing of values of $s_w = 381$ μm and $s_w = 660$ μm. It can be seen that sliding angle increases with decreasing droplet volume (no detachment was observed even at an inclination angle of 90 degrees for droplets with a volume of 5 μL, in agreement with work reported in [142 and 27]). This figure also compares the simulation results with our experimental data. Good general agreement can be seen between the measured and simulated sliding angles for different volumes. Figure 4.10b shows effects of wire spacing and YLCA on sliding angle for droplets with different volumes on a screen with

$d_w = 166$ µm. It is interesting to note that increasing the YLCA from 120 to 140 degrees, decreases the sliding angle by a factor greater than 2. Also consistent with the trend discuss previously, increasing the wire spacing increases the sliding angle. Comparing the data in Fig. 4.10a with those in Fig. 4.10b, it can be observed that for the same droplet volume and wire spacing, sliding angle increases with increasing the wire diameter for the same reason as was given in discussing Figs. 4.7b and 4.7c.

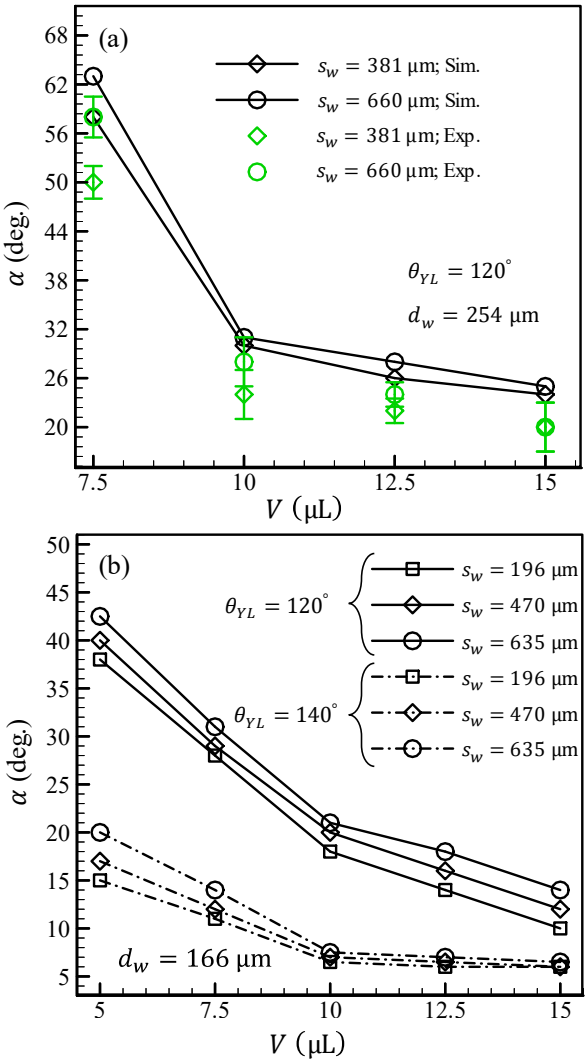

Fig 4.10: Effects of droplet volume on the sliding angle for screens with different diameters, different wire spacing, and different YLCAs are given in (a) and (b). Experimental and computational data are shown with green and black symbols, respectively.

4.6 Conclusions

In this work, we studied the role of geometrical properties of a hydrophobic wire screen on its interactions with water droplets both computationally and experimentally. Such information is valuable in many applications such as droplet–gas filtration (e.g., oil droplets removal from engine exhaust, mist filtration, fog harvesting) and droplet–liquid filtration (e.g., water droplet removal from fuels), as well as many other applications requiring self-cleaning or anti-icing surfaces. Our results indicate that apparent CA of a droplet on a wire screen decreases with increasing the spacing between the wires or with increasing the wire diameter. The predictions of our numerical simulations and experiments were compared with one another and the Cassie–Baxter equation (Eq. 4.2) and discussed in detail. It was emphasized that the Cassie–Baxter equation does not apply to surfaces with large roughness (relative to the droplet size) such as those considered in this study. We also studied the interplay between wire diameter, wire spacing, droplet volume, and YLCA on tilted hydrophobic screens. It was shown that droplet sliding angle increases with decreasing the YLCA or increasing the wire diameter (all other parameters being constant). The droplet sliding angle was also observed to increase with decreasing the droplet volume. Most interesting, our numerical simulations revealed that droplet sliding angle increases with increasing the wire spacing for screens with a fixed wire diameter in contrast to many previous studies reported in the literature. We attribute this behavior to the increase of the droplet's contact line on the receding side when the wire spacing is increased.

Chapter 5. Modeling Droplet Equilibrium Shape on Trilobal Fibers

5.1 Introduction

Understanding and controlling droplet movement inside fibrous media is important in predicting the performance of various engineering mechanisms such as liquid–liquid separation, liquid–gas filtration, textiles fabrication, water transport in fuel cells, and water harvesting [25]. Early studies on droplet-fiber interactions were focused on obtaining droplet profile and finding a relationship between Young-Laplace contact angle (YLCA) and apparent contact angle (ACA) for barrel shape droplets (axi-symmetric droplet) [133-134]. Droplet conformations also attracted a lot of investigation; barrel shape droplet usually form at smaller YLCA and higher droplet volume while clamshell droplet (droplet sits only on one side of the fiber) forms at larger YLCA and smaller volume [135]. However, both barrel shape and clamshell droplets may coexist depending on YLCA, surface tension, fiber diameter and droplet volumes [136]. More recent studies are focused on finding the force required to move a droplet along a smooth fiber, detach it from smooth or rough fibers and detach it from two intersecting smooth fibers [137-141].

Although circular fiber is the most common shape manufactured by synthetic fiber producers, other shapes such as elliptical, lobed, and wedge-shaped cross-sections, are beginning to emerge for a variety of reasons—performance, bulkiness, tactility, processing, etc. [142-143]. Filters made from these various fibers may be configured as pads, pleated papers, bonded webs, nettings, or composites [144-147,67]. The only research on droplet-fiber interaction on non-circular fibers considers wedge-shaped cross-sections [148] but does not explain the effect of the shape of the fiber –e.g., number and size of the wedges- or volume of the droplets on fibers' wettability explicitly. Our objective in this work is to highlight the importance of a fiber's cross-sectional

shape on ACA and droplet detachment force from the fibers. We predicted the 3D shape of the droplet and ACA of a droplet on a trilobal fiber. We also calculated the force required to detach the droplet from a trilobal fiber for different lobe height and azimuthal orientation.

The remainder of this paper is structured as follows. First, we introduce the numerical modeling approach conducted to simulate the 3D shape of the droplet on trilobal fiber in Sec. 5.2. Our investigations of the effects of lobe height and droplet volume on the shape and ACA(s) of droplet deposited on a trilobal fiber are reported Sec. 5.3. In this section, we also study the force required to detach a droplet from a trilobal fiber for different droplet sizes. Finally, the conclusions drawn from the work are given in Sec. 5.4.

5.2 Numerical Simulation

The numerical simulations presented in this paper are conducted via Surface Evolver (SE) code. SE is a finite element code which minimizes the energy of surfaces formed by surface tension and other energies subjected to various constraints [149]. SE is used in this study to obtain the equilibrium 3-D shape of a droplet deposited on a trilobal fiber. Consider a fiber with its centerline placed on the *y*-axis having a radius that is described by a sinusoidal wave, as shown in Fig. 5.1,

$$R(\alpha) = r[1 + a\ \sin(\omega\alpha + \varphi)] \tag{5.1}$$

where R is the circular radius of the fiber, $R(\alpha) = \sqrt{x^2 + z^2}$ is the local radius of the trilobal fiber at any point, $\alpha = Arctan\frac{x}{z}$ is angular position, and φ is azimuthal orientation with respect to x-axis -perpendicular to gravity direction**.** The number of lobes is given with ω, which in the case of a trilobal fiber is set equal to 3. The parameter a in Equation 5.1 controls the lobes' height as

can be seen with an example in Fig. 5.1b for a trilobal geometry with $r = 15$ µm and $\varphi = 90^{\circ}$, but a varying from 0 to 0.4.

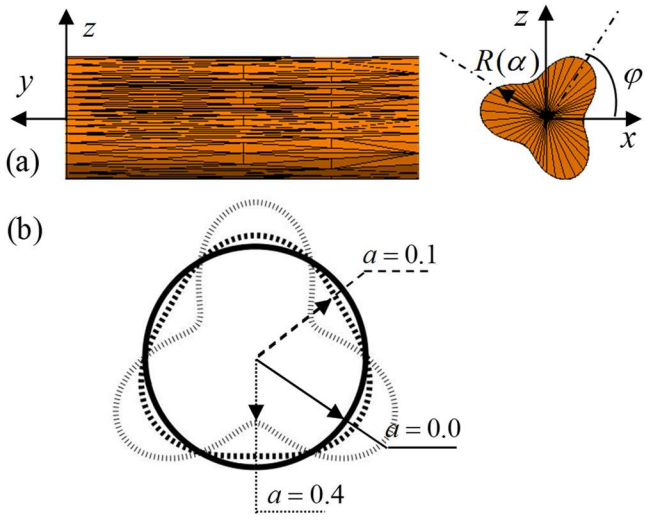

Fig. 5.1 (a): Side-view and cross-sectional view of a trilobal fiber. (b): Overlap of cross-sectional view of the fibers with different lobe height.

For a single-droplet–single-fiber system, the total free energy can be written as

$$E = \sigma A_{LG} - \sigma \int_{A_{SL}} cos\theta_{YL} dA + \int \rho h g \tag{5.2}$$

where σ is the surface tension and the subscripts LG and SL stand for liquid–gas and solid–liquid interfaces respectively. In this equation, h represents the vectorial change in the droplet's centroid position in response to a body force (zero in the absence of external forces). A, g, ρ, and V stand for area, body force per unit mass, liquid density, and the volume of the droplet, respectively. To find the equilibrium shape of a droplet on a fiber, an arbitrary initial shape with constant volume V is considered for the droplet, and its shape is allowed to evolve as the systems' free energy is being minimized iteratively. The input to the simulations is YLCA at the three-phase contact line as well as the surface tension and density of the liquid (in addition to droplet volume).

To ensure the that the curvature of the lobes (i.e., $\frac{r}{2\omega}$) is accurately captured in the simulations, the mesh density was increased by a power of 2 near the tip of the lobes. We also calculated the mean curvature of the droplet at each point H on the droplet surface to make sure that the simulation results satisfy the Laplace equation $P = \sigma H$ (i.e., the pressure P obtained from the Laplace equation matching that obtained from SE simulations).

5.3 Results and Discussion

In this section, we first discuss the effect of droplet volume and lobe height on the apparent contact angle. We then discuss the maximum detachment force of the droplet on the trilobal fiber followed by effect of cross-section. In all our simulations, we used water with a surface tension of 72 $\mathrm{nN/m}$ and a density of 1000 $\mathrm{g/L}$. We consider a fiber with a YLCA of $\theta_{YL} = 60^{\circ}$

5.3.1 Droplet Equilibrium Shape on a Rough Fiber

It is very important to notice that the droplet will have different local CA's when observed from different views. Fig. 5.2a shows the measurement of the local contact angle θ_l which is mentioned as the angle between the xy plane and the tangent to the droplet facet along the three phase contact line. Fig. 5.2a also shows possible planes that can go through the different views of the fiber to define local CA. The apparent contact angle is defined as the average of local contact angle along the three phase contact line which can be written as

$$\theta_A = \frac{\oint_c \theta_l dl}{\oint_c dl} \tag{5.3}$$

Fig. 5.2b shows the local contact angle on fiber with radius $r_f = 200\ \mu m$ along the perimeter (L_l/L_t is the ration of length of any point on the contact line to total length of the contact line) of trilobal fibers for different lobe heights. As expected, local CA varies around the three phase contact line (see Fig. 5.2b). It can be seen as the lobe height increases the local CA at any point on the three phase contact line decreases.

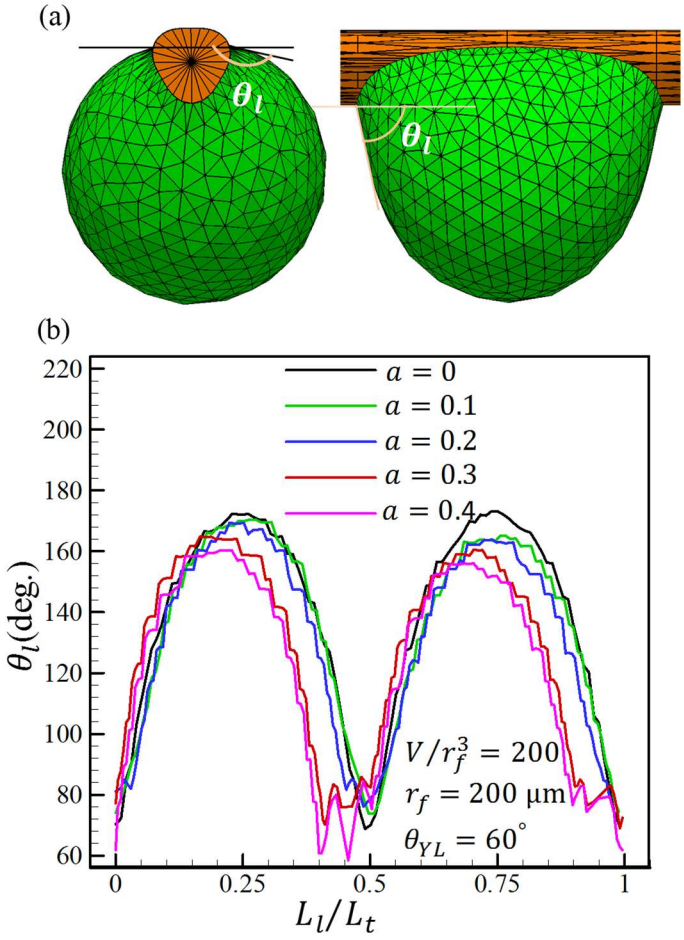

Fig. 5.2: (a) Local contact angle θ_l is shown using the tangent drawn to the droplet at the three phase contact line and xy plane for both lateral view(left) and longitudinal view(right) of the droplet. (b) Local contact angle is shown along the length of the contact line for different lobe heights for fiber radius $r_f = 200\ \mu m$ and droplet volume $V/{r_f}^3 = 200$ with $\theta_{YL} = 60°$.

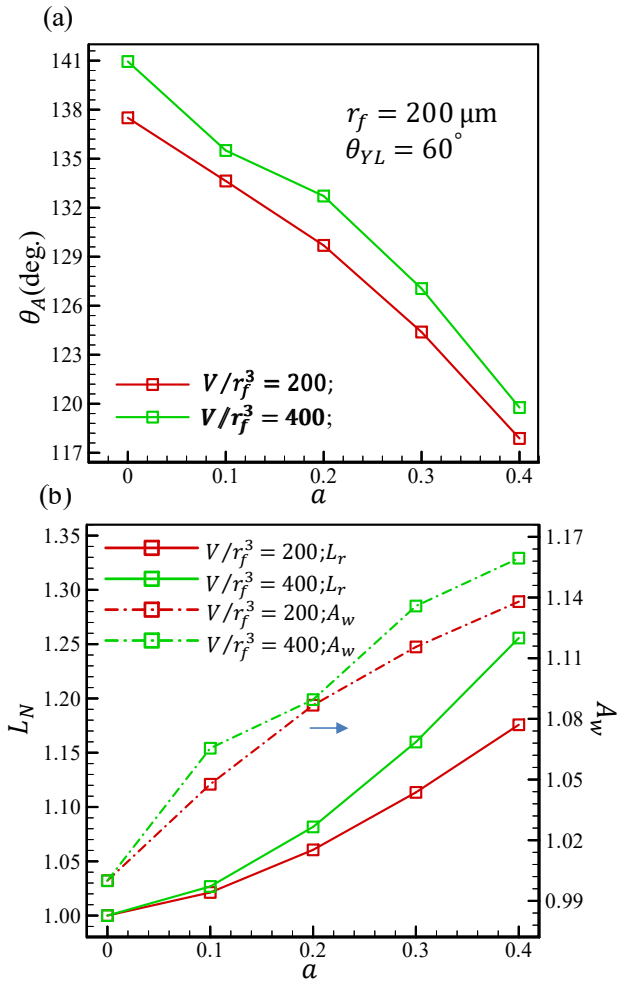

Fig. 5.3: (a) The apparent contact angle θ_A measured using Eq.5.3 is shown for fibers with different lobe heights ranging from $a = 0$ to $a = 0.4$ and radius $r_f = 200$ µm having YLCA $\theta_{YL} = 60°$ for two different volume ratio $V/{r_f}^3 = 200$ and $V/{r_f}^3 = 400$. (b) The total length of three phase contact line and wetted area were shown for the same parameters as in (a).

Fig. 5.3a shows the apparent contact angle measured using Eq. 5.3 for droplets of two different volumes $V/{r_f}^3 = 200$ and $V/{r_f}^3 = 400$ on fibers having radius $r_f = 200$ µm. It can be seen that as lobe height increases ACA decreases. This finding is in consistent with Wenzel's finding: roughness makes a philic surface more philic. This figure also shows effect of droplet volume on ACA. For the fibers having same lobe height (say $a = 0.4$), as the droplet volume increases, ACA

also increases. It is because as volume of the droplet increases the effect of a becomes less significant.

To explain the why ACA increases with increase in lobe height we report three-phase contact line and solid liquid area in Fig. 5.3b. For the sake of convenience we define non-dimensionalized contact length L_N and wetted area A_w are the ratio of the same parameter of a trilobal fiber to that of circular fiber. As the lobe height increases both L_N and A_w also increases. The increase in A_w can explain the increase in ACA in terms of Wenzel equation.

5.3.2 Droplet Detachment Force

In this section, we calculated the force required to detach the droplet. It is worthy to note that our numerical method is only able to simulate the equilibrium shape. Therefore we reported the maximum force at which the droplet can be found in equilibrium state as the force required to detach the droplet.

Fig. 5.4a shows three different azimuthal orientation φ we simulated to study the effect of lobe height on detachment force from trilobal fiber with radius $r_f = 200\ \mu m$ for droplet volume $V/{r_f}^3 = 200$ (see Fig. 5.4b). It can be seen as the lobe height increases the force per mass required to detach the droplet also increases. The main reason for this as explained in Fig. 5.3, that as lobe height increases apparent contact angle decreases making philic surface more philic. On the other hand for $\varphi = 90^{\circ}$(see Fig. 5.4b), the force required to detach the droplet is higher than the force required to detach from the fiber $\varphi = -90^{\circ}$ (see Fig. 5.4c). Moreover when the lobes were facing sides i.e., $\varphi = 45^{\circ}$, the detachment force is always lower compared to other orientations. Comparing the figures in fig. 5.4a, we can say that shows that the solid-liquid area of $\varphi = 90^{\circ}$is

higher so as the detachment force. However, this effect will gets smaller as volume increases because the relative size of the lobe height to the size of the droplet become insignificant at higher volume. Therefore, one can conclude that detachment force is a strong function of the φ at small volumes but as volume of the droplet increases the effect of φ becomes less significant.

Figure 5.5a shows the capillary forces and pressure forces acting on the droplet at equilibrium before detachment for a fiber with radius $r_f = 200$ µm and YLCA $\theta_{YL} = 60^{\circ}$. Furthermore balance of forces i.e., the pressure and the capillary forces on the equilibrium droplet (see Fig. 5.5a) existing on the fiber using analytical solution was presented. This is performed in order to verify the maximum detachment force obtained from the SE simulations with the analytical solution. The total force (F_t) acting along the z direction is the sum of the capillary force (F_c) and the pressure force (F_p) can be written as

$$F_t = F_c - F_p = \int_0^L \sigma cos\alpha \, dL - \int_L \; x\,(p - \rho g_z z)dy \qquad (5.4)$$

Where σ is the surface tension of the liquid, α is the angle of projection between the tangent to the facet of the droplet onto the z axis, L is the total length of the three phase contact line, p is the internal pressure of the droplet and $\rho g_z z$ is the change in pressure due to the force g_z at z coordinate.

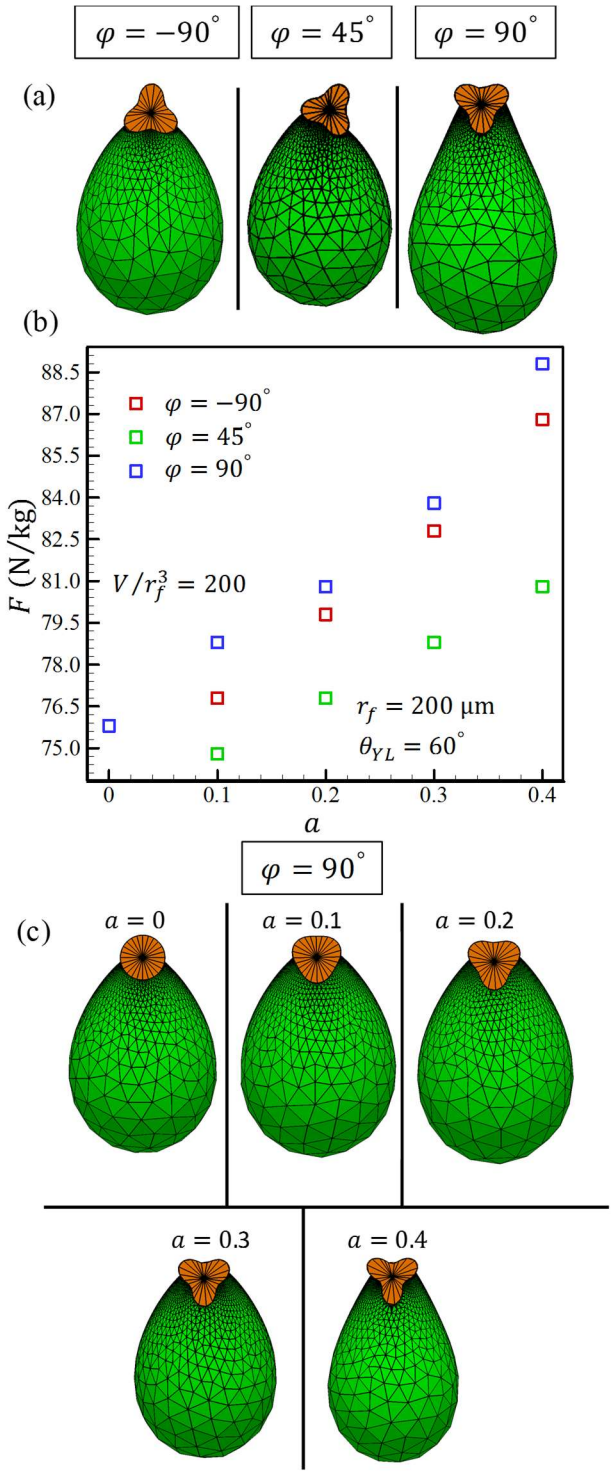

Fig. 5.4: The effects of the azimuthal orientation (a) on the maximum force per unit mass (b) required to detach droplets from a fiber with $r_f = 200$ μm but different lobe heights ranging from $a = 0$ to $a = 0.4$ and YLCA of $\theta_{YL} = 60°$. (c) The shape of a clamshell shape droplet with $V/{r_f}^3 = 200$ on a trilobal fiber for different lobe heights.

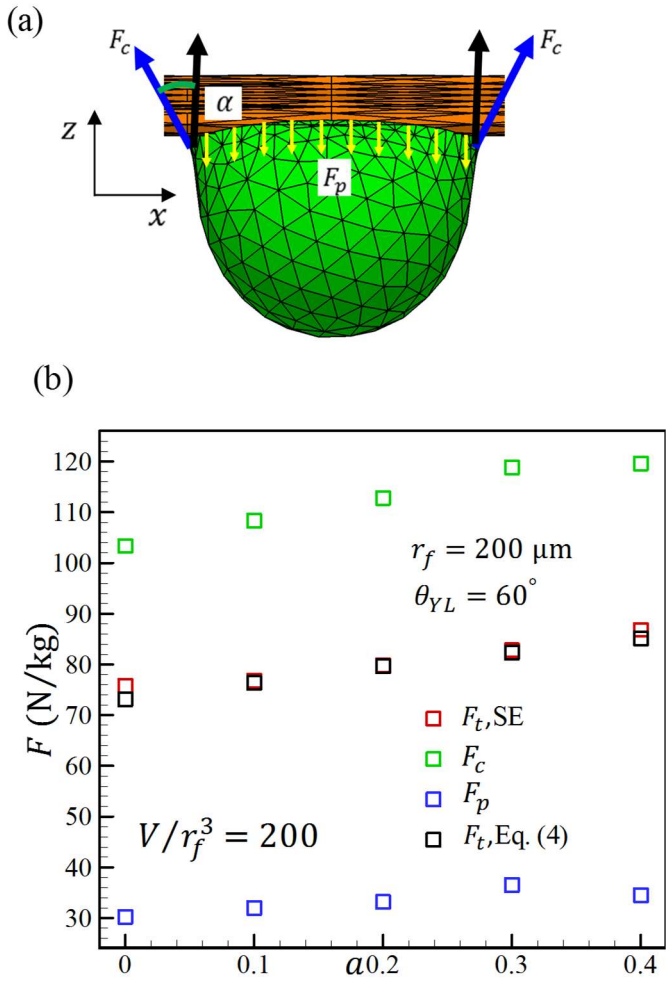

Fig. 5.5: (a) Free body diagram showing the forces acting on the droplet. (b) Effect of lobe height on the capillary force, pressure force and maximum detachment force on fiber radius $r_f = 200$ µm.

Figure 5.5b shows the individual force components normalized with mass of droplet acting on the trilobal fiber for different lobe height with droplet volume $V/{r_f}^3 = 200$. It can be seen that the capillary forces F_c (green) is much higher than the gravity force F_t (red). Moreover, the pressure force F_p (blue) acting along the direction of gravity counter acts the capillary force. On the other hand, when the

detachment force F_t (black) calculated using Eq. (5.4) shows a very good agreement with the detachment force from SE simulations.

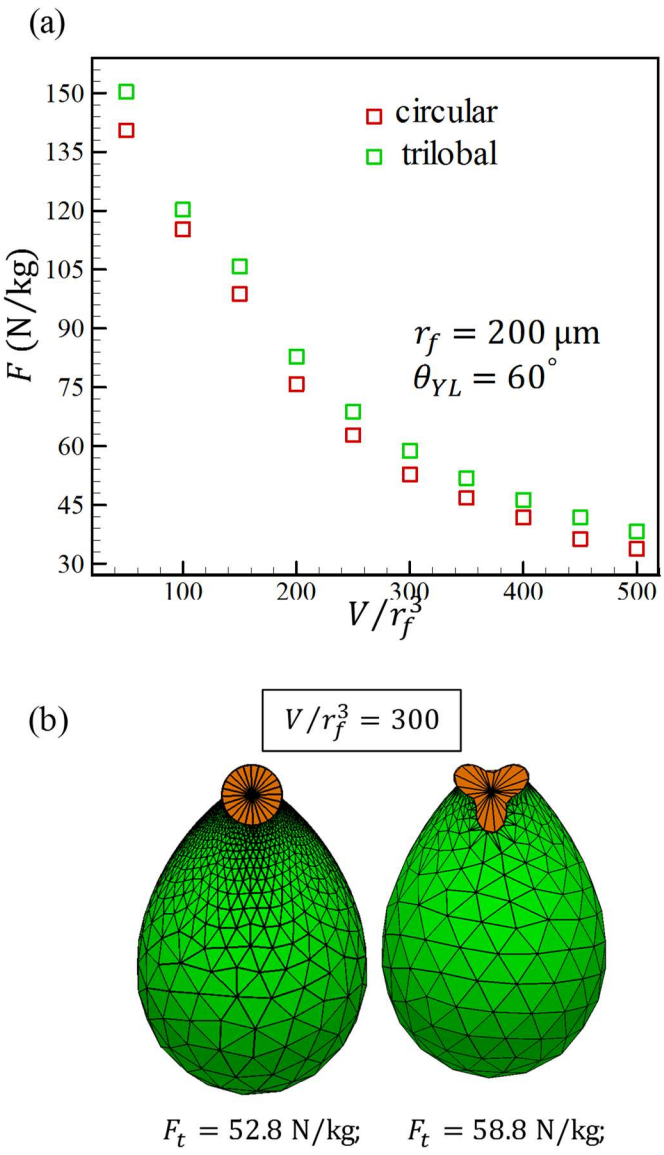

Fig. 5.6: The maximum force per unit mass required to detach droplets with different volumes for fiber with $r_f = 200$ µm for different cross-section of fibers (circularand trilobal) for an YLCA $\theta_{YL} = 60°$;(b) Droplet with $V/{r_f}^3 = 300$ for fibers with circular and trilobal cross section.

Fig. 5.6a shows the detachment force for droplet with different volumes on the fiber of radius $r_f =$ 200 µm for three different cross sections circular and trilobal (see Fig. 5.5b) with lobe height $a =$

0.4. It can be seen that the detachment force will be higher for the trilobal fibers when compared with circular fibers at smaller volume of droplets. However, this effect decreases with increase in droplets volume as the effect of cross section becomes insignificant at higher volumes.

5.5 Conclusions

Droplet apparent contact angle on a trilobal fiber was studied for the first time and found to be a function of lobe height and droplet volume. We showed that the ACA decreases as lobe height increases. The detachment force from a trilobal fiber is also calculated and it was shown that the lobe height and azimuthal orientation has significant role in detachment force. The detachment force increases with increase in lobe height and also it depends on the cross section of the fiber for smaller volume of droplets. As the droplet volume increases the fiber cross section doesn't affect the detachment force.

Chapter 6. Overall Conclusion

The main goal of this thesis is to simulate the liquid interactions over fibrous surfaces (nanofibrous mats, woven screens). We first presented a modeling approach for simulating the 3-D structure of nanofiber mats. In the proposed technique, fibers are treated as an array of beads with a diameter equal to the diameter of the fibers. This allowed us to observe an effect that has never been reported previously: for fibrous mats with identical weights, the thicker and more porous mat is not necessarily the one comprised of smaller fibers. Depending on how diameter of a fiber influences its tendency to bend at fiber-fiber crossovers, a fibrous mat made of fine fibers may or may not be more porous than its counterpart composed of coarser fibers.

We also presented analytical and numerical methods to estimate the air-water interface stability over superhydrophobic woven screen under elevated pressures. The failure pressure of SHP woven screens and how the interplay between the wire diameter and wire-to-wire spacing can affect the performance of a SHP screen was discussed. Then the efficiency of such surfaces in drag reduction for underwater applications were predicted by performing 3D simulations. Our simulations indicate that operating pressure in the Couette configuration does not significantly affect the drag reducing effects of the screens.

Droplet interactions with the hydrophobic woven screen were presented using computationally and experimentally. Our results indicate that apparent CA of a droplet on a wire screen decreases with increasing the spacing between the wires or with increasing the wire diameter. We also studied the interplay between wire diameter, wire spacing, droplet volume, and YLCA on tilted hydrophobic screens. It was shown that droplet sliding angle increases with decreasing the YLCA

or increasing the wire diameter. The droplet sliding angle was also observed to increase with decreasing the droplet volume. We attribute this behavior to the increase of the droplet's contact line on the receding side when the wire spacing is increased.

The wetting behavior of a droplet deposited on a nocircular fiber (trilobal) is also investigated numerically. Our simulations showed that the apparent contact angle decreases as lobe height increases. Therefore, upon increasing lobe amplitude, the wettability of the droplet also increases. The detachment force from a trilobal fiber is also calculated and it was shown that the lobe height and azimuthal orientation has significant role in detachment force. The detachment force increases with increase in lobe height and also it depends on the cross section of the fiber for smaller volume of droplets. We also found that the effect of lobe height becomes less significant on large droplet volume relative to roughness amplitude.

The main contribution of the work is to understand the dependency of wettability and hydrophobicity on the geometric parameters of the surface, physical properties of the fluid. The results of this work were, can be applied for design of SHP porous surface which has many applications including but not limited to fog-harvesting, oil–water separation, self-cleaning and anti-icing , and filtration.

Chapter 7. References

[1] D. Quere, Wetting and roughness, *Annu. Rev. Mater.* Res. 38 (**2008**) 71–99.

[2] J.P. Rothstein, Slip on superhydrophobic surfaces, *Annu. Rev. Fluid Mech.* 42 (**2010**) 89–109.

[3] A. M. J. Davis, E. Lauga, The friction of a mesh-like super-hydrophobic surface, *Phys. Fluids* 21 (**2009**) 113101.

[4] C. H. Lee, N. Johnson, J. Drelich, Y. K. Yap, The performance of superhydrophobic and superoleophilic carbon nanotube meshes in water–oil filtration, *Carbon* 49 (**2011**) 669-676.

[5] C.W. Extrand, Repellency of the lotus leaf: resistance to water intrusion under hydrostatic pressure, *Langmuir* 27 (**2011**) 6920–6925.

[6] A. Ganne, V.O. Lebed, A.I. Gavrilov, Combined wet chemical etching and anodic oxidation for obtaining the superhydrophobic meshes with anti-icing performance, *Colloids Surf. A* 499 (**2016**) 150-155.

[7] K.-C Park, S.S. Chhatre, S. Srinivasan, R.E. Cohen, G.H. McKinley, Optimal Design of Permeable Fiber Network Structures for Fog Harvesting, *Langmuir* 29 (**2013**) 13269−13277.

[8] N.R. Geraldi, G. McHale, B.B. Xu, G.G. Wells, L.E. Dodd, D. Wood, M.I. Newton, Leidenfrost transition temperature for stainless steel meshes, *Mater. Lett.* 176 (**2016**) 205-208.

[9] P.G. de Gennes, F. Brochard-Wyart, D. Quéré, Capillarity and Wetting Phenomena: Drops, Bubbles, Pearls, Waves, Springer-Verlag, New York, **(2004)**.

[10] T. Young, An Essay on the Cohesion of Fluids, *Philos Trans R Soc Lond.* **1805**;95:65–87.

[11] J. Ou, J.P. Rothstein Direct velocity measurements of the flow past drag-reducing ultrahydrophobic surfaces, *Phys Fluids.* (**2005)**;17(10).

[12] A. Tuteja, W. Choi, JM. Mabry, GH. McKinley, RE. Cohen. Robust omniphobic surfaces, *Proc Natl Acad* Sci. (**2008**), 105(47):18200–5.

[13] G. McHale, N.J. Shirtcliffe, C.R. Evans, M.I. Newton. Terminal velocity and drag reduction measurements on superhydrophobic spheres, *Appl Phys Lett.* (**2009**) 94(6).

[14] M.A. Samaha, H.V. Tafreshi, M. Gad-el-Hak. Modeling drag reduction and meniscus stability of superhydrophobic surfaces comprised of random roughness, *Phys Fluids.* (**2011**) 23(1).

[15] H. Dong, M. Cheng, Y. Zhang, H. Wei, F. Shi, Extraordinary drag-reducing effect of a superhydrophobic coating on a macroscopic model ship at high speed, *J Mater Chem A.* (**2013**) 1(19):5886–91.

[16] D.G. Venkateshan, M.A. Tahir, H.V. Tafreshi, and B. Pourdeyhimi, Modeling Effects of Fiber Rigidity on Thickness and Porosity of Virtual Electrospun Mats, *Materials and Design*, 96 (**2016**), 27.

[17] C.W. Extrand, Criteria for Ultralyophobic Surfaces. *Langmuir*, **(2004)** 20(12), 5013–8.

[18] M.A. Samaha, H.V. Tafreshi, M. Gad-el-Hak, Influence of Flow on Longevity of Superhydrophobic Coatings. *Langmuir*. (2012) 28(25) 9759–66.

[19] A.A. Hemeda, M. Gad-el-Hak, H.V. Tafreshi. Effects of hierarchical features on longevity of submerged superhydrophobic surfaces with parallel grooves. *Phys Fluids* **(2014)** 26(8).

[20] N.J. Shirtcliffe,G. McHale, M.I. Newton,G. Chabrol,C.C. Perry, Dual-Scale Roughness Produces Unusually Water-Repellent Surfaces. *Adv Mater*. **(2004)** 16(21).

[21] C. Lee, C-H. Choi, C-J. Kim, Structured Surfaces for a Giant Liquid Slip. *Phys Rev Lett.* **(2008)** 101(6).

[22] R.N. Wenzel, Resistance of Solid Surfaces To Wetting By Water. *Ind Eng Chem.* **(1936)** 28(8).

[23] A.B.D. Cassie, S.Baxter, Wettability of porous surfaces. *Trans Faraday Soc.* **(1944)** 40(0).

[24] B. Emami, T.M. Bucher, H.V. Tafreshi, D. Pestov, M. Gad-el-Hak, G.C. Tepper, Simulation of meniscus stability in superhydrophobic granular surfaces under hydrostatic pressure, *Colloids Surf., A* 385 (**2011**) 95–103.

[25] A. Tuteja, W. Choi, J.M. Mabry, G.H. McKinley, and R.E. Cohen, "Robust omniphobic surfaces," P Natl Acad Sci USA 105 **(2008)** 18200.

[26] S. Srinivasan, W. Choi, K.C. Park, S.S. Chhatre, R.E. Cohen, G.H. McKinley, Drag reduction for viscous laminar flow on spray-coated non-wetting surfaces, *Soft Matter* 9 (**2013**) 5691-5702.

[27] P. Contal, J. Simao, D. Thomas, T. Frising, S. Calle, J. C. Appert-Collin, D. Bemer, Clogging of fibre filters by submicron droplets. Phenomena and influence of operating conditions. *J. Aerosol Sci.* 35 (**2004**) 263–278.

[28] S. U. Patel, G. G. Chase, Separation of water droplets from water-in-diesel dispersion using superhydrophobic polypropylene fibrous membranes, Sep. Purif. Technol. 126 (**2014**) 62-68.

[29] S. Michielsen, H. J. Lee, Design of a superhydrophobic surface using woven structures, *Langmuir* 23 (**2007**) 6004-6010.

[30] S. Wurster, J. Meyer, Meyer, H. E. Kolb, G. Kasper, Bubbling vs. blow-off – On the relevant mechanism(s) of drop entrainment from oil mist filter media, *Sep. Purif. Technol.* 152 (**2015**) 70–79.

[31] E. Gauthier, T. Hellstern, I. G. Kevrekidis, J. Benziger, Drop detachment and motion on fuel cell electrode materials, *ACS Appl. Mater. Interfaces* 4 (**2012**) 761−771.

[32] T. Gilet, D. Terwagne, N. Vandewalle, Digital microfluidics on a wire, *Appl. Phys. Lett.* 95 (**2009**) 014106.

[33] J. Ju, H. Bai, Y. Zheng, T. Zhao, R. Fang, L. Jianga, A multi-structural and multi-functional integrated fog collection system in cactus, *Nat Commun.* 3 (**2012**) 1247.

[34] B.J. Carroll, Equilibrium conformations of liquid drops on thin cylinders under forces of capillarity. A theory for the roll-up process. *Langmuir.* **(1986)** 2(2).

[35] G. McHale, M. Newton. Global geometry and the equilibrium shapes of liquid drops on fibers. *Colloids Surf Physicochem Eng Asp.* **(2002)** 206(1–3).

[36] S. Rebouillat, B. Letellier, B. Steffenino, Wettability of single fibres – beyond the contact angle approach. Int J Adhes Adhes. **(1999)** 19(4).

[37] D. Quere, Drops at Rest on a Tilted Plane, *Langmuir,* (**1998)**, 14, 2213-2216.

[38] Z. Yoshimitsu, A. Nakajima, T. Watanabe, K. Hashimoto, Effects of Surface Structure on the Hydrophobicity and Sliding Behavior of Water Droplets, *Langmuir,* (**2002)**, 18, 5818-5822.

[39] M. Mei, J. Fan, D. Shou, The gravitational effect on the geometric profiles of droplets on horizontal fibers, *Soft Matter* 9 (**2013**) 10324-10334.

[40] S. Dawar, H. Li, J. Dobson, G. G. Chase, Drag correlation of drop motion on fibers, *Dry. Technol.* 24 (**2006**) 1283-1288.

[41] S. Haefner, O. Baumchen, K. Jacobs, Capillary droplet propulsion on a fibre, *Soft Matter* 11 (**2015**) 6921-6926.

[42] M. Davoudi, J. Fang, G. G. Chase, Barrel shaped droplet movement at junctions of perpendicular fibers with different orientations to the air flow direction, *Sep. Purif. Technol.* 162 (**2016**) 1–5.

[43] D. H. Reneker, A.L. Yarin, H. Fong, S. Koombhongse, Bending instability of electrically charged liquid jets of polymer solutions in electrospinning, *J. Appl. Phys.* 87 (**2000**) 4531–4547.

[44] J.M. Deitzel, J.D. Kleinmeyer, J.K. Hirvonen, N.C.B. Tan, Controlled deposition of electrospun poly(ethylene oxide) fibers, *Polymer* 42 (**2001**) 8163–8170.

[45] A.L. Yarin, E. Zussman, Upward needleless electrospinning of multiple nanofibers, *Polymer* 45 (**2004**) 2977–2980.

[46] D.H. Reneker, A.L. Yarin, Electrospinning jets and polymer nanofibers, *Polymer* 49 (**2008**) 2387–2425.

[47] W.E. Teo, S. Ramakrishna, A review on electrospinning design and nanofibre assemblies, *Nanotechnology* 17 (**2006**) R89–R106.

[48] G. Collins, J. Federici, Y. Imura, L.H. Catalani, Charge generation, charge transport, and residual charge in the electrospinning of polymers: A review of issues and complications, *J. Appl. Phys.* 111 (**2012**) 4.

[49] J. Stanger, N. Tucker, A. Wallace, N. Larsen, M. Staiger, R. Reeves, The effect of electrode configuration and substrate material on the mass deposition rate of electrospinning, *J. Appl. Polym. Sci.* 112 (**2009**) 1729–1737.

[50] B. Maze, H.V. Tafreshi, B. Pourdeyhimi, Geometrical modeling of fibrous materials under compression, *J. Appl. Phys.* (**2007**) 073533.

[51] B. Maze, H.V. Tafreshi, Q. Wang, B. Pourdeyhimi, A simulation of un-steady-state filtration via nanofiber media at reduced operating pressures, *J. Aerosol Sci.* 38 (**2007**) 550–571.

[52] Q. Wang, B. Maze, H.V. Tafreshi, B. Pourdeyhimi, Simulating through-plane permeability of fibrous materials with different fiber lengths, *Modell. Simul. Mater. Sci. Eng.* 15 (**2007**) 855–868.

[53] H.V. Tafreshi, M.S.A. Rahman, S. Jaganathan, Q. Wang, B. Pourdeyhimi, Analytical expressions for predicting permeability of bimodal fibrous porous media, *Chem. Eng. Sci.* 64 (**2009**) 1154–1159.

[54] S. Fotovati, H.V. Tafreshi, B. Pourdeyhimi, Influence of fiber orientation distribution on performance of aerosol filtration media, *Chem. Eng. Sci.* 65 (**2010**) 5285–5293.

[55] S.A. Hosseini, H.V. Tafreshi, Modeling permeability of 3-D nanofiber media in slip flow regime, *Chem. Eng. Sci.* 65 (**2010**) 2249–2254.

[56] R. Arambakam, H.V. Tafreshi, B. Pourdeyhimi, A simple simulation method for designing fibrous insulation materials, *Materials & Design* (**2013**) 44, 99.

[57] A.M. Saleh, S.A. Hosseini, H.V. Tafreshi, and B. Pourdeyhimi, 3-D Microscale simulation of dust-loading in thin flat-sheet filters: a comparison with 1-d macroscale simulations, *Chem. Eng. Sci.* (**2013**) 99, 284.

[58] R.M. Christensen, Theory of viscoelasticity, *2nd ed. Academic Press*, New York, **1982**.

[59] B. Pourdeyhimi, R. Ramanathan, R. Dent, Measuring fiber orientation in nonwovens Part 1: Simulation*, Text. Res. J.* 66 (**1996**) 713–722.

[60] E. Kreyszig, Advanced engineering mathematics, 10th ed. John Wiley & Sons, Inc, **2000**.

[61] J.J.L. Higdon, G.D. Ford, Permeability of three-dimensional models of fibrous porous media, *J. Fluid Mech.* 308 (**1996**) 341–361.

[62] D.S. Clague, R.J. Phillips, A numerical calculation of the hydraulic permeability of three-dimensional disordered fibrous media, *Phys. Fluids* 9 (**1997**) 1562–1572.

[63] S. Dhaniyala, B.Y.H. Liu, An asymmetrical, three-dimensional model for fibrous filters, *Aerosol Sci. Technol*. 30 (**1999**) 333–348.

[64] Z. Idris, L. Org'eas, C. Geindream, F.J. Bloach, L.J. Auriault, Microstructural effects on the flow law of power-law fluids through fibrous media, *Modell. Simul. Mater. Sci. Eng.* 12 (**2004**) 995–101.

[65] M. Faessel, C. Delisee, F. Bos, P. Castera, 3D Modelling of random cellulosic fibrous networks based on X-ray tomography and image analysis, *Compos. Sci. Technol.* 65 (**2005**) 1931–1940.

[66] M.M. Tomadakis, T.J. Robertson, Viscous permeability of random fiber structures: comparison of electrical and diffusional estimates with experimental and analytical results, *J. Compos. Mater.* 39 (**2005**) 163–188.

[67] J.P. Vassal, L. Orgeas, D. Favier, Modelling microstructure effects on the conduction in fibrous materials with fibre–fibre interface barriers, *Modell. Simul. Mater. Sci. Eng.* 16 (**2008**) 035007.

[68] T. Stylianopulos, Y. Andrew, J. Derby, X. Luo, M. Shepard, E. Sander, V. Barocas, Permeability calculations in three-dimensional isotropic and oriented fiber networks, *Phys. Fluids* 20 (**2008**) 123601.

[69] P. Katta, M. Alessandro, R.D. Ramsier, G.G. Chase, Continuous electrospinning of aligned polymer nanofibers onto a wire drum collector, *Nano Lett.* 4 (**2004**) 2215–2218

[70] S. Sarkar, S.C. Deevi, G.C. Tepper, Biased AC electrospinning of aligned polymer nanofibers, *Macromol. Rapid Commun.* 28 (**2007**) 1034–1039.

[71] F.O. Ochanda, M.A. Samaha, H.V. Tafreshi, G.C. Tepper, M. Gad-el-Hak, Effects of salinity on drag reduction and longevity of superhydrophobic fiber coatings, *J. Appl. Polym. Sci.* 123 (**2012**) 1112–1119.

[72] P.D. Dalton, C.V. Brooke, L. Farrugia, T.R. Dargaville, T.D. Brown, D.W. Hutmacher, Electrospinning and additive manufacturing: converging technologies, *Biomater. Sci.* 1 (**2013**) 171–185.

[73] T.M. Bucher, M.M. Amrei, H.V. Tafreshi, Wetting resistance of heterogeneous superhydrophobic coatings with orthogonally layered fibers, *Surf. Coat. Technol.* 277 (**2015**) 117–127.

[74] T.M. Bucher, H.V. Tafreshi, G.C. Tepper, Modeling filtration performance of nanofiber coatings with orthogonal fiber orientations, *Powder Technol.* 249 (**2013**) 43–53.

[75] N.J. Shirtcliffe, G. McHale, S. Atherton, M.I. Newton, An introduction to superhydrophobicity, *Adv. Colloid Interf. Sci.* 161 (**2010**) 124–138.

[76] C. Lee, C.-H. Choi, C.-J. Kim, Structured surfaces for giant liquid slip, *Phys. Rev. Lett.* 101 (**2008**) 064501.

[77] A. Samaha, H.V. Tafreshi, M. Gad-el-Hak, Effects of hydrostatic pressures on drag-reduction performance of submerged aerogel particle coatings, *Colloids Surf. A* 399 (**2012**) 62–70.

[78] A. Hemeda, H.V. Tafreshi, Instantaneous Slip-Length in Superhydrophobic Microchannels: Grooves with Dissimilar Walls or Arbitrary Wall Curvatures, *Phys. Fluids* 27 (**2015**) 102101.

[79] J.C. Brennan, N.R. Geraldi, R.H. Morris, D.J. Fairhurst, G. McHale, M.I. Newton, Flexible conformable hydrophobized surfaces for turbulent flow drag reduction, *Sci. Rep.* 5 (**2015**) 10267 .

[80] S. Srinivasan, J.A. Kleingartner, J.B. Gilbert, R.E. Cohen, A.J.B. Milne, G.H. McKinley, Sustainable Drag Reduction in Turbulent Taylor-Couette Flows by Depositing Sprayable Superhydrophobic Surfaces, *Phys. Rev. Lett.* 114 (**2015**) 014501.

[81] J. Song, S. Huang, Y. Lu, X. Bu, J.E. Mates, A. Ghosh, R. Ganguly, C.J. Carmalt, I.P. Parkin, W. Xu, C.M. Megaridis, Self-driven one-step oil removal from oil spill on water via selective-wettability steel mesh, *ACS Appl. Mater. Interfaces* 6 (**2014**) 19858–19865.

[82] J. Li, L. Yan, H. Li, J. Li, F. Zha, Z. Lei, A facile one-step spray-coating process for the fabrication of a superhydrophobic attapulgite coated mesh for use in oil/water separation, *RSC Adv.* 5 (**2015**) 53802.

[83] S.U. Patel, S.U. Patel, G.G. Chase, Electrospun superhydrophobic poly(vinylidene fluoride-co-hexafluoropropylene) fibrous membranes for the separation of dispersed water from ultralow sulfur diesel, *Energy Fuels* 27 (**2013**) 2458–2464.

[84] E.J.Y Ling, V Uong, J-S. Renault-Crispo, A-M. Kietzig, P Servio, Reducing Ice Adhesion on Nonsmooth Metallic Surfaces: Wettability and Topography Effects, *ACS Appl. Mater. Interfaces,* 8 (**2016**) 8789−8800.

[85] S.M. Lee, D.J. Oh, I. D. Jung, P. G. Jung, K. H. Chung, W. I. Jang, J. S. Ko, Evaluation of the waterproof ability of a hydrophobic nickel micromesh with array-type microholes, *J. Micromech. Microeng.* 19 (**2009**) 125024.

[86] Y.M. Shin, S.K. Lee, J.Y. Lee, J.H. Kim, J.H. Park, C.H. Ji, Microfabricated environmental barrier using ZnO nanowire on metal mesh, *J. Micromech. Microeng*. 23 (**2013**) 127001.

[87] Z.X. Jiang, L. Geng, Y.D. Huang, Design and fabrication of hydrophobic copper mesh with striking loading capacity and pressure resistance, *J. Phys. Chem. C* 114 (**2010**) 9370–9378.

[88] Z.X. Jiang, L. Geng, Y.D. Huang, Fabrication of superhydrophobic 3-D braided carbon fiber fabric boat, *Mater. Lett.* 64 (**2010**) 2441–2443.

[89] Q. Pan, M. Wang, Miniature boats with striking loading capacity fabricated from superhydrophobic copper meshes. *ACS Appl. Mater. Interfaces* 1 (**2009**) 420–423.

[90] Z.X. Jiang, L. Geng, Y.D. Huang, S.A. Guan, W. Dong, Z.Y. Ma, The model of rough wetting for hydrophobic steel meshes that mimic Asparagus setaceus leaf, *J. Colloid Interface Sci.* 354 (**2011**) 866-872.

[91] S.S. Chhatre, W. Choi, A. Tuteja, K-C Park, J.M. Mabry, G.H. McKinley, R.E. Cohen, Scale Dependence of Omniphobic Mesh Surfaces, *Langmuir*, 26 (**2010**) 4027–4035.

[92] A. Hemeda and H.V. Tafreshi, General Formulations for Predicting Longevity of Submerged Superhydrophobic Surfaces Comprised of Pores or Posts, *Langmuir,* 30 (**2014**) 10317.

[93] K.A. Brakke, The surface evolver and the stability of liquid surfaces, *Philos. Trans. R.Soc. Lond. A* 354 (**1996**) 2143–2157.

[94] A. S. Haase, E. Karatay, P. A. Tsai, R.G.H. Lammertink, Momentum and mass transport over a bubble mattress: the influence of interface geometry, *Soft Matter* 9 (**2013**) 8949-8957.

[95] X. Yang, Z. C. Zheng, Effects of channel scale on slip length of flow in micro/nanochannels, *J. Fluids Eng.* 132 (**2010**) 061201-061206.

[96] D.G. Venkateshan, M.M Amrei, A.A. Hemeda, Z. Cullingsworth, J. Corbett, and H.V. Tafreshi, Failure Pressures and Drag Reduction Benefits of Superhydrophobic Wire Screens, *Colloids Surf. A*, 511 (**2016)**, 247.

[97] T. Darmanin, J. Tarrade, E. Celia, F. Guittard, Superoleophobic Meshes with High Adhesion by Electrodeposition of Conducting Polymer Containing Short Perfluorobutyl Chains, *J. Phys. Chem. C,* 118 (**2014**), 2052−2057.

[98] R. Grynyov, Edward Bormashenko, G. Whyman, Y. Bormashenko, A. Musin, R. Pogreb, A. Starostin, V. Valtsifer, V. Strelnikov, A. Schechter, S. Kolagatla, Superoleophobic Surfaces Obtained via Hierarchical Metallic Meshes, *Langmuir,* 32(2016), 4134−4140.

[99] J. Fang, A. Aljuhani, G. G. Chase, Water drop movement on woven fiber mat surfaces due to flow of diesel Fuel, *Sep. Purif. Technol.,* 171(**2016**), 123–130.

[100] M. Rajaram, X. Heng, M. Oza, Enhancement of fog-collection efficiency of a Raschel mesh using surface coatings and local geometric changes, *Colloids Surf. A*, 508(**2016)**, 218-229.

[101] J. Wu, L. Zhang, Y. Wang, P. Wang, Efficient and Anisotropic Fog Harvesting on a Hybrid and Directional Surface, *Adv. Mater. Interfaces,* 4(**2017)**, 1600801.

[102] D. Quere, Drops at Rest on a Tilted Plane, *Langmuir,* 14(**1998)**, 2213-2216.

[103] Z. Yoshimitsu, A. Nakajima, T. Watanabe, K. Hashimoto, Effects of Surface Structure on the Hydrophobicity and Sliding Behavior of Water Droplets, *Langmuir,* 18(**2002)**, 5818-5822.

[104] C. W. Extrand, Designing for Optimum Liquid Repellency, *Langmuir,* 22(**2006)**, 1711.

[105] A.I. ElSherbini a, A.M. Jacobi, Retention forces and CAs for critical liquid drops on non-horizontal surfaces, *J. Colloid Interface Sci.*299(**2006)**, 841–849.

[106] P.S. Yadav, P. Bahadur, R. Tadmor, K. Chaurasia, A. Leh, Drop Retention Force as a Function of Drop Size, *Langmuir,* 24(**2008)**, 3181-3184.

[107] B. Balu, A. D. Berry, D. W. Hess,V. Breedveld, Patterning of superhydrophobic paper to control the mobility of micro-liter drops for two-dimensional lab-on-paper applications, *Lab Chip*, 9(**2009)**, 3066–3075.

[108] Cunjing Lv, Changwei Yang, Pengfei Hao, Feng He, and Quanshui Zheng, Sliding of Water Droplets on Microstructured Hydrophobic Surfaces, *Langmuir,* 26 (**2010**), 11 8704–8708.

[109] X.Yang, X. Liu, Y. Lu, S. Zhou, M. Gao, J. Song, W. Xu, Controlling the Adhesion of Superhydrophobic Surfaces Using Electrolyte Jet Machining Techniques, *Sci. Rep.* 6(**2016)**, 23985.

[110] H. Choi, H. Liang, Wettability and spontaneous penetration of a water drop into hydrophobic pores, *J. Colloid Interface Sci.*, 477(**2016)**, 176 -180.

[111] M.M. Amrei, D.G. Venkateshan, N. D'Souza, J. Atulasimha, H.V. Tafreshi, Novel Approach to Measuring the Droplet Detachment Force from Fibers, *Langmuir*, 32(**2016)**, 13333.

[112] M.M. Amrei, M. Davoudi, G.G. Chase, H.V. Tafreshi, Effects of Roughness on Droplet Apparent CAs on a Fiber, *Sep. Purif. Technol.,* 180(**2017)**, 107.

[113] A. Marmur, Wetting on Hydrophobic Rough Surfaces: To Be Heterogeneous or Not To Be?, *Langmuir*, 19(**2003)**, 8343.

[114] A. Marmur, The Lotus Effect: Superhydrophobicity and Metastability, *Langmuir,* 20(**2004)**, 3517-3519.

[115] C. W. Extrand, Model for Contact Angles and Hysteresis on Rough and Ultraphobic Surfaces, *Langmuir*, 18(**2002)**, 7991-7999.

[116] S. S. Chhatre, A. Tuteja, W. Choi, A. Revaux, D. Smith, J. M. Mabry, G. H. McKinley, R. E. Cohen, Thermal Annealing Treatment to Achieve Switchable and Reversible Oleophobicity on Fabrics, *Langmuir*, 25(**2009)**, 13625–13632.

[117] J. A. Kleingartner, S. Srinivasan, Q. T. Truong, M. Sieber, R. E. Cohen, G. H. McKinley, Designing Robust Hierarchically Textured Oleophobic Fabrics, *Langmuir*, 31(**2015)**, 13201−13213.

[118] L. Feng, Z. Zhang, Z. Mai, Y. Ma, B. Liu, L. Jiang, D. Zhu, A Super-Hydrophobic and Super-Oleophilic Coating Mesh Film for the Separation of Oil and Water, *Angew. Chem. Int. Ed*., 43(**2004)**, 2012 –2014.

[119] A.J.B. Milne, A. Amirfazli, The Cassie equation: How it is meant to be used, *Advances in Colloid and Interface Science*, 170(**2012)**, 48–55.

[120] K. Kawasaki, Study of Wettability of Polymers by Sliding of Water Drop*, J. Colloid Sci.*, 15 (**1960**), (5), 402-407.

[121] B. Krasovitski, A. Marmur, Drops Down the Hill: Theoretical Study of Limiting Contact Angles and the Hysteresis Range on a Tilted Plate, *Langmuir*, 21(**2005)**, 3881-3885.

[122] T.H. Chou, S.J. Hong, Y.J. Sheng, H.K. Tsao, Drops Sitting on a Tilted Plate: Receding and Advancing Pinning, *Langmuir*, 28(**2012)** 5158-5166.

[123] H. Aziz, M.M. Amrei, A. Dotivala, C. Tang, H.V. Tafreshi, Modeling Cassie Droplets on Superhydrophobic Coatings with Orthogonal Fibrous Structures, *Colloids Surf. A*, 512(**2017)**, 61.

[124] S. Brandon, N. Haimovich, E. Yeger, A. Marmur, Partial wetting of chemically patterned surfaces: The effect of drop size, *J. Colloid Interface Sci.*, 263(**2003)**, 237–243.

[125] A. Marmur, Soft contact: measurement and interpretation of contact angles, *Soft Matter*, 2(**2006)**, 12–17.

[126] A. Marmur, E. Bittoun, When Wenzel and Cassie Are Right: Reconciling Local and Global Considerations, *Langmuir*, 25(**2009)**, 3, 1279.

[127] A. Milionis, D. Fragouli, L. Martiradonna, G. C. Anyfantis, P. D. Cozzoli, I. S. Bayer, A. Athanassiou, Spatially Controlled Surface Energy Traps on Superhydrophobic Surfaces, *ACS Appl. Mater. Interfaces*, 6(**2014)**, 1036−1043.

[128] R. Zhang, P. Hao, F. He, Drop Impact on Oblique Superhydrophobic Surfaces with Two-Tier Roughness, *Langmuir*, 33(**2017)**, 3556−3567.

[129] B. Zhang, J. Wang, X. Zhang, Effects of the Hierarchical Structure of Rough Solid Surfaces on the Wetting of Microdroplets, *Langmuir*, 29(**2013)**, 6652−6658.

[130] T. P. Adam, K. K. Varanasi, Self-similarity of contact line depinning from textured surfaces, *Nature communications,* 4(**2013)**, 1492.

[131] E.B. Dussan V, R.T.-P. Chow, On the ability of drops or bubbles to stick to nonhorizontal surfaces of solids, *J. Fluid Mech.,* 137(**1983)**, 1–29.

[132] F. Schellenberger, N. Encinas, D. Vollmer, H. J. Butt, How Water Advances on Superhydrophobic Surfaces, *Phys. Rev. Lett.*, 116(**2016)**, 096101.

[133] B. J. J, Carroll,. The accurate measurement of contact angle, phase contact areas, drop volume, and Laplace excess pressure in drop-on-fiber systems. *J. Colloid Interf. Sci.,* 57 (**1976**) 488-495.

[134] S. Rebouillat, B. Letellier, B. Steffenino, Wettability of single fibers-beyond the contact angle approach. *Int. J. Adhes. Adhes.,* 19 (**1999**) 303-314.

[135] R.J. Roe, Wetting of fine wires and fibers by a liquid-film, *J. Colloid Interf. Sci.*. 50 (**1975**) 70–79.

[136] T.-H. Chou, S.-J. Hong, Y.-E. Liang, H.-K. Tsao, Y.-J. Sheng, Equilibrium phase diagram of drop-on-fiber: coexistent states and gravity effect, *Langmuir*, 27 (**2011**) 3685-3692.

[137] R. Mead-Hunter, B.J. Mullins, T. Becker, R.D. Braddock, Evaluation of the Force Required to Move a Coalesced Liquid Droplet along a Fiber. *Langmuir*, 27 (**2011**) 227-232.

[138] A.L. Yarin, W. Liu, D.H. Reneker, Motion of droplets along thin fibers with temperature gradient. *J. Applied. Phys*. 91(**2002**) 4751-4760.

[139] T. Gilet, D. Terwagne, N. Vandewalle, Droplets sliding on fibres. *Eur. Phys. J. E* 31 (**2010**) 253-262.

[140] D.G. Venkateshan and H.V. Tafreshi, Modelling droplet sliding angle on hydrophobic wire screens, Colloids and Surfaces A, 538 (**2018**), 310.

[141] M.M. Amrei, M. Davoudi, G.G. Chase and H.V. Tafreshi, Effects of Roughness on Droplet Apparent Contact Angles on a Fiber, Separation and Purification Technology, 180 (**2017**) 107.

[142] B. D. Regan, P.C. Raynor, Single-Fiber Diffusion Efficiency for Elliptical Fibers, *Aerosol Sci.and Tech*., 43 (**2009**) 533–543.

[143] M.A. Bueno, A.P. Aneja, M. Renner, Influence of the shape of fiber cross section on fabric surface characteristics*, J. Mater. Sci.,* 39 (**2004**) 557-564.

[144] I.M. Hutten, Handbook of Nonwoven Filter Media, *Elsevier,* (**2007**).103–194.

[145] S. Fotovatia, H. Vahedi Tafreshia, B. Pourdeyhimi, Analytical expressions for predicting performance of aerosol filtration media made up of trilobal fibers, *J. Hazard Matter,* 186 (**2011**) 1503–1512.

[146] G.E.R. Lamb, P.A. Costanza, Influences of Fiber Geometry on the Performance of Nonwoven Air Filters: Part III Cross-sectional shape, *Text. Res. J.,* 50 (**1980**) 362–370.

[147] S.A. Hosseini, H. Vahedi Tafreshi, On the importance of fibers' cross-sectional shape for air filters operating in the slip flow regime, *Powder Technol.,* 212 (**2011**) 425–431.

[148] B.J. Carroll, The equilibrium of liquid drops on smooth and rough circular cylinders, *J. Colloid Interf. Sci.,* 97 (**1984**) 195–200.

[149] K.A. Brakke, The Surface Evolver. Exp. *Math.,* 1 (**1992**) 141–165.

Appendix A: Vita

DELLI GANESH VENKATESHAN

Cell: 860-402-9386; Email: venkateshadgg@vcu.edu

SUMMARY

- Demonstrated problem-solving ability in fluid and solid mechanics.
- Experienced in multi-phase flow modeling with publications in peer-reviewed journals.
- Proficient in computer programming.

EDUCATION

- **PhD in Mechanical & Nuclear Engineering**
  Virginia Commonwealth University, (August 2014–Expected Graduation April 2018).
  Thesis: Modeling Fluid Motion over Fibrous Surfaces.
- **M. Tech in Chemical Engineering**
  Indian Institute of Technology, Guwahati, India (2012–2014).
  Thesis: Stokesian Dynamics Simulation of Suspension flow in Confined Geometries.
- **B. Tech in Chemical Engineering**
  Sri Venkateswara University College of Engineering, Tirupathi, India (2007–2011).

PROFESSIONAL EXPERIENCE

Graduate Research and Teaching Assistant, VCU August, 2014– Present

Assisted in several research projects by developing numerical or analytical models or designing experimental setups.

- Developed an in-house computer code to simulate deformation of nanofibers in a 3-D fibrous network (electrospun fiber mats).
- Developed numerical simulations for flow over superhydrophobic surfaces using ANSYS.
- Developed predictive models and experimental validations for numerous fluid–surface interactions, e.g., droplet motion over fibrous surfaces.
- Familiar with computational methods/tools used for modeling aerosol flows.
- Familiar with User-Defined Functions in ANSYS environment.
- Experienced with C++, MATLAB, and Python.
- Authored/co-authored 7 journal articles while doing a PhD at VCU
- Teaching Assistant for Numerical Methods and Dynamic Systems.

Teaching and Research Assistant, Indian Institute of Technology, India September, 2012–April, 2014

- Conducted research on Stokesian Dynamics Simulation of Suspension flow in confined geometries.
- Numerical simulations were carried out in MATLAB and FORTRAN.
- Assisted for the courses, Numerical Methods in Chemical Engineering, Computational Fluid Dynamics. Fluid dynamics laboratory.

- Presented lectures on programming the numerical methods in MATLAB for graduate students.

TECHNICAL AND EXPERIMENTAL SKILLS

- **Engineering Packages:** FLUENT, WORKBENCH ANSYS, COMSOL and Surface Evolver.
- **Mathematical Packages:** MATLAB, Simulink, MATHEMATICA and MAPLE.
- **Programming Languages:** FORTRAN, C++, C, Python, and Visual Basic.
- **Experimental:** Electrospinning, Particle Image Velocimetry (PIV), Imaging (optical and SEM), Rheometer.

RESEARCH INTERESTS AND ACTIVITIES

- Modeling and experiment with porous media and multiphase flows.
- Interfacial phenomena.
- Computer simulation and code development.

RELEVANT COURSEWORK

- Multiphase Flow, Computational Fluid Phenomena, Advanced Transport Phenomena, Convective Heat Transfer, Materials Science, Advanced Thermodynamics.

HONORS AND AWARDS

- School of Engineering *Dissertation Fellowship Award*, 2017–2018, VCU.
- 2nd place winner of *Outstanding Graduate Research Award*, 2016–2017, VCU.
- *Human Resource Development (HRD) scholarship* for Post-Graduation 2012–2014.
- Recipient of a *travel grant award* to attend a 3-day workshop on Rheology of Complex Fluids in 2014, India.
- Selected as *Project Assistant* at Wipro Technologies (an I.T. firm) during undergraduate campus hiring.

PEER-REVIEWED JOURNAL PUBLICATIONS

1. **D.G. Venkateshan,** M.A. Tahir, H.V. Tafreshi, and B. Pourdeyhimi, Modeling Effects of Fiber Rigidity on Thickness and Porosity of Virtual Electrospun Mats, *Materials and Design* 96, 27 (2016).
2. **D.G. Venkateshan,** M.M Amrei, A.A. Hemeda, Z. Cullingsworth, J. Corbett, and H.V. Tafreshi, Failure Pressures and Drag Reduction Benefits of Superhydrophobic Wire Screens, *Colloids and Surfaces A* 511, 247 (2016).
3. M. M. Amrei, **D. G. Venkateshan**, N. D'Souza, J. Atulasimha, and H. V. Tafreshi, Novel Approach to Measuring the Droplet Detachment Force from Fibers, *Langmuir,* 32, 50 (2016).
4. **D.G. Venkateshan** and H.V. Tafreshi, Modelling Droplet Sliding Angle on Hydrophobic Wire Screens, *Colloids and Surfaces A* 538, 310 (2017).

5. A. Moghadam, M.Jamali, **D.G. Venkateshan** and H.V. Tafreshi, Modeling Air–Water Interface in Disordered Orthogonally Layered Fibrous Media with Heterogeneous Wettabilities (in preparation)
6. **D.G. Venkateshan**, M.M. Amrei, N.Farhan, H.V. Tafreshi, Break-up Force of a Droplet Deposited on Non-circular Fibers (in preparation).
7. S.H. Yousefi, **D.G. Venkateshan**, C.Tang, H. V. Tafreshi, and B. Pourdeyhimi, Modeling of Thickness And Porosity of Polystyrene Electrospun Mats (in preparation).

CONFERENCE PRESENTATIONS

1. **D.G Venkateshan** and H.V. Tafreshi, Modelling Drag Reduction and Droplet Mobility over Superhydrophobic Wire Screens, *Virginia Soft Matter Workshop,* Sep. 2017.
2. **D.G Venkateshan**, M.Tahir, S.H. Yousefi, H.V. Tafreshi and B. Pourdeyhimi, Influence of Fiber Rigidity During Deposition on the Characteristics of Electrospun Mats, accepted for presentation at *Nanofibers, Applications & Related Technologies (NART) conference*, Sep. 13-15 2016, Raleigh, NC.
3. **D.G Venkateshan** and P. Madhala, Chemical Engineering in human body, *Fusion*, Aug. 2010, Ananthapur, India.
4. **D.G Venkateshan** and S. Kumar, Simulation studies on heat transfer, *I.I.ChE & J.C.C.E*, Sep. 2010, Guntur, India.
5. **D.G Venkateshan,** Bioreactor for the removal of SO2 from waste air, *Chemosphere*, Mar. 2009, Tirupathi, India.